


Jacob-induced transcriptional inactivation of CREB promotes A β -induced synapse loss in Alzheimer's disease

Katarzyna M Grochowska^{1,2,†} , Guilherme M Gomes^{1,3,†} , Rajeev Raman^{1,†}, Rahul Kaushik^{1,†}, Liudmila Sosulina^{4,5}, Hiroshi Kaneko^{4,5}, Anja M Oelschlegel¹, PingAn Yuanxiang¹ , Irene Reyes-Resina¹ , Gonca Bayraktar¹, Sebastian Samer¹, Christina Spilker¹ , Marcel S Woo⁶ , Markus Morawski⁷ , Jürgen Goldschmidt⁸ , Manuel A Friese⁶ , Steffen Rossner⁷, Gemma Navarro^{9,10}, Stefan Remy^{3,4,5}, Carsten Reissner¹¹ , Anna Karpova^{1,3,*} , & Michael R Kreutz^{1,2,3,5,**} 

Abstract

Synaptic dysfunction caused by soluble β -amyloid peptide (A β) is a hallmark of early-stage Alzheimer's disease (AD), and is tightly linked to cognitive decline. By yet unknown mechanisms, A β suppresses the transcriptional activity of cAMP-responsive element-binding protein (CREB), a master regulator of cell survival and plasticity-related gene expression. Here, we report that A β elicits nucleocytoplasmic trafficking of Jacob, a protein that connects a NMDA-receptor-derived signalosome to CREB, in AD patient brains and mouse hippocampal neurons. A β -regulated trafficking of Jacob induces transcriptional inactivation of CREB leading to impairment and loss of synapses in mouse models of AD. The small chemical compound Nitarson selectively hinders the assembly of a Jacob/LIM-only 4 (LMO4)/ Protein phosphatase 1 (PP1) signalosome and thereby restores CREB transcriptional activity. Nitarson prevents impairment of synaptic plasticity as well as cognitive decline in mouse models of AD. Collectively, the data suggest targeting Jacob protein-induced CREB shutoff as a therapeutic avenue against early synaptic dysfunction in AD.

Keywords Alzheimer's disease; Amyloid pathology; CREB; early synaptic dysfunction; Jacob

Subject Categories Molecular Biology of Disease; Neuroscience

DOI 10.15252/embj.2022112453 | Received 25 August 2022 | Revised 7

December 2022 | Accepted 9 December 2022 | Published online 3 January 2023

The EMBO Journal (2023) 42: e112453

Introduction

Soluble oligomeric β -Amyloid peptide (A β) induces deterioration of synaptic function in Alzheimer's disease (AD) even before overt signs of dementia and plaque formation (Selkoe, 2002; Selkoe & Hardy, 2016; Forner *et al*, 2017; Li & Selkoe, 2020; Peng *et al*, 2022). While a large number of synaptic proteins have been suggested as A β receptors (Jarosz-Griffiths *et al*, 2016), their pathophysiological relevance for synaptic dysfunction *in vivo* is still elusive given that the earliest hallmark of AD in humans and animal models is neuronal hyperexcitability caused by suppression of glutamate reuptake (Zott *et al*, 2019). In this scenario, glutamate spillover to perisynaptic sites might cause detrimental activation of extrasynaptic N-methyl-D-aspartate receptors (NMDAR). NMDAR are heteromeric glutamate-gated ion channels implicated in synaptic plasticity, learning, and memory but also in neurodegeneration and excitotoxicity (Hardingham & Bading, 2010; Parsons & Raymond, 2014; Bading, 2017).

1 RG Neuroplasticity, Leibniz Institute for Neurobiology, Magdeburg, Germany

2 Leibniz Group 'Dendritic Organelles and Synaptic Function', Center for Molecular Neurobiology (ZMNH), University Medical Center Hamburg-Eppendorf, Hamburg, Germany

3 Center for Behavioral Brain Sciences, Otto von Guericke University, Magdeburg, Germany

4 Department of Cellular Neuroscience, Leibniz Institute for Neurobiology, Magdeburg, Germany

5 German Center for Neurodegenerative Diseases (DZNE), Magdeburg, Germany

6 Institute of Neuroimmunology and Multiple Sclerosis, Center for Molecular Neurobiology (ZMNH), University Medical Center Hamburg-Eppendorf, Hamburg, Germany

7 Molecular Imaging in Neurosciences, Paul Flechsig Institute of Brain Research, Leipzig, Germany

8 Department of Systems Physiology of Learning and Memory, Leibniz Institute for Neurobiology, Magdeburg, Germany

9 Department of Biochemistry and Physiology, Faculty of Pharmacy and Food Science, University of Barcelona, Barcelona, Spain

10 Institut de Neurociències de la Universitat de Barcelona, Barcelona, Spain

11 Institute of Anatomy and Molecular Neurobiology, Westfälische Wilhelms-University, Münster, Germany

*Corresponding author. Tel: +49 0391 626394371; E-mail: akarpova@lin-magdeburg.de

**Corresponding author. Tel: +49 0391 626394181; E-mail: michael.kreutz@lin-magdeburg.de

†These authors contributed equally to this work

Aberrant and synergistic activation of GluN2B-containing NMDAR at extrasynaptic sites by glutamate and A β has been shown in AD (Bordji *et al*, 2010; Malinow, 2012; Bading, 2017; Marcello *et al*, 2018). Signaling downstream of synaptic and extrasynaptic NMDAR is tightly and antagonistically coupled to the transcription factor cAMP-responsive element-binding protein (CREB). Activation of synaptic NMDAR activates CREB through sustained phosphorylation of a crucial serine at position 133 (S133) and thereby promotes the expression of plasticity-related genes (Hardingham & Bading, 2010) critically involved in learning and memory (Barco *et al*, 2002; Carlezon *et al*, 2005). Conversely, predominant activation of extrasynaptic NMDAR leads to sustained dephosphorylation of CREB (CREB shutoff), rendering CREB transcriptionally inactive (Hardingham *et al*, 2002). Loss of CREB-dependent gene expression after extrasynaptic NMDAR activation precedes cell death and neurodegeneration; however, whether A β -induced CREB shutoff plays a role already in early synaptic dysfunction driving cognitive impairment in AD is currently unclear (España *et al*, 2010; Saura & Valero, 2011; Yiu *et al*, 2011; Teich *et al*, 2015; Bartolotti *et al*, 2016). Under the premise that activation of extrasynaptic NMDAR happens before the manifestation of clinical symptoms, it is likely that A β will interfere already at this very early stage with transcriptional regulation. Surprisingly little is known, however, on molecular mechanisms of CREB shutoff in general and in AD in particular.

In previous work, we found that the synapto-nuclear protein messenger Jacob, following long-distance transport and nuclear import, differentially transduces NMDAR signals of synaptic and extrasynaptic origin to the nucleus (Dieterich *et al*, 2008; Karpova *et al*, 2013; Panayotis *et al*, 2015; Grochowska *et al*, 2021). Activation of synaptic NMDARs leads to phosphorylation of Jacob at serine 180 (S180) (pJacob) via MAP-kinase ERK1/2, which is followed by trafficking of a pJacob/pERK1/2 signalosome along microtubules to neuronal nuclei (Karpova *et al*, 2013). Binding of the intermediate filament α -internexin protects pJacob and pERK against dephosphorylation during transport. This signalosome promotes CREB phosphorylation at S133 and hence CREB-dependent gene expression (Karpova *et al*, 2013). On the contrary, activation of extrasynaptic NMDAR leads to prominent nuclear translocation of non-phosphorylated Jacob. In this case, nuclear import is followed by stripping of synaptic contacts, simplification of dendritic arborization, and cell death (Rönicke *et al*, 2011; Gomes *et al*, 2014; Grochowska *et al*, 2017) and is correlated with CREB shutoff. The molecular identity of the signalosome assembled by non-phosphorylated Jacob is not known and the molecular mechanism of CREB shutoff is at present elusive.

In this study, we show the involvement of Jacob in A β pathology and present a molecular mechanism of CREB shutoff. In addition, we demonstrate the relevance of the identified mechanism for early synaptic failure in AD by targeting a crucial protein interaction responsible for CREB shutoff with the small chemical compound Nitarson. Taken together, the data support the hypothesis that Jacob operates as a mobile signaling hub that docks NMDAR-derived signalosomes to nuclear target sites and the results point to the significance of macromolecular protein transport from NMDAR to the nucleus for disease progression at an early stage of AD. Finally, our findings suggest that this pathway provides novel molecular entry points for interventions.

Results

CREB shutoff and reduced pJacob levels in AD patient brains

We first examined the levels of pJacob and pan Jacob in post-mortem tissue of AD patients (see Table EV1 for patient information) to provide evidence for a potential involvement of the protein in human AD pathology. Immunoblotting of a nuclear enriched fraction obtained from the temporal cortex of AD patients did not reveal a significant reduction in pan Jacob levels as compared to controls (Fig EV1A–C). However, the levels of pJacob were significantly reduced by roughly 40% (Figs 1A and B, and EV1A), indicating that nuclear import of Jacob following activation of synaptic NMDAR is diminished probably at the expense of activation of extrasynaptic NMDAR (Karpova *et al*, 2013). Expectedly, we observed significant neuronal loss in AD patients as evidenced by NeuN-immunoblotting (Fig EV1D and E). Since Jacob, unlike CREB, is only detectable in neurons (Mikhaylova *et al*, 2014), we could compare phosphorylation of nuclear Jacob normalized to total protein levels and corrected these values for NeuN content to adjust for neuronal cell loss (Fig 1C). With this measure, we observed a clear reduction of the pJacob/Jacob ratio (Fig 1C) that was correlated with the degree of CREB shutoff, which we determined following FACS sorting of NeuN-positive nuclei (Figs 1D–F and EV1F), given that CREB is expressed in both glia cells and neurons. Taken together, the data indicate CREB shutoff in human AD brains. In addition, lower levels of pJacob suggest a functional link between CREB shutoff and A β -pathology that is mediated by Jacob.

Jacob protein knockdown and gene knockout protects against A β toxicity

A β oligomers can be found in various, post-translationally modified forms, out of which the N-terminally truncated, pyroglutamylated A β _{3(pE)-42} species are prominent in the brain of AD patients (Bayer & Wirths, 2014; Kummer & Heneka, 2014). Previous work suggests that Jacob might play a role in A β -induced CREB shutoff that is elicited by activation of extrasynaptic GluN2B containing NMDAR by yet unknown mechanisms (Rönicke *et al*, 2011; Gomes *et al*, 2014; Grochowska *et al*, 2017). Knockdown of Jacob by shRNA in hippocampal neurons indeed prevented CREB shutoff induced by treatment of cultures with 500 nM A β ₁₋₄₂ or A β _{3(pE)-42} oligomers (Fig 1G and H). Similar results were obtained in organotypic hippocampal slices from Jacob/*Nsmf* knockout (–/–) mice or wild-type littermates treated with 1 μ M oligomeric A β ₁₋₄₂ for 1 h (Fig 1I–K). Basal pCREB immunofluorescence levels were not different between both genotypes; however, neurons from knockout mice, unlike the wild-type, did not display A β ₁₋₄₂-induced CREB shutoff (Fig 1J and K). Total CREB levels remained unchanged (Fig EV1G and H).

Jacob gene knockout ameliorates neuronal loss in transgenic AD mice

We next reasoned that the lack of A β -induced CREB shutoff in Jacob knockout mice could confer neuroprotection in AD. The CA1 subfield of the hippocampus is one of the areas earliest affected in AD, with pronounced neuronal loss and a decreased number of synaptic

contacts (Price *et al*, 2001; Yiu *et al*, 2011; Padurariu *et al*, 2012; Wirths & Zampar, 2020). TBA2.1 mice express A $\beta_{3(pE)-42}$ and display very early on severe CA1 neuronal loss, amyloidosis, LTP impairment, and neuroinflammation (Alexandru *et al*, 2011). We chose TBA2.1 mice because they show probably the most aggressive and prominent amyloid pathology of all transgenic AD mouse models. Western blot analysis of protein extracts from TBA2.1 mouse brain revealed that, while Jacob protein levels remained unchanged

(Fig EV11 and J), pJacob levels are decreased resulting in a reduced pJacob/Jacob ratio like in human brain (Fig EV11–L). In accordance with reports from other AD transgenic mouse lines (Caccamo *et al*, 2010; Yiu *et al*, 2011; Bartolotti *et al*, 2016), we found that TBA2.1 mice exhibit significantly reduced nuclear pCREB levels (Fig 1L and M). To directly study whether the loss of Jacob expression in neurons confers neuroprotection in TBA2.1 mice, we next crossed both lines to obtain homozygous TBA2.1 and Jacob/*Nsmf*

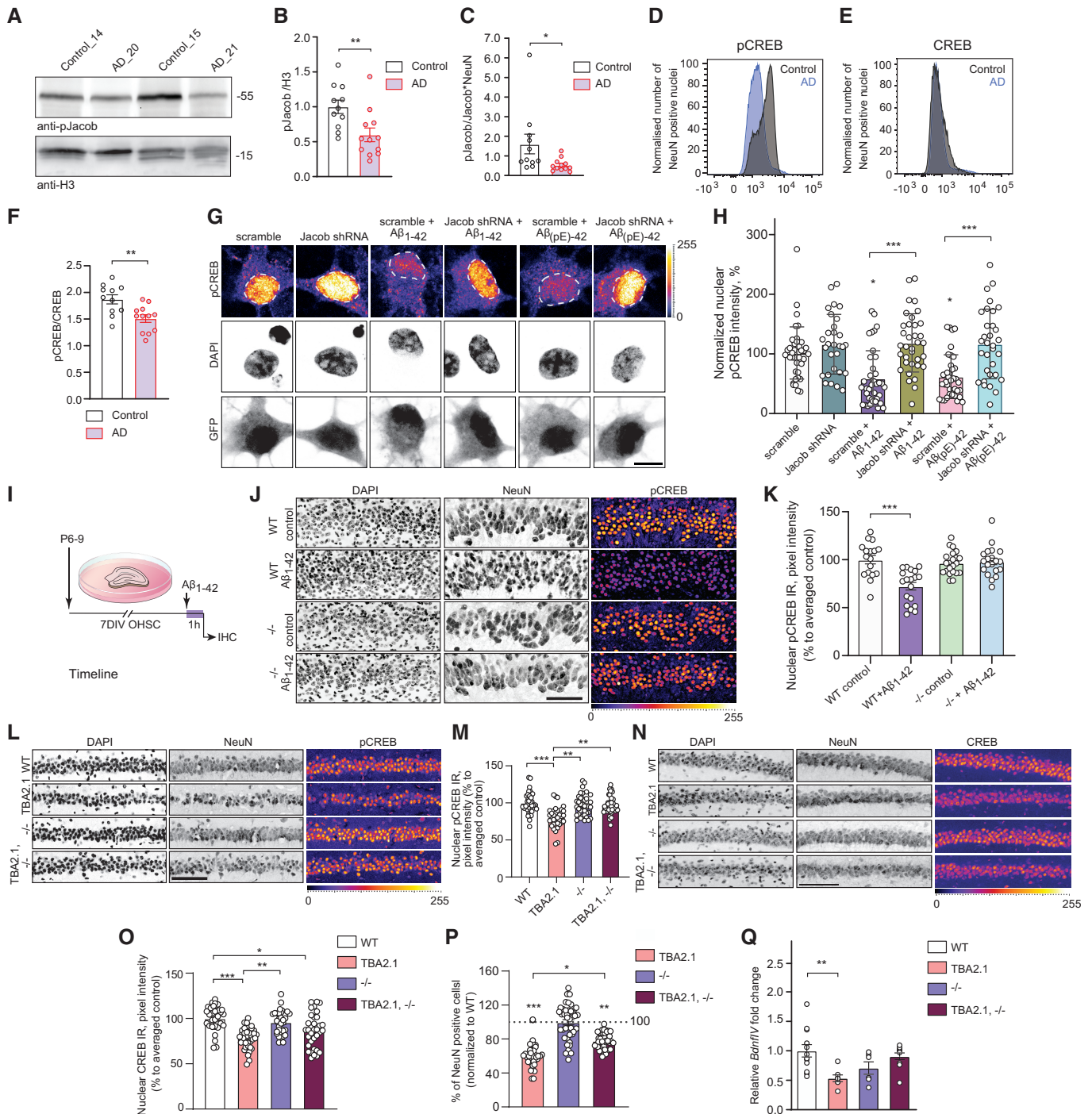


Figure 1.

Figure 1. Jacob is associated with cAMP-responsive element-binding protein (CREB) shutoff in human Alzheimer's disease (AD) and in AD mouse models.

- A–C Jacob and CREB expression in human AD. (A, B) Total pJacob protein levels and (C) The ratio of normalized levels of pJacob/jacob (panel B and EV1C) corrected by NeuN (panel EV1E) is significantly reduced in the temporal cortex of AD patients as compared to the age-matched control group. All samples are normalized to Histone3 (H3). $N = 11–12$ different subjects.
- D–F FACS of neuronal nuclei revealed significantly decreased pCREB, but not CREB, immunoreactivity in AD patients as compared to the control group. (D, E) Frequency distribution plot of neuronal nuclei immunoreactivity of (D) pCREB and (E) CREB (no statistically significant difference). (F) pCREB/CREB ratio in neuronal nuclei. $N = 11–12$ different subjects.
- G, H Jacob shRNA knockdown prevents A β -induced CREB shutoff. (G) Representative confocal images of hippocampal neurons transfected with Jacob-shRNA or scrambled (scr) shRNA control (both expressing GFP) and treated with oligomeric preparations of A β_{1-42} or A $\beta_{3(pE)-42}$. (H) Neurons transfected with a Jacob knockdown construct did not display reduction of pCREB immunofluorescence intensity after treatment with A β_{1-42} or A $\beta_{3(pE)-42}$. Bar plot of mean nuclear pCREB intensity normalized to untreated control. Scale bar: 10 μm . $N = 29–39$ nuclei from two independent experiments.
- I–K Acute (1 h) treatment with 1 μM A β_{1-42} does not induce CREB shutoff in organotypic hippocampal slices from Jacob (–/–) mice. (J) Representative confocal images of slices immunolabeled against pCREB, co-labeled with NeuN and DAPI. Scale bar: 100 μm . (K) Bar plot of pCREB, $N = 17–21$ slices.
- L, M The quantification of pCREB intensity in NeuN-positive cells revealed a statistically significant decrease in pCREB immunoreactivity in TBA2.1 but not in double transgenic animals (TBA2.1, –/–). (L) Representative confocal images of CA1 cryosections from 13 weeks old mice stained for NeuN, DAPI, and pCREB. Scale bar: 100 μm . Data represented as cumulative frequency distribution. (M) Bar plot of average hippocampal pCREB nuclear immunoreactivity normalized to WT. $N = 34–38$ hippocampal sections from 10 to 11 animals.
- N, O The quantification of CREB intensity in NeuN-positive cells revealed a statistically significant decrease in CREB immunoreactivity in Jacob/*Nsmf* knockout (–/–) and TBA2.1 \times Jacob/*Nsmf* knockout (TBA2.1, –/–) mice. (N) Representative confocal images of CA1 cryosections from 13 weeks old mice stained for NeuN, DAPI, and CREB. Scale bar: 100 μm . (O) Bar plot of CREB nuclear immunoreactivity normalized to WT. $N = 34–36$ hippocampal images from 8 to 11 animals.
- P Double transgenic TBA2.1 Jacob/*Nsmf* knockout (TBA2.1, –/–) mice display significantly lower neuronal loss compared to TBA2.1 mice. The number of NeuN-positive cells was normalized to wild-type (WT) group. $N = 36–47$ CA1 images analyzed from 10 to 12 animals per genotype. Dotted line marks value of the normalized control group –100%.
- Q Jacob knockout rescues decrease in the *BdnfIV* gene transcription. Bar plot of mean *BdnfIV* transcript levels in hippocampal homogenates normalized to β -actin as reference transcript. $N = 5–10$ hippocampi.

Data information: (G, J, L, N) Lookup table indicates the pixel intensities from 0 to 255. * $P < 0.05$, ** $P < 0.01$, *** $P < 0.001$ by (B, C, F) two-tailed Student's *t*-test or (H, K, Q) two-way ANOVA followed by Bonferroni's multiple comparisons test by (M, O, P) linear mixed-effects model followed by Tukey's multiple comparisons test. All data are represented as mean \pm SEM.

Source data are available online for this figure.

(–/–) mice. Interestingly, the double transgenic animals (TBA2.1 \times Jacob/*Nsmf* –/–) did not display CREB shutoff as evidenced by no reduction in pCREB levels (Fig 1L–O). Although we observed in all three genotypes (TBA2.1, Jacob/*Nsmf* –/–, and double TBA2.1 \times Jacob/*Nsmf* –/–) slightly decreased nuclear CREB levels (Fig 1N and O), the absence of CREB shutoff in Jacob/*Nsmf* –/– and double transgenic animals points to a key role of the protein for transcriptional inactivation at an early stage of A β -amyloidosis. Accordingly, cell loss in the dorsal CA1 region was less pronounced in double transgenic mice (on average 23%) (Fig 1P). The rescue mediated by Jacob gene knockout was also visible at the level of brain-wide network activation patterns when we imaged cerebral blood flow (CBF) in unrestrained behaving mice of all four genotypes (TBA2.1, Jacob/*Nsmf* –/–, TBA2.1 \times Jacob/*Nsmf* –/–, and wild-type (WT)) using SPECT (Kolodziej *et al*, 2014; Oelschlegel & Goldschmidt, 2020; Fig EV1M). Decreases in CBF, found in dorsal CA1 (arrow) of TBA2.1 mice when compared to wild type animals, were partially rescued in double transgenic mice (Fig EV1M). This rescue was also apparent in the lateral septum and the diagonal band, regions connected to the hippocampus (Fig EV1N). In addition, levels of BDNF mRNA transcribed from promoter IV of the *Bdnf* gene (*BdnfIV*), a synaptic plasticity-related neurotrophic factor (Spilker *et al*, 2016), whose expression is regulated by CREB in an activity-dependent manner, were decreased in TBA2.1 mice, but not in Jacob/*Nsmf* (–/–) and double transgenic animals (Fig 1Q).

Jacob gene deletion did not influence the number of astrocytes (Fig EV1O and P) and activated microglia (Fig EV1O and Q). Moreover, amyloid load, evidenced by the number of A β -positive deposits (Fig EV1R and S), was not affected as well, indicating that indirect effects of neuroinflammation or amyloid deposition do not account for the neuroprotection conferred by Jacob gene deletion.

Jacob is a direct binding partner of CREB and LMO4

These data collectively suggest that Jacob-induced CREB shutoff that we termed JaCS contributes to transcriptional inactivation of CREB in AD and we therefore next aimed to decipher underlying molecular mechanism. We first tested for a possible direct interaction between both proteins. A pull-down assay with bacterially expressed proteins revealed a direct association of both N-terminal 117-172 amino acid (aa) and C-terminal (262-532 aa) regions of Jacob to the bZIP domain of CREB (Figs 2A and EV2A–C). Accordingly, super-resolution stimulated emission depletion (STED) imaging showed nuclear Jacob in close vicinity to CREB in cultured hippocampal neurons (Fig EV2D and E). We could co-immunoprecipitate endogenous CREB from HEK293T cells following heterologous expression of Jacob (Fig EV2F) and in support of these data we found prominent *in vivo* fluorescence resonance energy transfer (FRET) efficiency when we co-expressed either full length or the N-terminal half of Jacob and a C-terminal fragment of CREB (Fig 2B–E). Of note, the N-terminal fragment of Jacob yielded significantly stronger FRET signals than the C-terminal fragment (Fig 2B–F). Finally, proximity ligation assays provided evidence for an interaction of Jacob with CREB in neuronal nuclei of hippocampal primary cultures (Fig 2G).

In a yeast two-hybrid (YTH) screen performed with the N-terminus of Jacob as bait we identified LMO4 as a binding partner (Appendix Fig S1A). LMO4 is a transcriptional co-activator of CREB (Kashani *et al*, 2006) and we therefore wondered whether the Jacob-LMO4 interaction has a role in JaCS. A region encompassing aa 117-228 of Jacob directly interacted with the LIM1 domain of LMO4 (Fig 2H, Appendix Fig S1A and B). In addition, both proteins were in close proximity to each other in neuronal nuclei as revealed

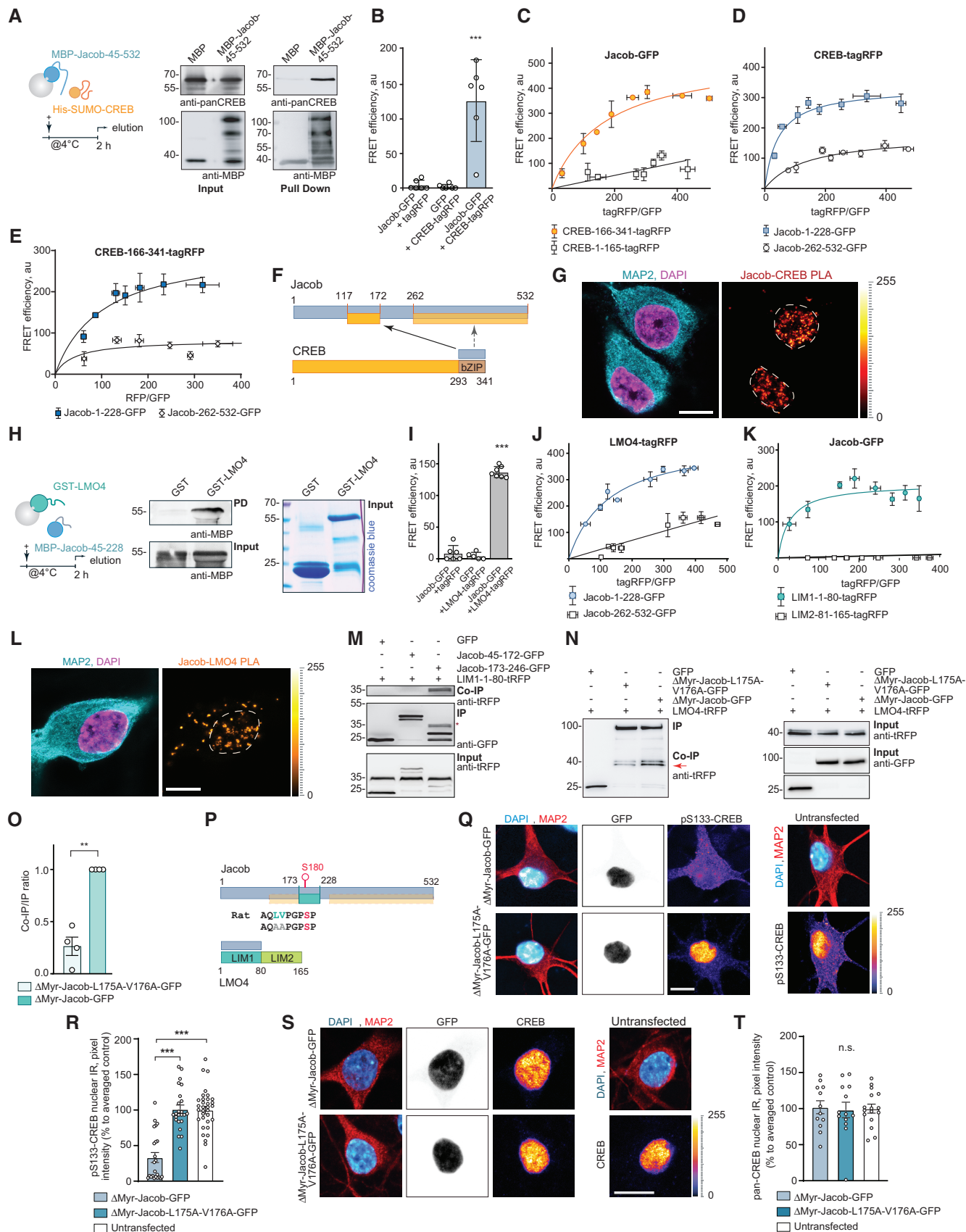


Figure 2.

Figure 2. Jacob directly associates with cAMP-responsive element-binding protein (CREB) and LMO4.

- A Pull-down assays confirm a direct interaction of MBP-Jacob-45-532 and His-SUMO-CREB.
- B Fluorescence resonance energy transfer (FRET) measurements show an association between CREB-tagRFP and Jacob-GFP. $N = 5$ independent experiments measured in triplicates.
- C–E (C) The C-terminus (CREB-166-341-tagRFP) but not the N-terminus (CREB-1-165-tagRFP) of CREB closely associates with Jacob-GFP in FRET saturation experiments. (D) Both the N- (Jacob-1-228-GFP) and the C-terminus (Jacob-262-532-GFP) of Jacob are in close proximity to CREB-tagRFP; however, the Jacob-1-228-GFP association with CREB is significantly stronger. (E) The C-terminus of CREB (CREB-166-341-tagRFP) associates prominently with the N-terminus (Jacob-1-228-GFP) and less strong with the C-terminus (Jacob-262-532-GFP) of Jacob. (C–E) FRET efficiency is presented in arbitrary units from 5 to 6 independent experiments.
- F Binding interfaces between CREB and Jacob.
- G A proximity ligation assay revealed an interaction between Jacob and CREB in primary neurons. Dashed ROIs indicate neuronal nuclei. Scale bar: 10 μm .
- H GST-LMO4 but not GST alone directly binds to MBP-Jacob-45-228. From left to right: A scheme depicting experimental procedure, image of membrane probed with anti-MBP antibody, and the Coomassie blue-stained gel showing the purity of proteins used as an pull-down input.
- I FRET experiments revealed that Jacob-GFP interacts with LMO4-tagRFP. $N = 5$ –7 independent experiments measured in triplicates.
- J, K FRET saturation experiments indicate the association of Jacob-1-228-GFP with LIM-1-80-tagRFP. FRET efficiency is presented in arbitrary units as a mean of 6 independent experiments measured in triplicates.
- L A proximity ligation assay revealed an interaction between Jacob and LMO4 in primary neurons. Scale bar: 10 μm .
- M Co-immunoprecipitation experiments to map the binding region of Jacob to the LIM1 domain of LMO4 revealed the association with Jacob-179-246-GFP, but not with Jacob-45-172-GFP (CREB-binding region).
- N, O Heterologous co-immunoprecipitation experiments between LMO4-tagRFP and nuclear ΔMyr -Jacob-GFP, ΔMyr -Jacob-L175A-V176A-GFP or GFP point to a decreased association of ΔMyr -Jacob-L175A-V176A-GFP with LMO4 as compared to ΔMyr -Jacob-GFP. $N = 4$ independent experiments.
- P Binding interfaces between Jacob and LMO4.
- Q–T A Jacob-LMO4-binding mutant expressed in the nucleus does not induce CREB shutoff. (Q, S) Representative confocal images of hippocampal neurons transfected with ΔMyr -Jacob-GFP (Jacob targeted to the nucleus) or ΔMyr -Jacob-L175A-V176A-GFP. Scale bar: 10 μm . Lookup table indicates the pixel intensities from 0 to 255. (R, T) The mean of nuclear (R) pCREB or (T) CREB immunoreactivity in Jacob-expressing neurons was normalized to non-transfected controls. $N = 23$ –33 neuronal nuclei from two independent cell cultures.

Data information: $**P < 0.01$, $***P < 0.001$ by (O) one-sample *t*-test or one-way ANOVA followed by (B, I) Bonferroni's or (R, T) Tukey's multiple comparisons test. All data are represented as mean \pm SEM.

Source data are available online for this figure.

by STED imaging (Appendix Fig S1C and D) and the LIM1 domain co-localized with cytosolic Jacob clusters following heterologous expression (Appendix Fig S1E). The association of both proteins was further confirmed by heterologous co-immunoprecipitation with tag-specific antibodies (Appendix Fig S1F) and the direct interaction was corroborated by *in vivo* FRET analysis (Fig 2I–K) and proximity ligation in hippocampal neurons points to an *in vivo* interaction (Fig 2L). Subsequent heterologous co-immunoprecipitation of Jacob fragments with the LIM1 domain indicated that the binding regions for LMO4 and CREB do not overlap (Fig 2F and M, Appendix Fig S1G). Interestingly, like other LIM1 domain-binding proteins, Jacob contains a leucine- and valine-rich stretch (Joseph *et al*, 2014). Point mutations (L175A-V176A) within this region resulted in much weaker binding (Fig 2M–O). In the previous work, we found that nuclear overexpression of non-phosphorylated Jacob leads to dephosphorylation of CREB (Dieterich *et al*, 2008). Nuclear accumulation of the LMO4 binding mutant of Jacob, however, did not induce CREB shutoff (Fig 2P–T), indicating that the association with LMO4 is instrumental for JaCS.

Jacob competes with CREB for LMO4 binding

We next asked why the association with LMO4 is crucial for JaCS. *In vivo* FRET assays and heterologous co-immunoprecipitation revealed that the LIM1 domain, which is the binding interface for Jacob (Fig 2J, K, M and P, Appendix Fig S1A, E and F), also interacts with a N-terminal fragment of CREB (Fig 3A–C). LMO4 directly binds to this region, but not to the isolated bZIP domain of CREB (Fig 3D–F, Appendix Fig S1B and G), which binds Jacob. The direct interaction with LMO4 promotes phosphorylation of S133 and thereby CREB transcriptional activity as evidenced by increased CRE-driven luciferase activity following heterologous expression of

LMO4 (Fig 3G). shRNA knockdown of LMO4 (Appendix Fig S1H–J) in neurons resulted in reduced pCREB (Fig 3H and I) but not total CREB immunofluorescence (Fig 3J and K).

Direct binding of LMO4 to CREB and Jacob raised the question whether all three proteins can assemble in a trimeric complex or whether they compete for the same binding interface. Sequential resonance energy transfer (SRET) *in vivo* indeed revealed the existence of a triple complex (Fig 3L and M). Jacob harbors a binding interface for the interaction with CREB and LMO4 at the N-terminus (Fig 2), whereas LMO4 can only associate through its first LIM1 domain either to Jacob or to CREB (Figs 2 and 3). Subsequent competition pull-down experiments confirmed competitive binding between the N-terminus of Jacob and CREB with LMO4, as shown when GST-LMO4 was coupled to the beads and increasing amounts of the N-terminal fragment of Jacob were added in the presence of CREB (Fig 3N–P). In summary, the LIM1 domain of LMO4 mediates the association either with CREB or Jacob, and Jacob is capable to displace LMO4 from the CREB complex, a mechanism that should facilitate CREB shutoff (Fig 3Q).

Protein phosphatase 1 γ and LMO4 are involved in Jacob-induced CREB shutoff

We next asked whether LMO4-binding to Jacob might be also actively involved in CREB shutoff. Protein phosphatase 1 (PP1) is a phosphatase that can dephosphorylate S133 in CREB. Jacob harbors several PP1 binding motifs, both proteins co-localize following heterologous expression (Appendix Fig S2A) and tagged Jacob co-immunoprecipitate with endogenous PP1 γ (Appendix Fig S2B). Pull-down experiments revealed a direct interaction (Fig 4A, Appendix Fig S2C) and heterologous co-immunoprecipitation experiments pointed to two binding interfaces (Fig 4B). We therefore next

addressed whether the association with PP1 γ is involved in JaCS. To this end, we expressed a phosphodeficient mutant of Jacob in the nucleus of hippocampal primary neurons (Karpova et al, 2013)

and incubated cultures with the PP1 γ inhibitor okadaic acid (OA). Interestingly, we found that treatment with OA prevented JaCS (Fig 4C and D).

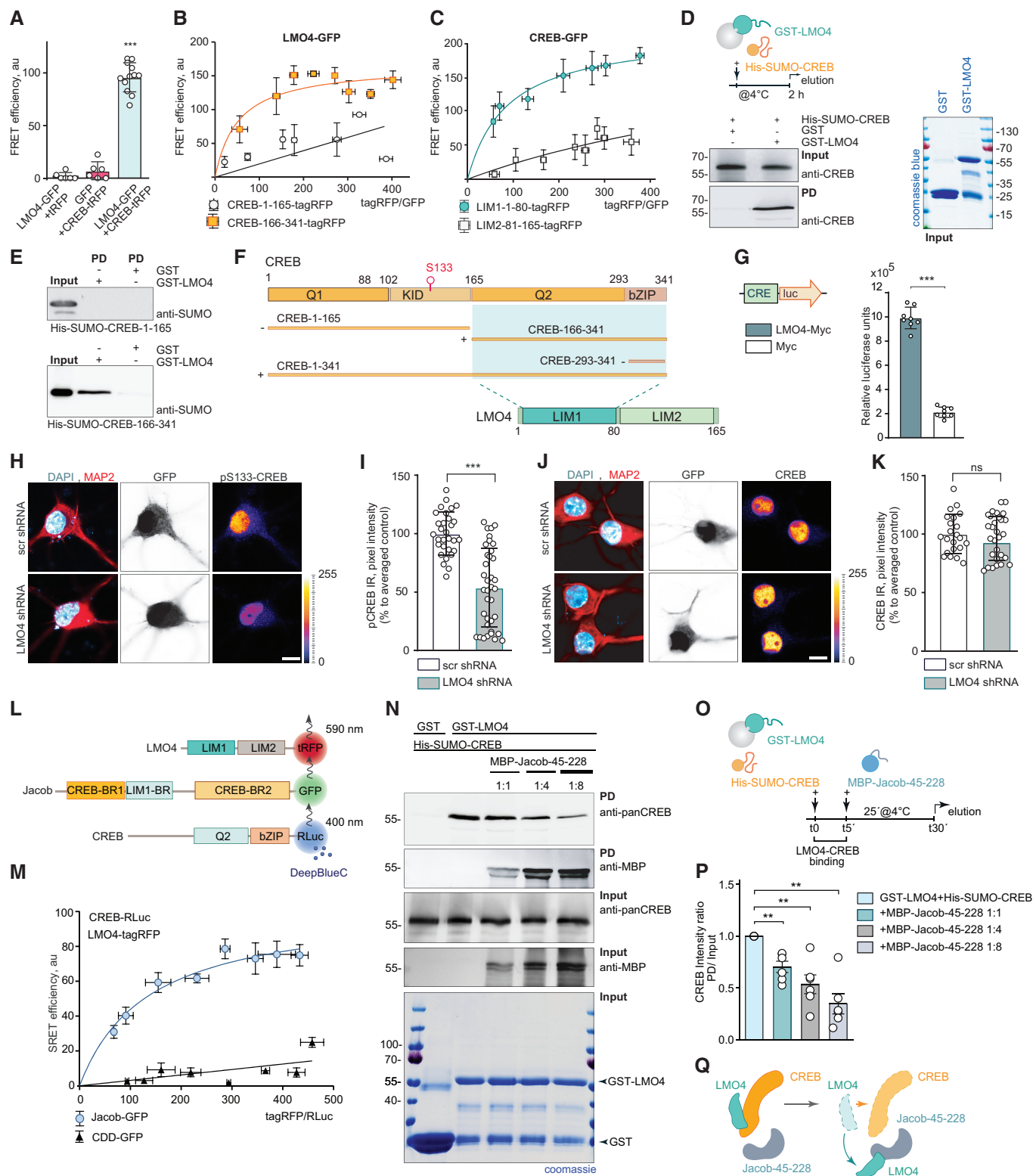


Figure 3.

Figure 3. Jacob can displace LMO4 from cAMP-responsive element-binding protein (CREB).

- A Fluorescence resonance energy transfer (FRET) measurements indicate a tight association between LMO4-GFP and CREB-tagRFP. $N = 6-12$ independent experiments measured in triplicates.
- B, C FRET saturation experiments with (B) LMO4-GFP and CREB-1-165-tagRFP or (C) CREB-166-341-tagRFP and CREB-GFP and LIM1-1-80-tagRFP or LIM2-81-165-tagRFP revealed an association between the LIM1 domain of LMO4 and the C-terminus of CREB. $N = 8$ independent experiments.
- D Recombinant His-SUMO-CREB directly binds to GST-LMO4 in pull-down experiments.
- E The interaction between CREB with LMO4 is mediated by the C-terminus of CREB (166-341 aa), but not by its N-terminus (1-165 aa), as evidenced by pull-down experiments between recombinant His-SUMO-1-165-CREB, His-SUMO-166-341-CREB, and GST-LMO4.
- F Schematic representation of CREB and LMO4 domain structure and fusion constructs used for the experiments. Light green boxes represent the interaction interface.
- G Myc-LMO4 overexpression increases CREB-dependent luciferase expression in HEK293T cells expressing luciferase under the CRE promoter. Relative luciferase units in cells overexpressing Myc-LMO4 as compared to Myc-transfected controls. $N = 8$ from two independent experiments.
- H-K Knockdown of LMO4 reduces nuclear pCREB immunoreactivity. (H, J) Representative confocal images of hippocampal neurons transfected with LMO4 shRNA construct or scrambled control (both expressing GFP under CMV promoter as a transfection control). Scale bar: 10 μm . Dot plots representing the mean of nuclear (I) pCREB or (K) CREB staining intensity normalized to scrambled control. $N = 30-37$ nuclei analyzed from at least 3 independent cell cultures.
- L, M (L) Schematic representation of constructs used in SRET experiments. "BR" stands for binding region. (M) SRET saturation experiments reveal that Jacob-GFP forms a triple complex with CREB-RLuc and LMO4-tagRFP. A caldendrin (CDD-GFP) construct was used as negative control. $N = 8$ independent experiments.
- N-Q The N-terminus of Jacob displaces LMO4 from CREB. (N) GST-LMO4 coupled to beads was preincubated with His-SUMO-CREB and subsequently incubated with an increasing amount of MBP-Jacob-45-228. (O) Schematic depicts the timeline of the competition pull-down experiment. (P) Bar graphs represent six independent experiments per condition.

Data information: (H, J) Lookup table indicates the pixel intensities from 0 to 255. ns, non-significant difference, $**P < 0.01$, $***P < 0.001$ by (G, I, K) two-tailed Student's t -test or (P) one-sample t -test or (A) one-way ANOVA followed by Bonferroni's multiple comparisons test. All data are represented as mean \pm SEM.

Source data are available online for this figure.

Phosphorylation of Jacob at S180 is induced by activation of synaptic NMDAR, whereas nuclear import of non-phosphorylated Jacob is related to extrasynaptic NMDAR activation (Karpova *et al*, 2013). Accordingly, in a CRE-luciferase activity assay, the expression of wild-type but not phosphodeficient Jacob caused increased activity (Fig 4E, Appendix Fig S2D). Furthermore, the association of a phosphodeficient mutant of Jacob to LMO4 was significantly stronger than the corresponding phosphomimetic protein (Fig 4F and G, Appendix Fig S2E and F). Phosphomimetic Jacob, unlike the non-phosphorylated protein, did not displace CREB from LMO4 bound to beads (Figs 3N-Q and 4H-J). To further test the idea that LMO4 binds to non-phosphorylated Jacob more efficiently, we applied the protein kinase inhibitor staurosporine and performed heterologous co-immunoprecipitation experiments (Fig 4K and L). We indeed found a stronger association of non-phosphorylated Jacob to LMO4 (Fig 4K and L) and concomitantly a stronger association of S180 phosphorylated Jacob to CREB (Fig 4K and L). Since Jacob directly interacts with PP1 γ (Fig 4A), we performed a pull-down assay where we observed that the association between both proteins was much stronger in the presence of LMO4 (Fig 4M and N, Appendix Fig S2E and F). Thus, non-phosphorylated Jacob, entering the nucleus following activation of extrasynaptic NMDAR, will likely displace LMO4 from the CREB complex and the subsequent association with LMO4 will enhance binding to PP1 γ , which then ultimately results in CREB shutoff (Fig 4I).

The small organoarsenic compound Nitarosone selectively blocks binding of Jacob but not of CREB to the LIM1 domain of LMO4

The molecular analysis outlined above allowed us to perform structural modeling of the binding interface between CREB, Jacob and the LIM1 domain of LMO4. To this end, we analyzed deposited peptide-bound LMO4 structures. In LMO4:LIM domain-binding protein 1 (Ldb1) (Deane *et al*, 2004) a peptide of Ldb1 binds to LMO4 by short β - β main chain formations and single hydrophobic side

chains protruding into deep pockets in each of the two LIM domains (Fig 5A). LMO4:Ldb1 highlights the relatively weak sequence preferences for peptides binding to either or both LIM domains (Fig 5A). Therefore, we performed a positional scan by computational serial mutation of each peptide residue to any of 20 aa stretches in both Jacob and CREB which let us define a search pattern of only four critical residues for potential LMO4-binding regions (Fig EV3A-D). With this approach we found eight potential binding regions in Jacob and five in CREB (Fig EV3B), for which we modeled LIM1:peptide complexes and calculated complex stability. For Jacob, we confirmed a peptide including residues 172-186 that is part of the experimentally localized LMO4 binding region. In addition, we found two overlapping peptides within the experimentally determined LMO4-binding region for CREB (Fig EV3D).

We next searched for small molecules that might selectively prevent binding of Jacob and not of CREB to LIM1 of LMO4. Here, we used ZINCPharmer, a tool that allows to define donor and acceptor atoms within the hydrophobic binding pocket (Fig 5B) and the β -strand (β_3 , Fig 5C) of LIM1 (Koes & Camacho, 2012). Several hits contained a p-nitrophenyl group (e.g., 2-[[1-(4-nitrophenyl)ethyl]amino]ethan-1-ol (ZINC37177221)) fitting to the hydrophobic binding pocket. We therefore next searched the Drugbank database (Wishart *et al*, 2006) for purchasable drugs containing this group and identified p-nitrophenylarsonic acid (Nitarosone) as promising candidate since Nitarosone fitted into the hydrophobic binding pocket of LIM1 as evidenced by AutoDock Vina (Eberhardt *et al*, 2021; Fig 5D).

To prove efficacy, specificity, and affinity of Nitarosone binding to the LIM1 domain, we next purified recombinant proteins expressed in bacteria (Fig EV3E). Isothermal titration calorimetry (ITC) revealed a single binding site in LMO4 and a K_D of 0.77 μM (Fig 5E), which is roughly matching the K_D of 0.37 μM for binding of Jacob to LMO4 (Fig 5F). These results prompted us to test the prediction that Nitarosone will only block binding of LMO4 to Jacob but not to CREB. In GST pull-down experiments, we could indeed

show that Nitarsonone completely abolished binding of Jacob to LMO4 when applied in 5× times molar excess (Figs 5G–I and EV3E). In these experiments, we immobilized 500 nM GST-LMO4, saturated

binding with 1 μM Jacob 45-228 and then applied 5 μM Nitarsonone. In contrast, even at a concentration of 20 μM, that is, in 20× times molar excess, the substance did not displace CREB from LMO4

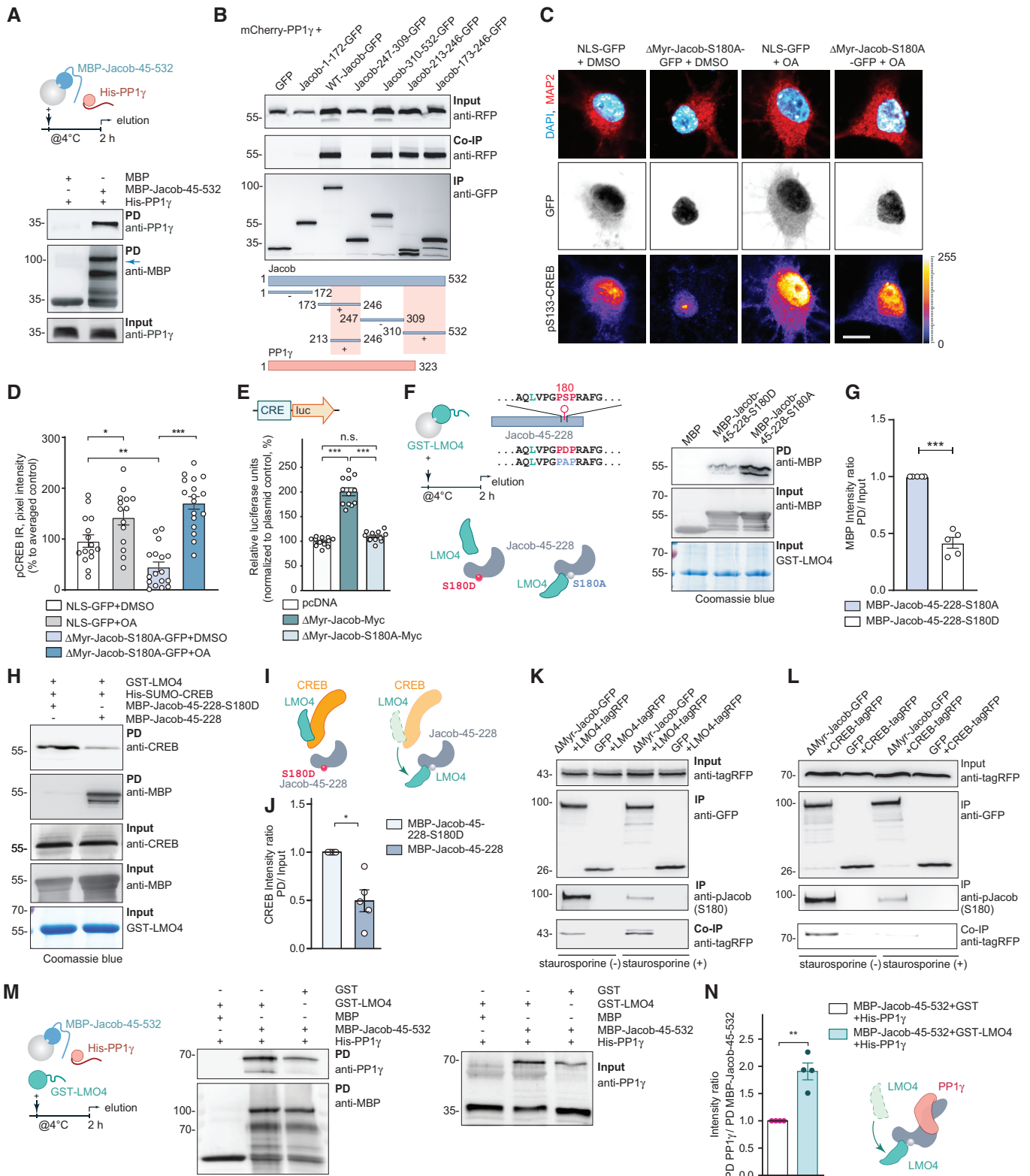


Figure 4.

Figure 4. JaCS essentially requires Jacob binding to PP1 γ .

- A Pull-down experiments confirmed a direct interaction between recombinant MBP-Jacob-45-532 and His-PP1 γ .
- B Mapping of the mCherry-PP1 γ interaction region within the Jacob sequence revealed binding of a C-terminal fragment (Jacob-310-250-GFP) as well as the N-terminal part (Jacob-173-246-GFP) where the region between 213-246 aa is sufficient for immunoprecipitation. The pink boxes in the schematic indicate binding regions.
- C, D Treatment of hippocampal primary neurons expressing phosphodeficient Jacob in the nucleus with okadaic acid (OA) rescues Jacob-induced cAMP-responsive element-binding protein (CREB) shutoff. Confocal images of pCREB immunostaining in DIV15 neurons overexpressing Δ Myr-Jacob-S180A-GFP with and without OA treatment. Scale bar: 20 μ m. Lookup table indicates the pixel intensities from 0 to 255. $N = 14-17$ nuclei analyzed from two independent cell cultures.
- E Overexpression of Δ Myr-Jacob-Myc but not the phospho-deficient mutant (Δ Myr-Jacob-S180A-Myc) positively regulates CREB-dependent luciferase expression. $N = 12$ measurements from three independent experiments.
- F, G Phosphodeficient N-terminus of Jacob (MBP-Jacob-45-228-180A) interacts with LMO4 stronger than its phosphomimetic form (MBP-Jacob-45-228-180D). (G) Quantification of MBP immunoreactivity normalized to input. Data are presented from five independent experiments.
- H-J Phosphomimetic Jacob mutant (MBP-45-228-180D) does not displace LMO4 from CREB. Recombinant GST-LMO4 was coupled to beads, preincubated with His-SUMO-CREB and subsequently incubated in 1:8 ratio with MBP-Jacob-45-228 or MBP-45-228-180D. (J) Quantification of the CREB band intensity normalized to the input. $N = 5$ independent experiments.
- K Treatment with staurosporine decreases Jacob phosphorylation level (S180), but increases its association with LMO4-tagRFP. Immunoblot of HEK293T cells extracts transfected with LMO4-tagRFP and Δ Myr-Jacob-GFP or GFP alone.
- L Treatment with staurosporine decreases the association of Jacob with CREB. Immunoblot of HEK293T cells extract transfected with CREB-tagRFP and Δ Myr-Jacob-GFP or GFP as a control.
- M, N The association of Jacob with LMO4 enhances its interaction with PP1 γ in pull-down assays. (M) PP1 γ interacts with Jacob as a dimer (70 kDa) that forms during purification. (N) Bar graph represents quantification of PP1 γ immunoreactivity normalized to MBP-Jacob. $N = 5$ independent experiments.

Data information: * $P < 0.05$, ** $P < 0.01$, *** $P < 0.001$ by (G, J, N) one-sample t -test or (E) one-way ANOVA followed by Bonferroni's multiple comparisons test or (D) two-way ANOVA followed by Bonferroni's multiple comparisons test. All data are presented as mean \pm SEM. Source data are available online for this figure.

(Figs 5J–M and EV3E). Finally, we tested the effect of 5 μ M Nitarosone administration on Jacob-LMO4 complex formation in A β -treated hippocampal primary cultures employing a proximity ligation assay. As expected, Nitarosone drastically reduced the A β -induced association of Jacob with LMO4 in neurons (Fig 5N and O).

Nitarosone application rescues A β -induced CREB shutoff as well as synapse loss and synaptic dysfunction

We next found that bath application of 10 μ M Nitarosone prevented A β -induced CREB shutoff in hippocampal primary neurons (Fig EV4A–C). The drug was either applied 30 min prior or 2 h after application of 500 nM A β for 2 h. In both conditions, we found a rescue of pCREB levels following Nitarosone administration (Fig EV4A–C), indicating that the drug will not only prevent Jacob binding in response to A β -treatment but will also displace Jacob bound to LMO4 even after A β -induced CREB shutoff. Co-application of 5 μ M Nitarosone, a dose that is already effective to interrupt the Jacob/LMO4 interaction in primary neurons (Fig 5N and O), also rescued CREB shutoff induced by application of 500 nM A β oligomers for 48 h (Fig 6A and B).

We therefore next assessed A β -induced synapse loss in dissociated hippocampal neurons that were kept for 48 h in the presence of 5 μ M Nitarosone (Fig 6C and D). A β induced a 30% reduction of synaptophysin/Shank3 puncta in these cultures (Fig 6C and D) and this synapse loss was completely prevented by Nitarosone application (Fig 6C and D). The concomitant downscaling of synaptic surface expression of GluA1 AMPA-receptors was also significantly attenuated in the presence of Nitarosone (Fig 6E and F). In control experiments, these neurons exhibited normal up-scaling of GluA1 AMPA receptors in response to silencing of neuronal activity with 1 μ M TTX application (Fig EV4D). Whole-cell patch-clamp experiments showed that reduced surface expression of GluA1 following A β treatment was accompanied by reduced miniature excitatory postsynaptic current (mEPSC) amplitude but not frequency (Fig 6G–K).

Co-application of 5 μ M Nitarosone preserved mEPSC amplitude while administration of the drug alone had no effect on both measures (Fig 6G–K).

In vivo administration of Nitarosone prevents early synaptic dysfunction and cognitive deficits in two transgenic AD mouse lines

We next administered Nitarosone *in vivo* in two transgenic AD mouse lines with amyloid pathology, TBA2.1 and 5xFAD mice. 5xFAD mice express human APP and PSEN1 transgenes with a total of five AD-linked mutations (Oakley *et al*, 2006). These mice display less rapid spread of amyloid pathology than TBA2.1 mice, with visible plaques accompanied by gliosis at 4 months of age with accompanying synaptic dysfunction and cognitive impairment. We administered Nitarosone orally with forced feeding and a defined daily dose of 50 mg/kg that was based on a conservative NOEL (no observed effect level) from several toxicology studies and the rationale to achieve an effective dose in brain tissues (see Materials and Methods and Fig 7A for experimental details).

This regime had no effect on the body weight of treated as compared to control animals (Fig EV5A and B) and on amyloid load in both mouse lines (Fig EV5C–F). However, Nitarosone administration effectively prevented CREB shutoff in both transgenic AD mouse lines in the dorsal hippocampal CA1 region following 6 weeks of treatment (Figs 7B–E and EV5G–J). In addition, early neuronal cell loss was reduced in TBA2.1 mice in comparison to vehicle-treated littermates (Figs 7F and EV5K and L) while we could not detect neuronal cell loss in CA1 of 5xFAD mice at 19 weeks of age (Fig EV5M and N). Most important, we found clearly reduced synapse loss in the stratum lacunosum moleculare in mice treated with Nitarosone in both animal models of amyloid pathology (Fig 7G–J). This is the first hippocampal region affected by amyloid pathology in many AD animal models (Kerchner *et al*, 2012; Su *et al*, 2018). Synapse loss within this region was accompanied in

TBA2.1 mice by dendritic varicosities (Fig 7K and L), another morphological feature of AD pathology (Jin *et al*, 2011; Lee *et al*, 2022). Mice treated with Nitarosone displayed significantly less dendritic varicosities (Fig 7K and L).

In accord with these findings, we observed early synaptic dysfunction in acute hippocampal slices, as evidenced by deficits in late-phase long-term potentiation (LTP), in TBA2.1 and 5xFAD mice

at postnatal week 11 and 19, respectively (Fig 8A–D). The reduced fEPSP slope in the last 30 min of recordings was rescued in slices of Nitarosone-fed mice in both AD lines (Figs 8A–D and EV50 and P), indicating a rescue of synaptic plasticity that is relevant for learning and memory (Figs 8A–D and EV50 and P).

High CREB levels have been shown to increase excitability of neurons in the lateral amygdala and the hippocampus (Zhou

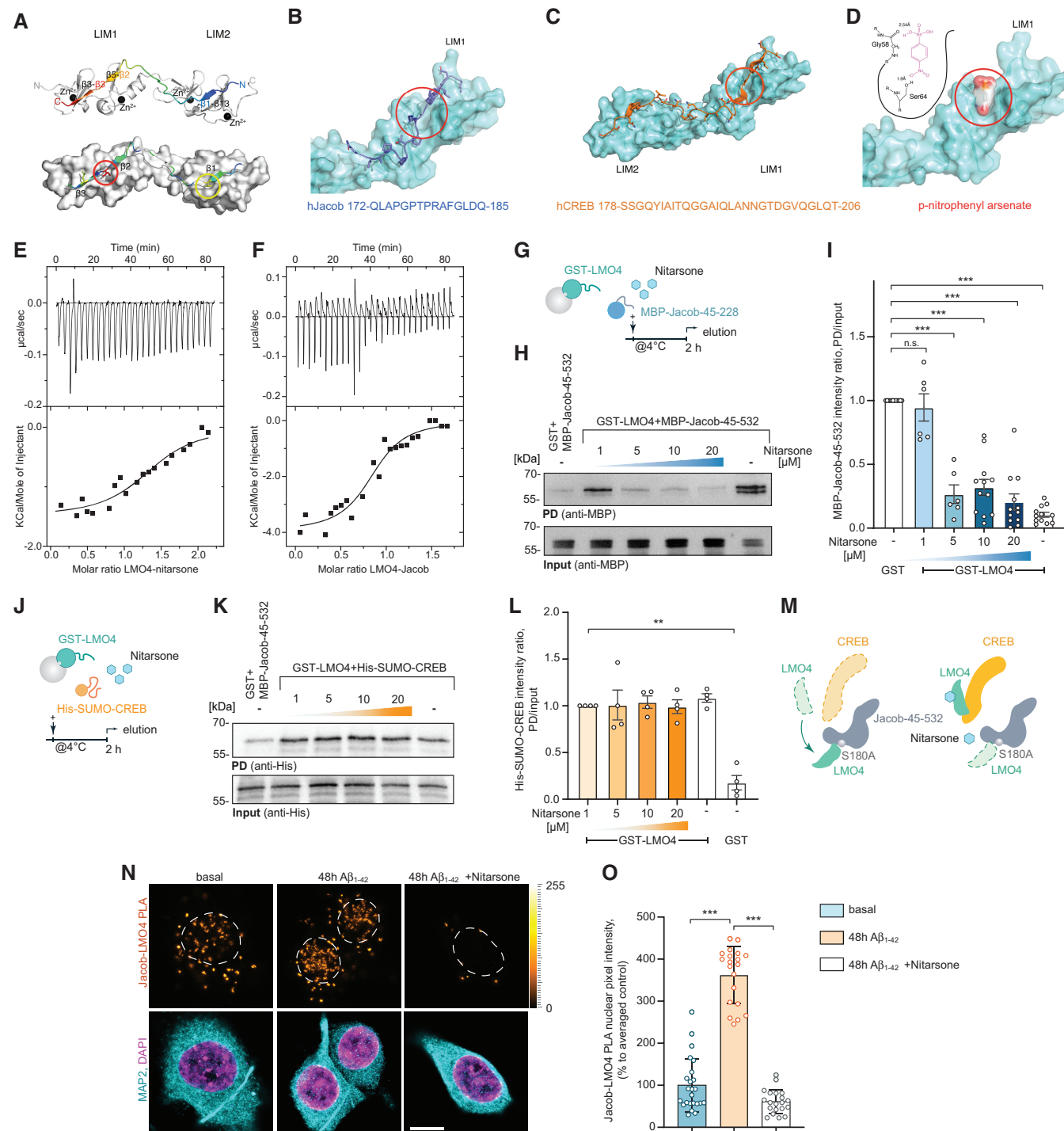


Figure 5.

Figure 5. Nitarosone disrupts LIM1-domain binding of Jacob.

- A Template structure of an LMO4:peptide complex based on fusion protein LMO4:Ldb1 LID (protein databank (PDB) ID: 1RUT). LIM1-LIM2 tandem domains are folded and stabilized by 4 zinc atoms (black spheres) and bind to a 29 residues long peptide in anti-parallel orientation. The binding occurs mainly via 3 well defined β -strands ($\beta 1$, $\beta 3$, $\beta 4$) interacting with corresponding β -strands of LMO4 ($\beta 13$, $\beta 5$, $\beta 3$). A positional alanine scan highlighted two hydrophobic binding pockets (red & yellow circle, lower panel) as hotspots of that complex allowing only residues Ile (red), Leu, Met, or Val (yellow) to be buried in each of the pockets. The peptide and the residues are rainbow color coded according to the positional alanine scan ($\Delta\Delta G$ (kcal/mol)) from 0% (blue, no side chain effect) to 100% (red, critical conserved residue).
- B hJacob residues 172–185 bind to the LIM1 domain.
- C hCreb binds to LIM1 and LIM2 similar to Ldb1.
- D Nitarosone (*p*-nitrophenyl arsonic acid) fits to the hydrophobic binding pocket of LIM1 and can form two hydrogen bonds. (B–D) Red circles mark the Nitarosone binding pocket.
- E, F Isothermal titration calorimetry (ITC) analysis of LMO4 (E) Nitarosone or (F) Jacob interaction. ITC thermograms for sequential dilutions. Upper panel presents raw data, with heat pulses illustrating exothermic binding. Lower panel depicts binding curve of integrated heat measurements with the best fit using one site binding model.
- G–I Nitarosone disrupts binding of Jacob to LMO4 in a concentration-dependent manner. (G) Bacterially expressed GST-LMO4 was immobilized on beads and pre-incubated with increasing concentrations of Nitarosone, and subsequently with MBP-Jacob-45-532. (H) MBP immunoreactivity normalized to input. $N = 6$ –12 independent experiments. (I) Representative immunoblot probed with anti-MBP antibody of input and pull-down with GST as a control.
- J–M Nitarosone does not disrupt binding of LMO4 to CREB. (J) Scheme showing experimental design. (K) Representative immunoblot probed with anti-His of input and pull-down with GST as a control. (L) Bacterially expressed GST-LMO4 was immobilized on beads and was pre-incubated with growing concentrations of Nitarosone, and subsequently with His-Sumo-CREB. His immunoreactivity normalized to input. $N = 4$ independent experiments. (M) Graphical summary of preceding experiments. Unphosphorylated Jacob displaces LMO4 from CREB. Nitarosone blocks binding of Jacob and LMO4 without affecting LMO4-CREB complex.
- N, O (N) 5 μ M Nitarosone reduced Jacob-LMO4 complex formation in A β -treated (500 nM) primary neurons as revealed by proximity ligation assay. Scale bar: 5 μ m. (O) Bar plot of normalized PLA signal intensity. $N = 20$ –24 neuronal nuclei from three cultures.

Data information: ** $P < 0.01$, *** $P < 0.001$ by (I, L) one-sample *t*-test or (O) one-way ANOVA followed by Bonferroni's multiple comparisons test. All data are presented as mean \pm SEM.

Source data are available online for this figure.

et al, 2009; Yu *et al*, 2017). Therefore, we hypothesized that Nitarosone by preventing JaCS in TBA2.1 mice should increase neuronal excitability in hippocampal CA1 neurons. Using patch-clamp recordings, we found a mild impact of genotype (transgene versus wild-type) on neuronal excitability in step current protocols (Fig 8F) probably reflecting the early stage of AD pathology in these mice. Nitarosone treatment during this early period increased the input resistance (Fig 8E and F), and reduced the rheobase (Fig 8E), and rescued the positive correlation of input resistance and action potential half width (Fig 8G; Helmstaedter *et al*, 2009) that was observed in wild-type mice in control conditions (Fig 8E–G). The latter observation is particularly interesting because following Nitarosone treatment neurons with high input resistance and high half-width within the CA1 neuronal population could serve to specifically overcome deficits in synaptic transmission and the induction of synaptic plasticity (LTP).

We therefore next determined whether treatment with Nitarosone also rescues cognitive decline in TBA2.1 and 5xFAD mice (Oakley *et al*, 2006; Alexandru *et al*, 2011). To evaluate short-term memory, we used the Y-maze object recognition task (Creighton *et al*, 2019), which minimizes contextual cues, with an interval of 3 h between training and test. Object recognition was impaired in TBA2.1 and 5xFAD mice treated with vehicle, when compared to littermate controls (Fig 8H–J). Conversely, transgenic TBA2.1 and 5xFAD mice fed with Nitarosone displayed improved discrimination performance in comparison to vehicle treated animals (Fig 8H–J). Human AD patients display impairments in object recognition, which essentially relies on proper synaptic function of CA1 neurons (Didic *et al*, 2013). Accordingly, TBA2.1 and 5xFAD mice showed deficits in novel object location and novel object recognition memory (Figs 8K–M and EV5Q–T). Treatment with Nitarosone also rescued memory in a novel location recognition as well as in a novel object recognition task with a cognitive performance comparable to vehicle-treated littermate controls (Fig 8N and O). We did not observe major differences in distance traveled as well as the number of

interactions with the objects (i.e., preference index) during the training (Fig EV5Q–T). Collectively, these data provide evidence that restoring synaptic plasticity and normal excitability with Nitarosone improve hippocampus-dependent learning and memory despite the presence of manifest amyloid pathology.

Discussion

Several lines of evidence suggest that the CA1 region, in both human patients and mouse AD models, is among the first to exhibit deficits in CREB activation, synaptic function, and neuronal excitability (Wang & Bibb, 2011; Yiu *et al*, 2011; Kerchner *et al*, 2012; Su *et al*, 2018; Wirths & Zampar, 2020). CREB might be a nodal point in the AD transcriptome network, given the central role of this transcription factor in the regulation of gene expression that is essential for synaptic plasticity, intrinsic excitability, and memory formation (Barco *et al*, 2002; Carlezon *et al*, 2005; Wang & Bibb, 2011; Alberini & Kandel, 2014; Teich *et al*, 2015). CRE-driven gene expression determines excitability of CA1 neurons (Barco *et al*, 2002; Lopez de Armentia *et al*, 2007; Alberini & Kandel, 2014), it reduces the threshold for LTP-induction in the Schaffer collateral pathway (Barco *et al*, 2002; Lopez de Armentia *et al*, 2007) and is instrumental for a switch from LTP to LTD that is characteristic for synaptic dysfunction in AD (Kim *et al*, 2001; Barco *et al*, 2002; Lopez de Armentia *et al*, 2007; Saura & Cardinaux, 2017). Despite this central role of CREB, research on amyloid pathology was largely focused on local signaling events that acutely elicit decay of synaptic function, largely ignoring the fact that molecular mechanisms underlying inactivation of CREB are likely to be first in the sequelae of events that cause synapse pathology. In consequence, such mechanisms remained elusive in AD.

Here we revealed a molecular mechanism implying A β -induced extrasynaptic NMDAR activation and nuclear import of Jacob for

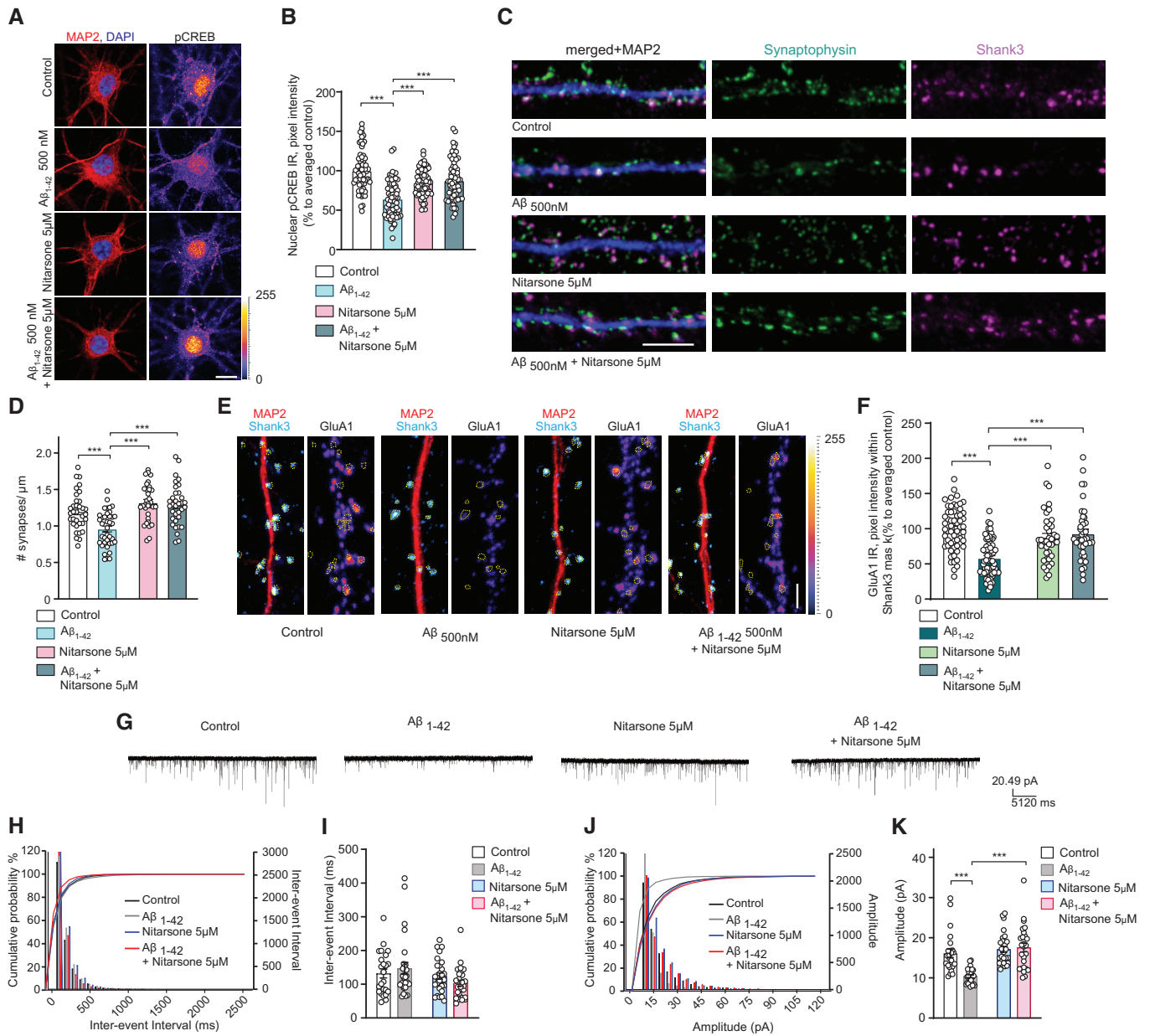


Figure 6. Nitarosone treatment rescues $A\beta_{1-42}$ -induced synaptic dysfunction.

A, B Co-application of Nitarosone prevents $A\beta$ -induced CREB shut-off. DIV16 hippocampal cultures were treated with 5 μ M Nitarosone, 500 nM $A\beta_{1-42}$ or vehicle control for 48 h and stained for pCREB, MAP2, and DAPI. (A) Representative confocal images. Scale bar: 10 μ m. (B) Nuclear pCREB immunoreactivity normalized to control. $N = 63$ –67 nuclei from three independent cultures.

C, D Treatment with Nitarosone rescues $A\beta_{1-42}$ -induced synaptic loss. DIV16 hippocampal cultures were incubated with 5 μ M Nitarosone, 500 nM $A\beta_{1-42}$, 5 μ M Nitarosone with 500 nM $A\beta_{1-42}$ or vehicle control for 48 h and stained for Shank3, Synaptophysin, and MAP2. (C) Representative confocal images of dendritic segments. Scale bar: 5 μ m. (D) Number of synaptic puncta per 1 μ m. $N = 33$ –38 dendritic segments from four independent cultures.

E, F Treatment with Nitarosone rescues $A\beta_{1-42}$ -induced decrease of synaptic GluR1-immunoreactivity within Shank3. DIV16 dissociated, hippocampal cultures were treated with 5 μ M Nitarosone, 500 nM $A\beta_{1-42}$, 5 μ M Nitarosone with 500 nM $A\beta_{1-42}$ or vehicle control for 48 h and stained for Shank3, surface GluR1, and MAP2. (E) Representative confocal images of dendritic segments. Scale bar: 5 μ m. (F) GluR1-immunoreactivity within Shank3 signal. $N = 39$ –61 of dendritic segments from four independent cell cultures.

G–K Nitarosone administration rescues mEPSC amplitude. (G) Analog traces of mEPSCs recorded in DIV16 hippocampal neurons treated with 500 nM $A\beta_{1-42}$, 5 μ M Nitarosone, 5 μ M Nitarosone with 500 nM $A\beta_{1-42}$ or vehicle control for 48 h. (H, J) Cumulative probability plots of (I) inter-event interval or (K) amplitude. Quantification of (I) inter-event-interval and (K) amplitude. $N = 24$ –28 neurons from four independent cell cultures.

Data information: (A, E) Lookup table indicates pixel intensities from 0 to 255. $***P < 0.001$ by (B, D, F, I, K) two-way ANOVA followed by Tukey's multiple comparisons test. All data are represented as mean \pm SEM.

Source data are available online for this figure.

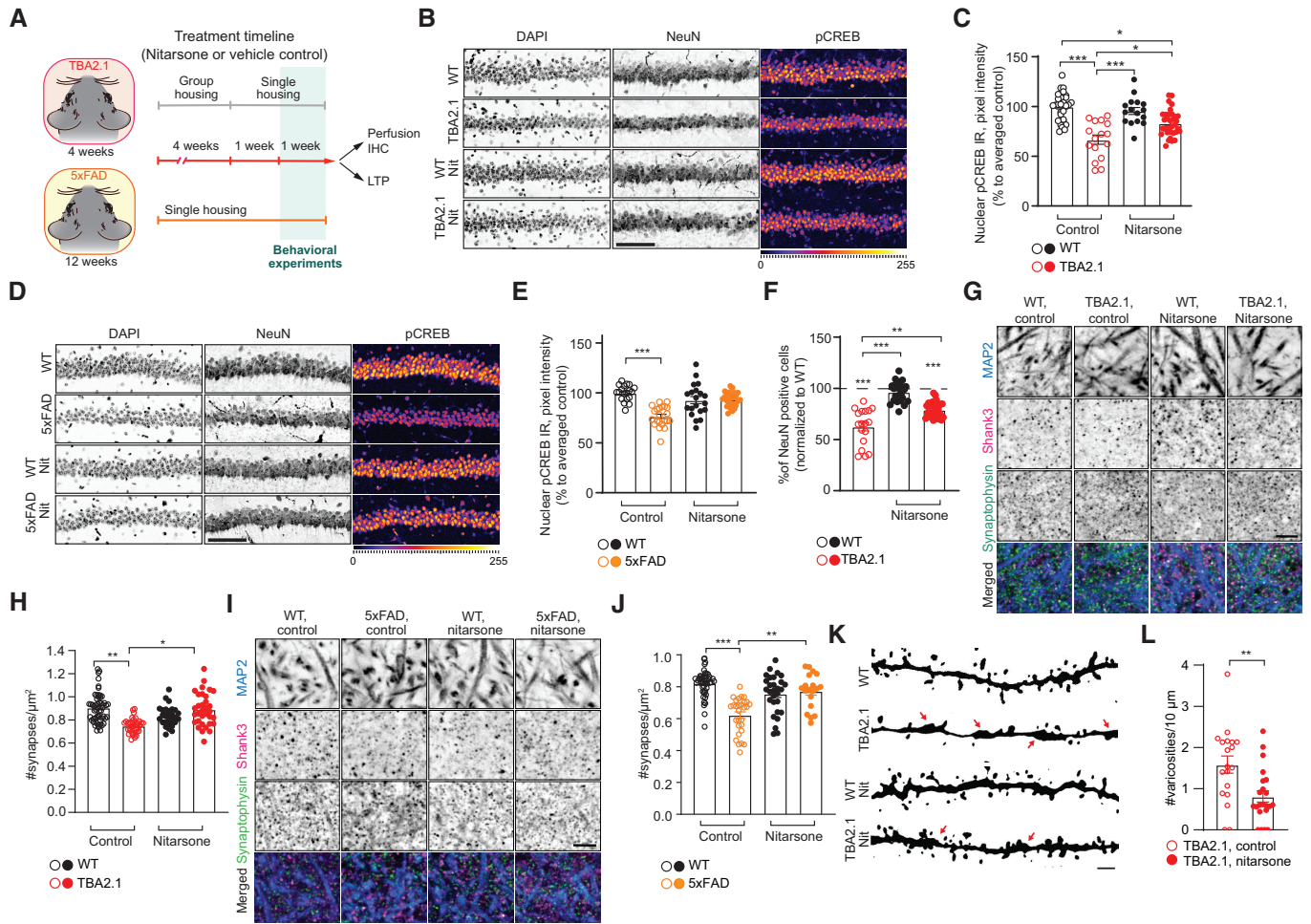


Figure 7. Oral administration of Nitarosone rescues cAMP-responsive element-binding protein (CREB) shutoff and synapse loss in TBA2.1 and 5xFAD mice.

- A Scheme representing the timeline of treatment with Nitarosone of TBA2.1 and 5xFAD mice.
- B, C Nitarosone rescues the reduction of pCREB immunoreactivity in NeuN positive cells in the CA1 region of TBA2.1 mice. (B) Representative confocal images of cryosections from 11 weeks old mice stained for NeuN, DAPI, and pCREB. Scale bar: 10 μm . (C) Bar plot of pCREB nuclear staining intensity. $N = 21\text{--}34$ hippocampal sections from 6 to 9 animals.
- D, E Nitarosone rescues the reduction of pCREB immunoreactivity in NeuN-positive cells in the CA1 region of 5xFAD mice. (D) Representative confocal images of CA1 cryosections from 18 weeks old mice stained for NeuN, DAPI, and pCREB. Scale bar: 10 μm . (E) Cumulative frequency distribution of pCREB nuclear staining intensity. $N = 22\text{--}27$ hippocampal sections from 6 to 7 animals.
- F Nitarosone reduces neuronal loss in TBA2.1 animals. The average number of NeuN-positive cells normalized to WT treated with vehicle. $N = 28\text{--}31$ CA1 images analyzed from 6 to 9 animals per genotype.
- G, H Nitarosone prevents synapse loss in SLM of CA1 of TBA2.1 mice. (G) Representative confocal images of SLM from 11-week-old mice stained for MAP2, Shank3, and Synaptophysin. Scale bar: 5 μm . (H) Number of synaptic puncta per ROI. $N = 27\text{--}55$ ROIs from 6 to 10 animals.
- I, J Nitarosone prevents synapse loss in SLM of CA1 of 5xFAD mice. (I) Representative confocal images of SLM from 18-week-old mice stained for MAP2, Shank3, and Synaptophysin. Scale bar: 5 μm . (J) Number of synaptic puncta per ROI. $N = 19\text{--}46$ ROIs from 6 to 9 animals.
- K, L Nitarosone reduces number of varicosities in SLM of CA1 of TBA2.1 mice. (K) Representative, confocal images of dendrites filled with biocytin stained from 13 weeks old mice. Arrows indicate varicosities. Scale bar: 1 μm . (L) Number of dendritic swellings per 10 μm . $N = 19\text{--}22$ dendrites from two animals per genotype.

Data information: * $P < 0.05$, ** $P < 0.01$, *** $P < 0.001$ by (C, E, F, H, J) linear mixed-effects model followed by Tukey's multiple comparisons test or (L) two-tailed Student t -test. All data are represented as mean \pm SEM. Source data are available online for this figure.

the induction of CREB shutoff (JaCS). Molecular modeling and screening for small chemical molecules subsequently led to the discovery that Nitarosone blocks binding of Jacob to the LIM1 domain. Application of Nitarosone *in vitro* and *in vivo* proved the relevance of the deciphered molecular mechanism for A β -induced synaptic pathology, CREB shutoff and the progression of synaptic and

cognitive dysfunction at a very early stage of AD. Taken together, the data support the idea that macromolecular protein transport to the nucleus has a pathophysiological role in amyloid pathology. To our knowledge, no other molecular mechanism for long-lasting transcriptional inactivation of CREB in neurons has been described yet and it is tempting to speculate that JaCS will also contribute to early

synaptic dysfunction elicited by similar mechanisms in other slowly progressing neurodegenerative diseases. Finally, a key finding of the present work is that JaCS is druggable providing novel molecular entry points for interventions.

JaCS in AD

A key aspect in this regard is the balance between activation of extra-synaptic or synaptic NMDAR and the subsequent differential

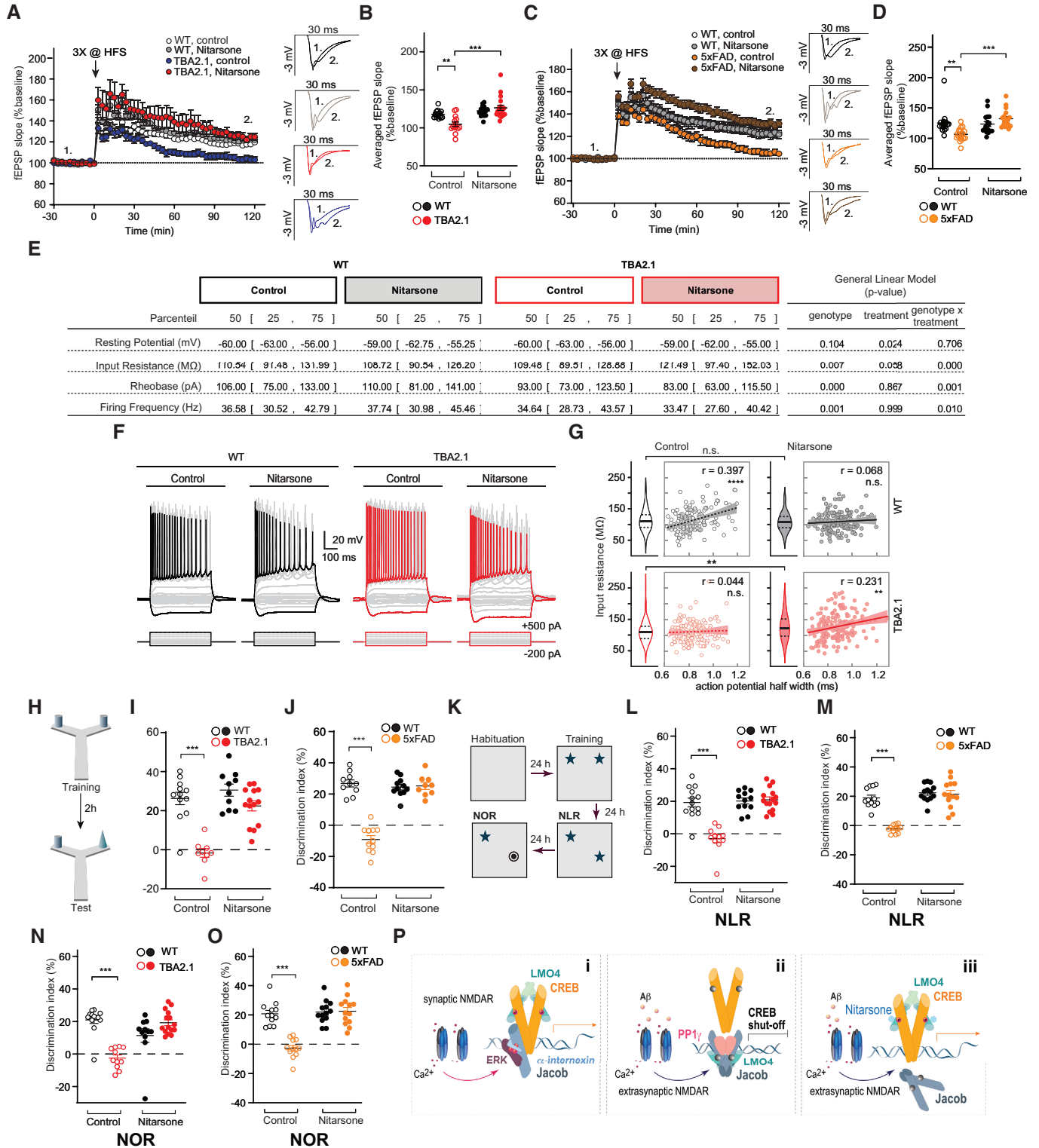


Figure 8.

Figure 8. Oral administration of Nitarsonone rescues Alzheimer's disease (AD)-related phenotypes in TBA2.1 and 5xFAD mice.

- A Nitarsonone rescues late CA1-LTP impairment in TBA2.1 mice. Insets show representative fEPSPs analog traces at indicated time points: 1 = baseline, 2 = late LTP.
- B Averaged fEPSP slopes recorded during the last 30 min. $N = 14\text{--}18$ slices from 5 to 6 mice.
- C Nitarsonone rescues late CA1-LTP impairment in 5xFAD mice. Insets show representative fEPSPs analog traces at indicated time points: 1 = baseline, 2 = late LTP.
- D Averaged fEPSP slopes recorded during the last 30 min. $N = 17\text{--}18$ slices from six mice.
- E–G Nitarsonone treatment changed basic electrophysiological properties of CA1 pyramidal neurons in TBA2.1 mice (E). (F) Step current injection evoked responses of CA1 pyramidal cells from wild-type (WT) and TBA2.1 mice in control conditions and following Nitarsonone-treatment. Gray and red traces display responses upon step current injections (see Materials and Methods, black (WT) and red (TBA2.1) traces represent -200 and 500 pA current injection). (G) Nitarsonone treatment recovers the positive correlation of input resistance and action potential half width that is observed in control conditions. Consistent with a higher availability of CREB, CA1 pyramidal neurons showed a treatment-induced increase in input resistance in TBA2.1 mice ($P = 0.0036$, post-hoc Dunn's comparison). $N = 156\text{--}166$ CA1 pyramidal neurons analyzed from six animals per genotype and treatment.
- H–J Nitarsonone rescues short-term memory impairment in Y-maze object recognition task in (I) TBA2.1 $N = 9\text{--}14$ and (J) 5xFAD mice. $N = 9\text{--}11$.
- K–M Nitarsonone rescues the impairment in novel location recognition (NLR) in (L) TBA2.1 $N = 11\text{--}15$ and (M) 5xFAD mice. $N = 12\text{--}13$.
- N, O Nitarsonone rescues the impairment in novel object recognition task (NOR) in (N) TBA2.1 $N = 11\text{--}15$ and (O) 5xFAD mice. $N = 12\text{--}13$.
- P Jacob couples the origin of NMDAR signals to CREB activity. (i) Synaptic NMDAR signaling leads to nuclear translocation of a trimeric complex consisting of pJacob, pERK1/2, and α -internexin, which promote CREB phosphorylation. (ii) Activation of NMDARs at extrasynaptic sites by A β leads to nuclear import non-phosphorylated Jacob, displacement of LMO4 from CREB, binding to PP1, and subsequent CREB shutoff. (iii) Nitarsonone specifically blocks Jacob-binding to LMO4 and thereby prevents CREB inactivation.

Data information: ** $P < 0.01$, *** $P < 0.001$ by (B, D, I, J, L–O) two-way ANOVA followed by Bonferroni's multiple comparisons test or (G) Pearson correlation coefficient. All data are represented as mean \pm SEM.

Source data are available online for this figure.

phosphorylation of S180 in Jacob. We provided evidence that Jacob directly associates with the bZIP domain of CREB irrespective of S180 phosphorylation and that this binding docks a signalosome to CREB that differs in its molecular composition depending upon the origin of NMDAR activation. We could show that binding of Jacob to LMO4 or, as shown previously, α -internexin (Karpova *et al*, 2013) determines whether the protein associates with the CREB phosphatase PP1 γ or the MAP-kinase ERK1/2, and binding to either of these adaptors is decisive whether Jacob induces inactivation of CREB or enhanced CREB-dependent gene transcription (Karpova *et al*, 2013; Figs 4 and 8P). LMO4 is reportedly a transcriptional co-activator of CREB (Kashani *et al*, 2006) and our data suggest that LMO4 might hinder dephosphorylation of S133, stabilize the CREB dimer (Figs 5 and 8P), and thereby could act as transcriptional enhancer. In the presence of amyloid pathology, Jacob likely displaces LMO4 from the CREB complex (Figs 3N–Q and 8P), and we suppose that this contributes to long-lasting CREB dephosphorylation. Thus, enhanced binding of Jacob to PP1 γ and displacement of LMO4 renders the association to LMO4 a key event for JaCS.

JaCS contributes to early synaptic dysfunction in AD

Collectively, this study suggests that long-distance protein transport from extrasynaptic NMDAR to the nucleus is an important mechanism for disease progression at an early stage in AD. We hypothesize that this stage follows the initial hyperexcitability that has been described in transgenic mice with A β pathology and AD patients (Busche *et al*, 2012; Lam *et al*, 2017; Li & Selkoe, 2020). Recent work suggests that this hyperexcitability is at least in part caused by the suppression of glutamate reuptake (Zott *et al*, 2019), which, in turn, might cause sustained activation of extrasynaptic NMDAR in response to increased ambient glutamate levels. We propose that JaCS kicks in when extrasynaptic NMDAR activation is continuous and synergistically driven by ambient glutamate and oligomeric A β (Röncke *et al*, 2011). In addition, we propose that nuclear import of Jacob might be the initial trigger for decay of synaptic function that is induced by altered gene transcription. Along these lines, we found

in previous work that the earliest morphological phenotype following nuclear accumulation of non-phosphorylated Jacob is the stripping of synaptic contacts (Dieterich *et al*, 2008; Karpova *et al*, 2013). Our observation of a recovery of a positive correlation between input resistance and action potential half width following Nitarsonone treatment in TBA2.1 mice (Fig 8G) is particularly interesting with respect to the rescue of LTP. Both parameters lead to a more effective input to output conversion of pyramidal neurons by increasing depolarization upon (synaptic) input and a more efficient transmitter release, respectively. The observed effects compensate for a reduction in synaptic strength and will facilitate the induction of synaptic plasticity. It is likely that this effect strongly contributes to Nitarsonone-mediated rescue of synaptic plasticity observed in this study.

Preserving synaptic function in AD by targeting the interaction of Jacob to LMO4

We could prove the relevance of CREB and of the proposed mechanism for A β -induced decay of synaptic function with a small chemical compound that was selected based on structural modeling of the most crucial binding interface that is involved in CREB shutoff. Thus, Nitarsonone selectively interrupts the interaction of Jacob, but not of CREB with the LIM1 domain of LMO4 and competes with a 15 amino acid short peptide in Jacob that binds to LIM1. Moreover, we identified two peptides within the LMO4-binding region of CREB. Structural modeling predicts that CREB binds with both regions to a LIM domain tandem of LMO4 with two times higher binding energy than Jacob (Fig EV3A–D). The second LIM2 domain has a weaker binding site for the CREB peptides than LIM1 as already shown for other proteins, CtIP and Lbd1 (Deane *et al*, 2004; Stokes *et al*, 2013). In concordance, we were not able to show binding of CREB to the isolated LIM2 domain, however, binding to the LIM1 of the first peptide might induce and facilitate binding of the second to the LIM2 domain. Of note, according to our model, CREB binding will not interfere with self-association of the LIM2 domain of LMO4 that has been reported previously (Deane *et al*, 2004).

The therapeutic potential of Nitarsone

Nitarsone has been in use in poultry farming as feed additive to prevent histomoniasis and to improve food utilization until 2015, when the compound was withdrawn from the market as a precaution by the FDA (<https://www.feedstuffs.com/story-fda-announces-pending-withdrawal-approval-nitarsone-45-125903>). The identified health risk, however, was very low since it was estimated that life-long consumption of turkey meat might result in increased lifetime risk of developing or dying from cancer of 0.00031% (Nachman *et al*, 2017). Nitarsone is the oxidized form of arsenilic acid, an organic arsenic compound, considered to be less harmful than inorganic arsenic like arsenic trioxide (ATO) (Fowler *et al*, 2022). However, a transformation in carcinogenic arsenic might be possible (Nachman *et al*, 2017) by anaerobic gut microbiota (Chen & Rosen, 2016) and chemical modification of the compound to prevent this transformation is difficult given its almost perfect fit to the binding pocket. On the other hand, arsenic itself has a long tradition in folk and veterinary medicine. It was used for many years to treat syphilis and other disease states (Iland & Seymour, 2013) and even though human arsenic methyltransferases in the liver convert ATO to cytotoxic arsenic (Maimaitiyiming *et al*, 2020), ATO has become the standard treatment of acute promyelocytic leukemia (Lo-Coco *et al*, 2013; de Almeida *et al*, 2021).

In light of these arguments and given that AD is a lethal neurodegenerative disease, the intervention with Nitarsone might

open up effective and selective therapeutic avenues that directly target altered NMDAR-to-nucleus communication without affecting NMDAR function at the plasma membrane, which has several detrimental side effects. A clear limitation of this study is, however, that interventions that have beneficial effects in transgenic AD mouse models might not be suitable for several reasons in humans. As a matter of fact, AD mouse models do not resemble all aspects of the human disease and the potential toxicity of Nitarsone raises concerns.

Along these lines despite strong evidence that A β -driven signaling underlies the pathological mechanisms of AD, in recent years doubts have been casted whether other pathways might contribute to the disease progression and cognitive decline (Haass & Selkoe, 2022). The failure of clinical trials with anti-amyloid therapies to show robust beneficial outcomes in AD patients on cognition has raised concerns that lowering amyloid load is sufficient to stop disease progression (Haass & Selkoe, 2022). We speculate that in light of the complexity of mechanisms in the so-called “cellular phase” of AD (Haass & Selkoe, 2022) and the notion that dissolving β -amyloid plaques with antibodies might have detrimental side effects due to release of oligomeric A β species, a combinatorial intervention with anti-A β antibodies (like Aducanumab) and targeting JaCS might be a more effective means to slow down early synaptic failure in AD. This hypothesis can be tested in future work in transgenic AD mouse models.

Materials and Methods

Reagents and Tools table

Antibodies, chemicals, kits, recombinant proteins, peptides, and software used in the study.

Reagent	Source	Identifier
Antibodies		
Anti-Jacob-87, rabbit polyclonal (against rat Jacob peptide – 187-203 aa)	Custom made by Thermo Fisher Scientific; Spilker <i>et al</i> (2016)	N/A
Anti-Jacob 1384, rabbit polyclonal (against MKADTSHDSRDSSDLQ rat Jacob peptide – 299-314 aa)	Custom made by bioGenes, Germany, Dieterich <i>et al</i> (2008)	N/A
Anti-Jacob (Jb150), rabbit polyclonal against synthetic peptides: RERSFSRSWSDPTPM (285-299 aa) and KADTSHDSRDSSDLQ (299-314 aa)	Custom made Dieterich <i>et al</i> (2008)	N/A
Anti-pJacob S180, rabbit polyclonal (against synthetic phosphorylated peptide LVPGpSPRAFG – 178-187 aa)	Custom made by bioGenes, Germany, Dieterich <i>et al</i> (2008)	N/A
Anti-CREB, 48H2, rabbit monoclonal	Cell Signaling Technology, CST	Cat.: #9197; RRID: AB_331277
Anti-CREB, D76D11, rabbit monoclonal	CST	Cat.: #4820; RRID: AB_1903940
Anti-CREB LB9, mouse monoclonal	Thermo Fisher Scientific	Cat.: #MA1-083; RRID: AB_558523
Anti-pCREB (Ser133), rabbit polyclonal	Millipore	Cat.: #06-519; RRID: AB_310153
Anti-GluR1, rabbit polyclonal	Millipore	Cat.: #ABN241; RRID: AB_2721164
Anti-PP1 gamma, rabbit polyclonal	Thermo Fisher scientific	Cat.: #PA5-21671; RRID: AB_11153939
Anti-MAP2, mouse monoclonal	Sigma-Aldrich	Cat.: #M-4403; RRID: AB_477193
Anti-NeuN, mouse monoclonal	Millipore	Cat.: #MAB377; RRID: AB_2298772
Anti-LMO4, goat polyclonal	Santa Cruz	Cat.: #sc-11122; RRID: AB_648429
Anti-GFAP, rabbit polyclonal	Sigma-Aldrich	Cat.: #G-9269; RRID: AB_477035

Reagents and Tools table (continued)

Reagent	Source	Identifier
Anti-Iba-1, guinea pig polyclonal	SySy	Cat.: #234004; RRID: AB_2493179
Anti-Amyloid β (clone 4G8), mouse monoclonal	BioLegend	Cat.: #800701; RRID: AB_2564633
Anti-Shank3, guinea pig polyclonal	SySy	Cat.: #162304; RRID: AB_2619863
Anti-Synaptophysin1, rabbit polyclonal	SySy	Cat.: #101002; RRID: AB_887905
Anti-GluR1, rabbit polyclonal	Millipore	Cat.: #ABN241; RRID: AB2721164
Anti-histone 3 (H3), rabbit monoclonal	NEB	Cat.: #4499; RRID: AB_10544537
Anti-MBP, mouse monoclonal	NEB	Cat.: #E8032L; RRID: AB_1559730
Anti-GST, rabbit polyclonal	Sigma-Aldrich	Cat.: #G7781; RRID: AB_259965
Anti-SUMO, rabbit polyclonal	Polyclonal rabbit custom made by bioGenes, Germany	N/A
Anti-GFP (B34), mouse monoclonal	BioLegend	Cat.: #902601; RRID: AB_2565021
Anti-tagRFP, rabbit polyclonal	Evrogen	Cat.: #AB233; RRID: AB_2571743
Anti-RFP, rabbit polyclonal	Rockland	Cat.: #600-401-379; RRID: AB_2209751
Duolink [®] <i>In Situ</i> PLA [®] Probe Anti-Maus MINUS	Sigma-Aldrich	Cat.: #DUO92004
Duolink [®] <i>In Situ</i> PLA [®] Probe Anti-Rabbit PLUS	Sigma-Aldrich	Cat.: #DUO92002
Duolink [®] <i>In Situ</i> PLA [®] Probe Anti-Goat PLUS	Sigma-Aldrich	Cat.: #DUO92003
Duolink [®] <i>In Situ</i> PLA [®] Probe Anti-Rabbit MINUS	Sigma-Aldrich	Cat.: #DUO92005
Anti-rabbit-AlexaFluor 488	ThermoFisher Scientific	Cat.: #A-11034; RRID: AB_2576217
Anti-rabbit-AlexaFluor 568	ThermoFisher Scientific	Cat.: #A-11036; RRID: AB_10563566
Anti-mouse-AlexaFluor 488	ThermoFisher Scientific	Cat.: #A-11001; RRID: AB_2534069
Anti-mouse-AlexaFluor 568	ThermoFisher Scientific	Cat.: #A-11004; RRID: AB_2534072
Anti-guinea pig-AlexaFluor 647	ThermoFisher Scientific	Cat.: #A-21450; RRID: AB_2535867
Anti-rabbit-IgG-HRP	Dianova	Cat.: #111-035-114; RRID: AB_2337938
Anti-mouse-IgG-HRP	Dianova	Cat.: #115-035-146; RRID: AB_2307392
Anti-guinea pig-IgG-HRP	Dianova	Cat.: #705-035-147; RRID: AB_2337022
Anti-goat AlexaFluor 568	Thermo Fisher Scientific	Cat.: #A-11057; RRID: AB_2534104
Anti-mouse Abberior STAR 635P	Abberior	Cat.: #2-0002-007-5; RRID: AB_2893232
Anti-rabbit Abberior STAR 580	Abberior	Cat.: #2-0012-005-8; RRID: AB_2893229
Bacterial and virus strains		
<i>E. coli</i> XL10Gold	Agilent	Cat.: #200314
<i>E. coli</i> BI21DE3	Invitrogen	Cat.: #C6000-03
Biological samples		
Human temporal cortex (area 22)	Brain Banking Centre of the German Brain Banking Network "BraiNet"	Paul Flechsig Institute of Brain Research (Leipzig University)
Chemicals, peptides, and recombinant proteins		
Blocking peptide for anti-LMO4 antibodies	Santa Cruz Biotechnology	SC-11122p /discontinued
Lipofectamine 2000	ThermoFisher Scientific	Cat.: #11668019
PEI	Polysciences	Cat.: #23966

Reagents and Tools table (continued)

Reagent	Source	Identifier
Nitarsonic (4-Nitrophenylarsonic acid), 98%	ABCR Gute Chemie	Cat.: #AB370306; CAS #98-72-6
MBP-PP1y	Creative BioMart	Cat.: #PPP1CC-84
Protino Glutathione Agarose 4B beads	Macherey-Nagel	Cat.: #11962462
Protease inhibitors, Complete	Roche	Cat.: #04693159001
Phosphatase inhibitors, PhosSTOP	Roche	Cat.: #04906837001
μ MACS Anti-GFP MicroBeads	Miltenyi Biotec	Cat.: #130-091-125
SPOT-Trap-MA	Chromotek	Cat.: #eta-20
SYBR Green Supermix	BIORAD	Cat.: #170882
Coelenterazine-H	ThermoFisher Scientific	Cat.: #C6780
DeepBlueC	ThermoFisher Scientific/Biotium 101252	Cat.: #50-196-4118
Human A β ₁₋₄₂ peptide	Anaspec	AS-20276
Human A β _{3(pE)-42}	Anaspec	AS-29907-01
Okadaic acid	Tocris	Cat.: #1136; CAS #78111-17-8
Tetradotoxin (TTX)	Tocris	Cat.: #1078/1
Bicuculine	Tocris	Cat.: #0130/50
MediGel Sucralose	ClearH2O	Cat.: #74-02-5022
DietGel boost Hazelnut	ClearH2O	Cat.: #72-04-5022
Staurosporine	CST	Cat.: #9935S
Critical commercial assays		
MATCHMAKER Two-Hybrid System 3	Takara	Cat.: #630489
Dual-Luciferase Reporter Assay System	Promega	Cat.: #TM040
Nuclei Isolation Kit	Sigma-Aldrich	Cat.: #NUC101
Deposited data		
Experimental models: Cell lines		
HEK293T cells		
Experimental models: Organisms/strains		
Mouse: Jacob/Nsmf ^{-/-}	Dr. Michael R. Kreutz, Spilker et al (2016)	N/A
Mouse: TBA2.1	ProBiodrug, Alexandru et al (2011)	N/A
Mouse: TBA2.1 \times Jacob/Nsmf ^{-/-}	This paper	N/A
Mouse: 5xFAD	Jackson Laboratories	Cat.: #034840-JAX
Rat: Wistar	Janvier	RjHan:WI
Oligonucleotides		
qPCR, BdnfIV, mouse, F 5'-GCAGCTGCCTTGATGTTTAC-3'	Spilker et al (2016)	N/A
qPCR, BdnfIV, mouse, R 5'-CCGTGGACGTTGCTTCTTTC-3'	Spilker et al (2016)	N/A
qPCR, B-actin, mouse, F 5'-AACCGAGCTCAGTAACAGTCC-3'	Spilker et al (2016)	N/A
qPCR, B-actin, mouse, R 5'-GTACCACCATGTACCCAGGC-3'	Spilker et al (2016)	N/A
Genotyping Jacob/Nsmf ^{-/-} , F-Jac_5574 5'-CTGAGGCTGAGACCTAGCGC-3'	Spilker et al (2016)	N/A
Genotyping Jacob/Nsmf ^{-/-} , R-Jac_6032 5'-CAGCCTCCAATACTGGCAAGAC-3'	Spilker et al (2016)	N/A
Genotyping Jacob/Nsmf ^{-/-} , R-Jac_7329 5'-GGAAGGACTTCATCTGACTG-3'	Spilker et al (2016)	N/A
Recombinant DNA		
pGL4.29[luc2P/CRE/Hygro]	Promega	Cat.: #9PIE847
pEGFP-N1	Clontech	Cat.: #6085-1
pGADT7, MATCHMAKER Two-Hybrid System 3	Takara	Cat.: #630489
GBKT7, MATCHMAKER Two-Hybrid System 3	Takara	Cat.: #630489
Jacob-1-228 in pGBKT7	Dieterich et al (2008)	N/A

Reagents and Tools table (continued)

Reagent	Source	Identifier
Jacob-1-228 in pGADT7	Dieterich <i>et al</i> (2008)	N/A
Jacob-262-532 in pGBKT7	This paper	N/A
Jacob-1-116 in pGADT7	This paper	N/A
Jacob-117-228 in pGADT7	This paper	N/A
Jacob-167-193 in pGADT7	This paper	N/A
Jacob-175-201 in pGADT7	This paper	N/A
Jacob-202-228 in pGADT7	This paper	N/A
Jacob-117-228 in pGADT7	This paper	N/A
Jacob-167-193 in pGADT7	This paper	N/A
Jacob-175-201 in pGADT7	This paper	N/A
Jacob-202-228 in pGADT7	This paper	N/A
hJacob-SPOT in pRP(Exp)-CMV (VectorBuilder)	This paper	N/A
ptRFP-N1	Evrogen	Cat.: #FP142
Jacob in ptRFP-N1	This paper	N/A
Δ Myr-Jacob in pEGFP-N1	Dieterich <i>et al</i> (2008)	N/A
Δ Myr-Jacob-S180A in pEGFP-N1	Karpova <i>et al</i> (2013)	N/A
pcDNA3.1/Myc-His	ThermoFisher Scientific	Cat.: #V80020
Δ Myr-Jacob in pcDNA3.1/Myc-His	Karpova <i>et al</i> (2013)	N/A
Δ Myr-Jacob-S180A in pcDNA3.1/Myc-His	Karpova <i>et al</i> (2013)	N/A
Jacob-1-228 in pEGFP-N1	This paper	N/A
Jacob-262-532 in pEGFP-N1	This paper	N/A
Δ Myr-Jacob-L175A-V176A in pEGFP-N1	This paper	N/A
Jacob-1-246 in pEGFP-N1	This paper	N/A
Jacob-247-532 in pEGFP-N1	This paper	N/A
Jacob-1-172 in pEGFP-N1	This paper	N/A
Jacob-173-246 in pEGFP-N1	This paper	N/A
Jacob-247-309 in pEGFP-N1	This paper	N/A
Jacob-310-532 in pEGFP-N1	This paper	N/A
Jacob-213-246 in pEGFP-N1	This paper	N/A
Jacob-173-246 in pEGFP-N1	This paper	N/A
pMAL-c5x	NEB	Cat.: #N0378
Jacob-45-228 in pMAL-c5x	This paper	N/A
Jacob-1-116 in pMAL-c5x	This paper	N/A
Jacob-117-228 in pMAL-c5x	This paper	N/A
Jacob-262-532 in pMAL-c5x	This paper	N/A
pGEX-5X-1	Sigma-Aldrich	Cat.: #GE28-9545-53
Jacob-45-228 in pMAL-c5x	This paper	N/A
Jacob-45-228-S180D in pMAL-c5x	This paper	N/A
Jacob-45-228-S180A in pMAL-c5x	This paper	N/A
pRNAT-U6.1	Gene script	Discontinued
Jacob shRNA in pRNAT 5'-AGAATGATCCGCTGTAA-3'	Karpova <i>et al</i> (2013)	N/A
Jacob scr shRNA in pRNAT 5'-AGATATAGTCGCCGCTGTAA-3'	Karpova <i>et al</i> (2013)	N/A
LMO4 in pACT2	This paper	N/A
LMO4 in pGBKT7	This paper	N/A

Reagents and Tools table (continued)

Reagent	Source	Identifier
LIM1-1-80 in pGADT7	This paper	N/A
LIM2-81-165	This paper	N/A
LMO4 in ptRFP-N1	This paper	N/A
LIM1-1-80 in ptRFP-N1	This paper	N/A
LIM2-81-165 in ptRFP-N1	This paper	N/A
LMO4 in pGEX-5X-1	This paper	N/A
pEGFP-N3	Clontech	Cat.: #6080-1
LMO4 in pEGFP-N3	This paper	N/A
LMO4 in pcDNA3.1/Myc-His	This paper	N/A
pFUGW-H1	Addgene, Fasano <i>et al</i> (2007)	Cat.: #25870
LMO4_shRNA 5'-AGATCGGTTTCACTACATC-3'	This paper	N/A
LMO4_scrambled shRNA 5'-GCTTCGCGCCGTAGTCTTA-3'	This paper	N/A
CREB in ptRFP-N1	This paper	N/A
CREB in pEGFP-N1	This paper	N/A
pRLuc-N1	PerkinElmer	Cat.: #6310200
CREB in pRLuc-N1	This paper	N/A
CREB-1-165 in ptRFP-N1	This paper	N/A
CREB-166-341 in ptRFP-N1	This paper	N/A
Champion™ pET-6xHis-SUMO	Thermo Fisher Scientific	Cat.: #K3001
CREB in pET-6xHis-SUMO	This paper	N/A
CREB-1-88 in pET-6xHis-SUMO	This paper	N/A
CREB-1-165 in pET-6xHis-SUMO	This paper	N/A
CREB-1-293 in pET-6xHis-SUMO	This paper	N/A
CREB-89-314 in pET-6xHis-SUMO	This paper	N/A
CREB-89-165 in pET-6xHis-SUMO	This paper	N/A
CREB-166-341 in pET-6xHis-SUMO	This paper	N/A
CREB-166-293 in pET-6xHis-SUMO	This paper	N/A
CREB-294-341 in pET-6xHis-SUMO	This paper	N/A
NLS in pEGFP-N1	This paper	N/A
Caldendrin in pEGFP-N1	Dieterich <i>et al</i> (2008)	N/A
PP1 gamma in pEGFP-C1	Addgene, Trinkle-Mulcahy <i>et al</i> (2001)	Cat.: #44225
mCherry-PP1 gamma	Addgene, Liu <i>et al</i> (2010)	Cat.: #45220
pET28a-His tag	Novagen	Cat.: #69864-3
PP1 gamma in pET28	This paper	N/A
Software and algorithms		
Swiss-PDB Viewer version 4.1	Guex and Peitsch (1997)	http://www.expasy.org/spdbv/
FoldX version 5	Centre for Genomic Regulation	http://foldxsuite.crg.eu/
Avogadro version 1.2	Hanwell <i>et al</i> (2012)	https://avogadro.cc/
AutoDock Vina version 1.1.2	Eberhardt <i>et al</i> (2021)	https://autodock-vina.readthedocs.io
PsiPred version 1.1.2	McCuffin <i>et al</i> (2000)	http://bioinf.cs.ucl.ac.uk/psipred/
RaptorX	Källberg <i>et al</i> (2012)	http://raptorx.uchicago.edu/
PyMol version 2.5	Schrödinger	pymol.org
MicroCal LLC ITC	MicroCal	

Reagents and Tools table (continued)

Reagent	Source	Identifier
Mini Analysis 6.0.3	Synaptosoft	http://www.synaptosoft.com/MiniAnalysis/
InVivoScope version 1.43	Bioscan	http://www.bio-scan.com/
HISPECT, version 1.4.1876	Scivis	N/A
MPI Tool software version 6.36	ATV	N/A
Osirix version 5.8.1	Rosset et al (2004)	https://www.osirix-viewer.com/
Matlab version R2017b	Math Works	https://www.mathworks.com/ ; RRID: SCR_001622
(Fiji is just) ImageJ	Schindelin et al (2012)	http://fiji.sc/ ; RRID: SCR_002285
Openview Version 1.5	Tsuriel et al (2006)	N/A
Prism Version 7 and 8	GaphPad	https://www.graphpad.com/scientific-software/prism/
Patchmaster version 2x73.5	HEKA Elektronik	http://www.heka.com/
ANY-maze video tracking version 7.0	Stoelting Co.	http://www.anymaze.co.uk/
IBM SPSS Statistics version 21	IBM	www.ibm.com
Igor Pro version 8.0.4.2	WaveMetrics	www.wavemetrics.com
Python version 5.1.5	Python	www.python.org
R studio version 4.2.1	RStudio	www.r-studio.com

Methods and Protocols

Human subjects

The temporal cortex (area 22) biospecimens (Table EV1) were provided by the Brain Banking Centre Leipzig of the German Brain-Net, operated by the Paul Flechsig Institute of Brain Research (Leipzig University). The diagnosis and staging of AD cases was based on the presence of neurofibrillary tangles (Braak & Braak, 1991) and neuritic plaques in the hippocampal formation and neocortical areas as outlined by the Consortium to establish a registry for AD (CERAD; Mirra et al, 1991) and met the criteria of the National Institute on Aging on the likelihood of dementia (The National Institute on Aging, 1997). For the study of human biospecimens, informed consent forms were obtained and autopsies were approved (GZ 01GI9999-01GI0299).

Animals

Animals were maintained in the animal facility of the Leibniz Institute for Neurobiology, Magdeburg. Jacob/*Nsmf* knockout (homozygous labeled as $-/-$) animals were characterized previously (Spilker et al, 2016). TBA2.1 (homozygous labeled as TBA2.1) mice (Alexandru et al, 2011) were a kind gift from ProBiodrug. To generate double transgenic animals (animals homozygous for both mutations labeled as TBA2.1, $-/-$) Jacob/*Nsmf* heterozygous mice were crossed with heterozygous TBA2.1 mice. The 5xFAD mice (Oakley et al, 2006) were purchased from Jackson Laboratories. All lines had a C57BL/6J background. Animal experiments were carried out in accordance with the European Communities Council Directive (2010/63/EU) and approved by local authorities of Sachsen-Anhalt/Germany (reference number 42502-2-1501 LIN, 203.m-42502-2-1112LIN, 203.m-42502-2-1280LIN). Mice were housed individually ventilated cages (Green line system, Tecniplast) under controlled environmental conditions ($22 \pm 2^\circ\text{C}$, $55\% \pm 10\%$

humidity, 12 h, light–dark cycle, with lights on at 06:00 a.m.), with free access to food and water. Unless indicated otherwise, the animals were housed in groups up to five mice per cage. All animals were genotyped prior and after the experiment. The exact information concerning sex, age, and treatments are described in method details.

Murine organotypic hippocampal slice culture

Organotypic hippocampal slice culture (OHSC) were prepared according to previously published work (Grochowska et al, 2017). Slices were obtained from P7 to P9 mice of both sexes (Jacob/*Nsmf* knockout or WT littermates as a control). Animals were decapitated, brains removed, and hippocampi dissected under a binocular. 350–400 μm thick Perpendicular slices were cut using a McIlwain tissue chopper (Mickle Laboratory Engineering). Slices were cultured on millicell membranes (three slices per membrane, Merck Milipore) in six-well plates in 1 ml of medium 50% minimal essential medium (Gibco), 25% heat inactivated horse serum (Gibco), 25 mM glucose, 2 mM glutamine, 25 mM HEPES, 1xB27 (Gibco), and penicillin/streptomycin (100 U/ml). Cultures were grown at the 37°C , 5% CO_2 , and 95% humidity. Every 3rd day, the 700 μl of the medium was exchanged.

Primary hippocampal cultures

Hippocampal and cortical cultures were prepared from Wistar rat embryos (E18) of mixed sex as described previously (Spilker et al, 2016). Briefly, dissected were digested for 15 min with trypsin at 37°C . Neurons were plated on plastic 12-well dishes (Greiner) on glass coverslips coated with poly-L-lysine (Sigma-Aldrich) at a density of 60,000 cells/well in DMEM medium (Gibco, Thermo Fisher Scientific) supplemented with 10% FCS, $1\times$ penicillin/streptomycin, and 2 mM glutamine. After 1 h incubation (at the 37°C , 5% CO_2 , 95% humidity), cells were kept in BrainPhys medium supplemented

with 1% SM1 (Stemcell Technologies), 0.5 mM Glutamine (Gibco) at 37°C, 5% CO₂, and 95% humidity.

Cell lines

HEK293T cells were maintained DMEM medium (Gibco, Thermo Fisher Scientific) supplemented with 10% FCS, 1× penicillin/streptomycin, and 2 mM glutamine at 37°C, 5% CO₂, and 95% humidity. This cell line is regularly checked for mycoplasma contamination and authenticated by STR profiling.

Antibodies, chemicals, recombinant proteins, software

The antibodies, chemicals, kits, recombinant proteins, peptides, and software can be found in the Reagents and Tools table.

Structural modeling

Structures of LMO4:peptide complexes were modeled using coordinates of LMO4:Ldb1 complex (PDBId: 1RUT) using Swiss-PDB Viewer v4.1 (Guex & Peitsch, 1997; Johansson et al, 2012). Positional refinement and calculation of free binding energy $\Delta\Delta G$ of LMO4:peptide complexes were performed by FoldX v5 (Schymkowitz et al, 2005). Donor and acceptor atoms of LMO4 L11:Jacob peptide complexes were identified using ZINCPharmer and ZINC15 (11/20) (Koes & Camacho, 2012). Nitarosone (4-Nitrophenylarsonic acid) has been geometrically optimized and generated in PDB format by Avogadro v1.2 (Hanwell et al, 2012) and used as ligand for LMO4 LIM1 by molecular docking program AutoDock Vina v1.1.2 (Eberhardt et al, 2021). Secondary structures of full-length hJacob and hCreb were predicted with PsiPred v1.1.2 (McGuffin et al, 2000). RaptorX (12/20) (Källberg et al, 2012) was used to predict the structure of Jacob C-terminus. Structures were visualized using Open-source PyMol v2.5 (pymol.org).

YTH screening

The YTH screening for Jacob interaction partners was performed using a pre-transformed human brain cDNA Library in pACT2 (Matchmaker-GAL4 Two-Hybrid II; Clontech) as described previously (Helmuth et al, 2001; Dieterich et al, 2008). The yeast strains AH109 and Y187 as a partner (both from Clontech) were used.

Jacob-LMO4 interaction was reconfirmed using fusion vectors (bait vector pGBKT7, prey vector pGADT7) using MATCHMAKER Two-Hybrid System 3 (Takara Bio Europe/Clontech, France). Co-transformed yeasts were assayed for growth on quadruple drop-out medium (SD/-Ade/-His/-Leu/-Trp) and additionally for LacZ reporter activation accordingly to the manufacturer's instructions.

Recombinant protein production

GST-tagged recombinant proteins (LMO4) were produced and purified as described previously (Dieterich et al, 2008; Karpova et al, 2013). For protein production, *E. coli* BL21 (DE3) strain was used. Following induction with 0.3 mM isopropyl-beta-D-thiogalactoside (IPTG) at 18°C, cells were pelleted by centrifugation at 6,000 g for 15 min and purified from the soluble fraction by glutathione-Sepharose chromatography (elution buffer: 50 mM Tris-HCl, 10 mM reduced glutathione, pH 8.0). For MBP-tagged recombinant proteins (Jacob fragments (in aa): 45-228, 1-116, 117-228, 262-532, 262-532, 45-228, 45-228-S180D (phosphomimetic mutant), 45-228-S180A (phosphodeficient mutant)) lysis was done in 20 mM Tris buffer (pH 7.4), 200 mM NaCl, 1 mM DTT and

1 mM ethylenediaminetetraacetic acid (EDTA). Protein was eluted with lysis buffer + 10 mM maltose. His-SUMO-tagged recombinant proteins (CREB, CREB fragments (in aa): 1-88, 1-165, 1-293, 89-314, 89-165, 166-341, 166-293, 294-341) were purified from native conditions in which lysis buffer, wash, and elution buffer all have 50 mM NaH₂PO₄ (pH 8.0) and 300 mM NaCl with various concentrations of imidazole (10, 20, and 250 mM, respectively). All protease inhibitor (Complete, Roche) was used in all mentioned buffers. MBP-tagged PP1 γ was obtained from Creative BioMart (Cat. #PPP1CC-84). The purity of the protein was checked on SDS-PAGE gels stained and Coomassie blue staining.

Isothermal titration calorimetry

LMO4-Nitarosone (98%, ABCR Gute Chemie) binding affinity was measured using VP-ITC calorimeter (MicroCal) and data were analyzed by MicroCal LLC ITC software (MicroCal). Both purified GST-LMO4 protein and Nitarosone were prepared in 25 mM Tris buffer (pH 7.4) containing 50 mM NaCl. 20 μ M GST-LMO4 or buffer control (to calculate heat of dilution) was titrated against 180 μ M Nitarosone. LMO4 and Jacob binding affinity was measured by analyzing binding isotherms for titration of 5 μ M Jacob and 40 μ M LMO4. To estimate the influence of Nitarosone on Jacob-LMO4 interaction, LMO4 protein was saturated with Nitarosone, and subsequently the Jacob protein was injected. Typically for an ITC experiment, 30 injections of 10 μ l each were made at 180 s intervals. Heat change was determined by integration of the obtained peak of differential power by the instrument. Different parameters such as binding enthalpy (ΔH), dissociation constant (K_D), and stoichiometry were calculated.

Pull-down assays

Pull-down assays performed as described previously (Dieterich et al, 2008; Karpova et al, 2013). Briefly, protein amounts ranging from 1 to 10 μ g along with the equivalent amount of the control tag protein was bound on the respective beads and was incubated with 5% bovine serum albumin (BSA) for 1 h at room temperature (RT). 200 ng–10 μ g of the second recombinant protein was incubated with the resin bound protein in 1 ml Tris-buffered saline (TBS) buffer for 1 h either at RT or 3 h at 4°C. After three washing steps with TBS buffer containing 0.2–0.5% Triton X100, the complex was eluted in 2× sodium dodecyl sulfate (SDS) sample buffer (250 mM Tris-HCl, pH 6.8, 1% (w/v) SDS, 40% (v/v) glycerol 20% (v/v) β -mercaptoethanol, 0.004% bromophenol blue).

For competition pull-down assay 20 μ g of GST-LMO4 and equimolar amounts of GST control protein were bound to glutathione beads followed by 5% BSA blocking and washing with 50 mM Tris-Cl, pH 7.5, and 150 mM NaCl. Different combinations of recombinant proteins (i.e., HIS-SUMO-CREB; 1:1 of His-SUMO-CREB and MBP-Jacob-45-228; 1:4 of His-SUMO-CREB and MBP-Jacob-45-228; and 1:8 of His-SUMO-CREB and MBP-Jacob-45-228) were incubated with GST-LMO4 and GST (control protein) immobilized on Protino Glutathione Agarose 4B beads (Macherey-Nagel). Probes were eluted with 25 μ l of 2× SDS sample buffer after incubation and washing steps (washing buffer: 50 mM Tris pH 7.4, 500 mM NaCl, 0.1% Triton X100, and protease inhibitor without EDTA).

For pull-down assays with Nitarosone 10–20 μ g of GST-LMO4 or GST control protein were immobilized on glutathione beads

followed by overnight incubation with 1–20 μM of Nitarsonone solution at 4°C. Equimolar MBP-Jacob-45-228 were added to the solution and incubated rotating for 2 h and washing was performed with 20 mM Tris-Cl (pH 7.4), 150 mM NaCl, 0.2% TritonX-100 containing phosphatase and protease inhibitors. Complex was eluted using 2 \times SDS sample buffer. A schematic showing the experimental outline of the pull-down experiments is included in the main figures.

Heterologous co-immunoprecipitation

The constructs (LMO fragments (in aa) tagged with tRFP: 1-80 or 81 with GFP, or Jacob fragments (in aa): tagged with GFP: 45-172, 173, 246; mcherry-PP1 γ (Liu *et al*, 2010) with GFP or Jacob or Jacob fragments (in aa) tagged with GFP: 1-172, 247-309, 310-532, 213-246, 173-246) were heterologously expressed in HEK293T cells. Cells were harvested in cold TBS buffer containing protease inhibitors (Roche) and phosphatase inhibitors (Roche), in a 1 g/10 ml ratio 48 h after transfection. The pelleted cells were lysed in cold RIPA buffer (50 mM Tris-HCl (pH 8.0), 150 mM NaCl, 1% NP40, 0.5% doxycycline (DOC), 0.1%, SDS, protease and phosphatase inhibitors, pH 7.4) for 1.5 h in 4°C, rotating. The lysates were subsequently centrifuged at 20,000 g for 20 min. The supernatant was incubated with 25 μl of μMACS Anti-GFP MicroBeads (Miltenyi Biotec) for 40 min in 4°C, rotating. Beads were collected with the use of μMACS magnetic column and washed twice with 400 μl of RIPA buffer and 300 μl of 20 mM Tris-HCl (pH 7.5). 60 μl of hot 2 \times sample buffer (250 mM Tris-HCl, pH 6.8, 1% (w/v) SDS, 40% (v/v) glycerol 20% (v/v) β -mercaptoethanol, 0.004% bromophenol blue) was used for protein elution.

The phospho-dependent association of overexpressed nuclear Jacob was assessed by heterologous co-immunoprecipitation from HEK293T cells pre-treated with 20 nM staurosporine (Cell Signaling Technology, Cat.: #9953S) for 3 h.

Characterization of Jacob antibodies

For initial characterization of anti-panJacob and pJacob (S180) antibodies for the detection of human protein HEK293T cells were transfected with the plasmid expressing hJacob-SPOT. Overexpressed protein was immunoprecipitated from the cell lysate using tag-specific nano-trap (SPOT-Trap-MA, Chromotek) and analyzed by WB.

Immunoblotting of brain protein extracts

Human brain samples were homogenized in a buffer containing 0.32 M sucrose, 5 mM HEPES, protease inhibitors (Sigma), and phosphatase inhibitors (Roche), in a 1 g/10 ml ratio. The homogenates were centrifuged at 1,000 g for 10 min at 4°C. The pellets were used for immunoblotting. For immunoblotting of murine samples (CA1), dissected hippocampi were homogenized with TRIS-buffered saline (25 mM Tris-HCl, 150 mM NaCl, pH 7.4 buffer in the presence of protease (Complete, Roche)), and phosphatase inhibitors (PhosSTOP, Roche). Band intensities were quantified with Fiji/ImageJ (Schindelin *et al*, 2012).

Quantitative real-time PCR

Hippocampal homogenization, RNA extraction and cDNA preparation were described previously (Spilker *et al*, 2016). *Bdnf* exon IV (F primer: 5'-GCAGCTGCCTTGATGTTTAC-3', R primer: 5'-CCGTGGA CGTTTGCTTCTTTC-3') and β -actin (reference gene, F primer: 5'-AA

CGCAGCTCAGTAACAGTCC-3', R primer: 5'-GTACCACCATGTACC CAGGC-3') cDNA were amplified using the iScript RT-PCR iQ SYBR Green Supermix (BIORAD, Cat.: #170882) in a quantitative polymerase chain reaction (qPCR) detection system (LightCycler LC480, Roche). The sequences are indicated in the Reagents and Tools table. The relative expression levels were analyzed using the $2^{-\Delta\Delta\text{Ct}}$ method with normalization relative to β -actin.

Cell based co-recruitment assay

HEK293T cells were transfected with the following constructs: Jacob-1-228 tagged with GFP with tRFP or LMO4 or LMO4 fragments (in aa): 1-165, 1-80, 81-165; PP1 γ tagged with GFP (Trinkle-Mulcahy *et al*, 2001) and mCherry (Liu *et al*, 2010) or ΔMyr -Jacob tagged with tRFP. On the following day, cells were fixed with 4% PFA, permeabilized with 0.1% TX-100 in 1xPBS for 10 min, stained with DAPI and mounted. Z-stack with 300 nm step size was taken with 512 \times 512 pixels format using a Leica TCS SP8-STED system. Maximal intensity images from three optical sections were generated for representative images.

FRET and SRET assays

For FRET experiments, HEK293T cells were transiently co-transfected with MaxPEI (Polysciences, Cat.: #23966), with different combinations of two constructs of interest tagged with donor (GFP: LMO4, CREB, Jacob, Jacob fragments (in aa): 1-228, 262-532) or acceptor (tagRFP: LMO4, LMO4 fragments (in aa): 1-80, 81-165, CREB, CREB fragments (in aa): 1-165, 166-341), with constant concentration of cDNA of donor and increasing concentration of acceptor. FRET was performed as described previously (Carriba *et al*, 2008). For SRET measurements, transfected cells were resuspended in Hank's balanced salt solution supplemented with 10 mM glucose (Sigma-Aldrich). Triple-transfected (CREB-Rluc:Jacob-GFP:LMO4-tagRFP) cell suspension was used to perform the three measurements: (i) The LMO4-tagRFP expression level was assessed by the tagRFP fluorescence intensity, (ii) The CREB-Rluc expression level was estimated by CREB-Rluc luminescence determined 10 min after the addition of coelenterazine-H (5 μM), (iii) For SRET, the cells were incubated with 5 μM of Deep-BlueC (Molecular Probes). The measurements were done with Mithras LB940 (Berthold Technologies) equipped with detection filters at 400 and 590 nm. Net SRET was defined as [(long-wavelength emission)/(short-wavelength emission)] – Cf, where Cf corresponds to [(long-wavelength emission)/(short-wavelength emission)] for cells expressing CREB-Rluc:Jacob-GFP:LMO4-tRFP.

Luciferase assay

HEK293T cells stably expressing luciferase under the CRE promoter (vector pGL4.29[luc2P/CRE/Hygro], Promega) were transfected for 24 h and lysed with the lysis buffer (25 mM Tris-phosphate, 2 mM DTT, 2 mM 1,2-diaminocyclohexane-N,N,N',N'-tetraacetic acid, 10% glycerol, 1% TX-100, pH 7.8). The luciferase activity was measured with the Dual-Luciferase Reporter Assay System (Promega) on a (FLUOstar Omega, BMG Labtech).

Animal perfusion and immunohistochemistry

Animals were anesthetized with ketamine/xylazine (Medistar) and transcardially perfused with 0.9% saline followed by 4% PFA. The brains were post-fixed in 4% PFA in PBS overnight, followed by immersion in 0.5 M sucrose for 24 h and then 1 M sucrose for

another 1–2 days or until the brains were sunken down. The brains were snap-frozen and cut into 35 μm thick coronal cryosections (Leica CM3050S, Leica-Microsystems). The sections were blocked in a buffer (0.3% TX-100, 10% NGS in PBS) for 30 min at RT, and incubated with primary antibodies diluted in the blocking solution, overnight at 4°C. Secondary antibodies were applied for 2 h at RT. Sections were counterstained with DAPI and mounted in Mowiol 4-88 (Merck Chemicals). For the detection of A β , the heat-based antigen retrieval method was used. For anti-A β staining, following permeabilization, brain sections were immersed into 10 μM sodium citrate solution (Fluka, pH = 9) for 30 min at 80°C. Imaging of nuclear pCREB/CREB immunoreactivities in cryosections was performed using a Leica TCS SP5 system (Leica-Microsystems). Images were acquired sequentially with a HCX ApoL20x/1.0 water objective, optical zoom 4. Sections were imaged with constant laser/detector settings along the z-axis with 400 nm step in a 512 \times 512 pixel format.

OHSC stimulation and immunocytochemistry

For A β -induced CREB shutoff A β_{1-42} oligomeric solution was prepared as described in Grochowska *et al* (2017). Briefly, the A β_{1-42} peptide film (Anaspec) was re-suspended in 2 μl DMSO (Sigma-Aldrich), sonicated for 5 min, diluted with F12 medium (Gibco) to final concentration of 50 μM , sonicated for 10 min, and left for oligomerization at 4°C, on. 7 DIV OHSC were treated with 1 μM of A β_{1-42} oligomers for 1 h, fixed for 1 h at RT in 4% PFA/4% sucrose. After fixation, the slices were washed, permeabilized with 0.4% TX-100, and treated with 50 mM NH $_4$ Cl for 30 min. Subsequently, the samples were blocked for 1 h at RT in 10% normal goat serum (NGS) in PBS. Next, the slices were incubated for 72 h with primary antibody followed by incubation with the secondary antibody for 24 h. Following counterstaining with 4',6-diamidino-2-phenylindole (DAPI; Vectashield/Biozol), slices were mounted in Mowiol 4-88 (Merck Chemicals).

Primary cultures transfection and stimulation

Hippocampal neuronal cultures were transfected with plasmid cDNA using Lipofectamine2000 (Thermo Fisher Scientific) following the manufacturer's instructions. For LMO4 knockdown, cells were expressing shRNA (5'-AGATCGGTTTCACTACATC-3') for 5 days; for Jacob knockdown 4 days. For CREB shutoff experiments, hippocampal neurons were transfected at DIV15 with NLS or ΔMyr -Jacob or ΔMyr -Jacob-L175A-V176A tagged with GFP or GFP and fixed after 24 h. For the experiment with OA (Tocris), cells were treated for 20 min with 2 μM OA 1 day post-transfection. The target sequences for LMO4 and NLS-Jacob knockdown (Spilker *et al*, 2016) as well as scrambled controls are indicated in the Reagents and Tools table. For A β -induced CREB shutoff experiments, A β oligomers (Anaspec) were prepared as described previously (see previous section and Grochowska *et al*, 2017). Transfected neurons were treated with 500 nM A β_{1-42} or A $\beta_{3(\text{pE})-42}$. Nitarosone was diluted in distilled water. The concentration and duration of treatments are indicated in the figure legends.

Immunostaining of primary neurons

Primary neuronal cultures were fixed with 4% PFA/4% sucrose solution for 10 min at RT, washed with PBS, and permeabilized with 0.2% TX-100 in PBS for 10 min. Then, cells were incubated for

1 h in blocking solution (2% glycine, 0.2% gelatine, 2% BSA, and 50 mM NH $_4$ Cl (pH 7.4)) and primary antibodies were applied overnight at 4°C. Next, the coverslips were incubated with secondary antibodies diluted 1:500. Coverslips were mounted with Mowiol 4-88 (Merck Chemicals). For detection of Jacob-CREB and Jacob-LMO4 co-localization in STED imaging, a heat-based antigen retrieval protocol was used.

For assessing surface expression of AMPA receptors, dissociated hippocampal neurons were incubated for 10 min at RT with anti-GluA1 antibody diluted in Tyrode's buffer (128 mM NaCl, 5 mM KCl, 1 mM MgCl $_2$, 2 mM CaCl $_2$, 4.2 mM NaHCO $_3$, 15 mM HEPES, 20 mM glucose, pH 7.2–7.4), rinsed, and fixed for 10 min at RT with 4% PFA-sucrose, and subsequently stained with other antibodies as described above.

STED microscopy

STED images were obtained using a Leica TCS SP8 STED 3 \times equipped with pulsed White Light Laser (WLL) and diode 405 nm for excitation and pulsed depletion laser 775 nm and Leica HC ApoCS2 100 \times /1.40 oil objective. MAP2 and DAPI were acquired in confocal mode. The pixel size for all images was 20–23 nm (XY-plane). The Z-step was 150 nm. STED and confocal images were deconvolved using Deconvolution wizard (Huygens Professional, SVI), with optimized iteration method. Intensity profiles were created in Fiji/ImageJ.

Proximity ligation assay

For proximity ligation between Jacob and CREB in primary neurons in conditions of basal glutamatergic transmission, coverslips were incubated with primary anti-Jacob (rb) and anti-CREB (ms) antibodies overnight at 4°C. For the detection of Jacob-LMO4, PLA cultures were treated with A β for 48 h either alone or in the presence of Nitarosone (5 μM). Then, cells were fixed with 4% PFA and incubated with anti-Jacob (rb) and anti-LMO4 (goat) antibodies overnight at 4°C. After washing of coverslips with Duolink wash buffer A (Sigma-Aldrich), they were incubated with Duolink PLA probes PLUS and MINUS in a humidity chamber for 1 h at 37°C. For ligation of the probes, coverslips were again washed with buffer A and then incubated with ligase for 1 h at 37°C. For the amplification step, coverslips were washed with buffer A and then incubated with polymerase and Duolink FarRed Detection Reagent for 100 min at 37°C. Finally, coverslips were washed two times with Duolink wash buffer B and in PBS prior to incubation with MAP2-488 antibodies for immunocytochemistry and DAPI counterstaining. Coverslips were mounted with Mowiol 4-88. Images were acquired with a 63 \times (Leica) objective lens along the z-axis with 300 nm z-step in a 1,024 \times 1,024-pixel formats at 8-bit image depth with at least two times frame average at 400 Hz laser frequency using the SP8 CLSM system (Leica-Microsystems, Mannheim, Germany) equipped with white light laser (WLL).

Neuronal nuclei isolation and flow cytometry

Nuclei were isolated with a Nuclei Isolation Kit (Sigma Aldrich, Cat.: #NUC101) according to the manufacturer's protocol. Nuclei were fixed with ice-cold methanol for 10 min. 0.5% Triton for permeabilization and 10% normal donkey's serum for blocking were used followed by 1 h RT incubation with respective primary and, subsequently, secondary antibodies (see the Reagents and Tools

table). Nuclei were counterstained with Hoechst33342 (1:500, ThermoFisher Scientific, Cat.: #H3570). Samples were measured with a BD LSR II flow cytometer (BD Biosciences) and analyzed with FlowJo (LLC).

Whole-cell patch-clamp recording in slices

Hippocampal coronal brain slices (300 μm) were obtained from TBA2.1 mice, as described before (Justus *et al*, 2017) in four groups of mice: wild-type littermates and TBA2.1 mice treated with sucrose; wild-type littermates and TBA2.1 mice following Nitarosone treatment. Slices were kept at RT for up to 8 h in ACSF solution of the following composition in: 125 mM NaCl, 3 mM KCl, 1.25 mM NaH_2PO_4 , 26 mM NaHCO_3 , 2.6 mM CaCl_2 , 1.3 mM MgCl_2 , 15 mM glucose (supplied with 95% O_2 , 5% CO_2).

Whole cell patch-clamp recordings were performed in the CA1 area of the hippocampus in ACSF solution using borosilicate glass (GB150F-8P, Science Products) with pipette resistance in the range 3–6 M Ω . The internal solution contained: 140 Mm K-gluconate, 7 Mm KCl, 5 Mm HEPES-acid, 0.5 Mm MgCl_2 , 5 Mm phosphocreatine, and 0.16 Mm EGTA and was implemented with Biocytin (Sigma-Aldrich). The signals were acquired with either an BVC-700A amplifier (setup 1, Dagan) or an ELC-03XS (setup 2, NPI) amplifier at 50 kHz via a LIH 8 + 8 interface (HEKA) and Igor Pro software (Version 8.0.4.2, WaveMetrics). The mean series resistance was 21.3 ± 0.2 M Ω (mean \pm SEM). Recordings were performed at the temperature of 33°C. Membrane potential was not corrected for the liquid junction potential. No difference in membrane potential was observed between the experimental groups. For the investigation of the electrophysiological properties, neurons were held at a membrane potential of -65 mV by current injection. First, a step current injection protocol was performed, consisting of 500 ms step pulses with of -200 pA, -100 pA, -50 pA, -30 pA, -20 pA, -10 pA, $+10$ pA, $+20$ pA, $+30$ pA, $+50$ pA, $+100$ pA, $+200$ pA, $+300$ pA, $+400$ pA and $+500$ pA. For estimation of rheobase, 500 ms square pulse currents were injected with increasing amplitudes in steps of 2 pA until an action potential was generated.

The input resistance (IR) was calculated using -30 pA to $+30$ pA step-wise current injections as the slope of the relationship of the injected current and the steady state voltage response (Justus *et al*, 2017). Recordings were analyzed using Python (Version 5.1.5) and Igor Pro (V. 8.0.4.2, WaveMetrics). Statistical analysis was conducted using Prism 8 for Windows (Prism version for Windows, GraphPad Software) and IBM SPSS Statistic (Version 21).

SPECT-imaging of CBF

Mice (3 months of age, both sexes) were intravenously injected with $^{99\text{m}}\text{TcHMPAO}$ via chronically implanted catheters in the right external jugular vein. Jugular vein catheter implantation and preparation of the $^{99\text{m}}\text{TcHMPAO}$ injection solution were done as described in Kolodziej *et al* (2014). For tracer injection, the catheter was extended by a polyethylene (PE) tube (BioMedical Instruments, 60 cm, prefilled with 150 μl 0.9% NaCl) and connected to a syringe containing 130–170 MBq/330 μl of freshly prepared $^{99\text{m}}\text{TcHMPAO}$ -solution. Injections were made at flow rates of 33 $\mu\text{l}/\text{min}$ during periods of 15 min. During this time, the animals were awake and freely moving. After injection, animals were anesthetized (4–1.5% isoflurane, 800 ml/min O_2) and transferred to the SPECT/CT-scanner. The injected $^{99\text{m}}\text{Tc}$ activity was calculated by determining

the amounts of $^{99\text{m}}\text{Tc}$ that had remained in the syringe and in the extension tube by using a radionuclide calibrator (Aktivimeter Isomed 2010, Nuklear-Medizin-Technik Dresden GmbH). Co-registered head SPECT/CT-scans were made using a four-head NanoSPECT/CT (Mediso). CT scans were made at 45 kVp, 177 μA , with 180 projections, 500 ms per projection and 96 μm spatial resolutions, reconstructed (InVivoScope 1.43) at isotropic voxel-sizes of 100 μm . SPECT scans were made using 10-pin-hole mouse brain apertures with 1.0 mm pinhole diameters, providing a nominal resolution of < 0.7 mm. In all, 24 projections were acquired during a scan time of 1 h. Axial FOV was 20.9 mm. Photopeaks were set to the default values for $^{99\text{m}}\text{Tc}$ (140 keV \pm 5%). SPECT images were reconstructed (HISPECT, v 1.4.1876, SCIVIS) at an isotropic voxel output size of 250 μm . The co-registered SPECT/CT-images were aligned to a reference MR (MPI Tool software, v6.36, ATV; Dorr-Steadman-Ullmann-Richards-Qiu-Egan (40 micron, DSURQE)) and SPECT brain datasets were global mean normalized using ImageJ. Further data processing and calculation of group means and differences and statistical analyses were done using ImageJ and Matlab (R2017b). Results were illustrated with Osirix (v. 5.8.1) (Rosset *et al*, 2004).

Nitarosone feeding regime

Nitarosone (98%, ABCR Gute Chemie) was prepared in aliquots of 15 mg/850 μl (350 μl dH_2O , 500 μl MediGel Sucralose, Clear H_2O) to be used within 5 days. Mice were treated with Nitarosone (50 mg/kg body weight) or vehicle (sucrose solution) once a day per os for a total of 6–7 weeks. For TBA2.1 mice (both sexes), treatment started at the age of 4 weeks. The animals were group housed and force fed for 4 weeks. Afterwards, they were single housed with voluntary feeding (Nitarosone or vehicle mixed into a gel paste, DietGel boost Hazelnut, Clear H_2O). The animals were forced-fed when no uptake of paste was observed. Treatment in 5xFAD male mice started at the age of 12 weeks. Here, animals were single housed with voluntary feeding right away. The animals were forced-fed when no uptake of paste was observed. Behavioral experiments were conducted for both lines during the 6th week of Nitarosone treatment. During the course of the 7th week of treatment, animals were either subjected to perfusion to obtain their brains for subsequent immunohistochemistry or they were culled to obtain native brains for electrophysiological recordings.

Open-field test

Locomotor activity was assessed using the open-field test, performed in a square arena (45 \times 45 \times 45 cm) made of black Plexiglas and dimly illuminated. The animals were placed in the center of the arena, and were left to explore it for 10 min. The sessions were video recorded, and the distance traveled in the maze as well as the speed was tracked with ANY-maze Software 7.0 (Stoelting Co). Data were analyzed in 1 min bins.

Novel object recognition and location

The hippocampus-dependent memory was assessed using a novel object location and novel object recognition tasks. Assays were performed as described elsewhere (Andres-Alonso *et al*, 2019). Briefly, training and testing were done in an open-field square arena made out of plastic (50 cm \times 50 cm). The mice were habituated in the empty arena for 20 min. Subsequently, two identical objects were

introduced to the maze and the animals could explore the objects in two training sessions, 20 min each. 2 h afterwards, in the memory test phase, one object was replaced with an unfamiliar, unknown object (novel object recognition). Afterwards, the location of one object was changed (novel object recognition). During all sessions, the amount of time the animals explored the objects was recorded, and a discrimination index was calculated using the formula $DI = [(T_{\text{new}} - T_{\text{familiar}})/(T_{\text{new}} + T_{\text{familiar}})] \times 100$. The arena was cleaned with 5% ethanol before and after each animal was tested.

Y-maze object recognition

Y-maze Object Recognition short-term memory task was performed according to Creighton *et al* (2019). During training session, two identical objects (3D printed rectangle) were placed at the end of arms B and C and the animal was left to explore both objects for 10 min. To assess short-term memory, retrieval performance was tested 3 h after training with one of the familiar objects replaced by a novel one (wooden cube). The mice were placed in the arena, and had 5 min to explore both objects. During both sessions, the time animals explored the objects was scored, and a discrimination index was calculated, in the same manner as for the novel object recognition test.

Image analysis of murine brain sections

All quantifications were done within the distal CA1 region of the hippocampus. Fiji/ImageJ software (Schindelin *et al*, 2012) was used to calculate maximum intensity projection from five optical sections for each channel. CREB and pCREB immunoreactivity of every single nucleus in a 100 μm stretch was measured in arbitrary units of pixel intensity. ROIs were defined based on NeuN and DAPI. The neuronal loss was quantified based on NeuN staining (the number of neurons/CA1 length). For the quantification of microglia and astrocytes the number of cells based on overlaid DAPI and Iba-1 or GFAP signal was quantified within the rectangular ROI. A β plaques were counted in the region where the neuronal loss was quantified. For the quantification of synaptic density, the openview (Tsurie *et al*, 2006) software was used.

Image analysis of hippocampal cultures

For quantitation of nuclear staining intensity (pCREB or CREB), somatic regions were sequentially scanned using the 63 \times objective (Leica) in both: Leica TCS SP8-STED and Leica TCS SP5 systems. Image format was set either to 1,024 \times 1,024 or 512 \times 512 with optical zoom 4. Average intensity images from three optical sections (z-step 300 nm) were generated and intensity measurements were performed within the ROIs defined by DAPI. The values were normalized to the mean intensity of the control group. Unprocessed images were analyzed using Fiji/ImageJ software (Schindelin *et al*, 2012). For visualization of the quantified channel, a fire look-up table (LUT) was used.

Synaptic density was quantified in secondary dendrites using Fiji/ImageJ (Schindelin *et al*, 2012). The number of synaptophysin and Shank3-positive puncta was divided by the length of the dendritic segment. Intensity of the GluA1 channel was measured in ROIs defined by a Shank3 mask as a readout for surface AMPAR expression. All analysis was performed on raw, unprocessed images. For some representative images, linear contrast enhancement (histogram normalization) was applied equally for all

groups. The figures were created with Adobe Illustrator or Photoshop software.

Statistical analysis

All analysis was performed by a researcher blind to experimental groups (treatments, genotypes, transfected constructs). Statistical analysis was performed in Prism 8.0 (GraphPad) with the exception of SPECT data analysis where the Matlab (R2017b), and whole-cell patch-clamp recording where IBM SPSS Statistic (Version 21) are used. To choose the appropriate statistical analysis, a normality test (Shapiro–Wilk test) was performed. For normally distributed data, the parametric test was chosen: two-tailed Student's *t*-test (comparison of two groups) or one-way ANOVA (multiple groups with one parameter) or two-way ANOVA (multiple groups with two parameters). Nested data (immunohistochemistry analysis of cryosections from mouse brains) were analyzed with (generalized) linear mixed-effects model (*lmer* function of the *lme4* R package (Bates *et al*, 2015)) using R Studio (Version 4.2.1) with Tukey multiple comparison *post hoc* analysis carried out using the *emmeans* package (Lenth *et al*, 2020). For not normally distributed data, Mann–Whitney (comparison of two groups) or Kruskal–Wallis test was used (multiple groups). The type of statistical test used for each experiment, significance levels and the *n* numbers are reported in the corresponding figure legends. Merged values are represented as mean \pm SEM. For qPCR data (Ct values) and immunohistochemistry data (staining of cryosections) were subjected to Dixon's or Grubb's outlier test.

Data availability

This study includes no data deposited in external repositories.

Expanded View for this article is available [online](#).

Acknowledgements

The authors gratefully acknowledge the professional technical assistance of M. Marunde, C. Borutzki, S. Hochmuth, K. Böttger, T. Stöter, and O. Kobler. We would like to thank Dr. Schilling and Probiobdrug for the generous gift of the TBA2.1 mouse line and Dr. Głow for the help with virus production. We would like to thank Dr. A.V. Failla from the UKE Microscopy Imaging Facility (DFG Research Infrastructure; RI_00489) CNI. This work was supported by grants from the Deutsche Forschungsgemeinschaft (DFG) (Kr 1879/9-1/FOR 2419, FOR 5228 RP6; Kr1879/10-1; CRC 1436 TPA02, TPA04 and Z01; Research Training Group 2413 SynAGE, TPA3), BMBF “Energi” FKZ: 01GQ1421B, The EU Joint Programme—Neurodegenerative Disease Research (JPND) project STAD (FKZ: 01ED1613) and Leibniz Foundation SAW 2017, 2018, 2019 “Neurotranslation,” SyMetAge and “SynERCA” to MRK. People Programme (Marie Curie Actions) of the European Union's Seventh Framework Programme FP7/2007-2013/under REA grant agreement no. [289581], H2020 Priority Excellent Science, Marie Skłodowska-Curie Actions (MSCA) MC-ITN NPlast to KMG, MRK. DFG CRC 779 TPB8, FOR 5228 RP6 and CRC 1436 TPA02 to AK. U.S. Alzheimer's Association, grant Ref. No. AARFD-17-503612 to GNB. DAAD/CAPES scholarship, Alexander-von-Humboldt Foundation (99999.001756/2014-01), federal state of Saxony-Anhalt and the European Regional Development Fund (ERDF 2014 - 2020), Project: Center for Behavioral Brain Sciences (CBBS) Neuronetwork (ZS/2016/04/78113, ZS/2016/04/78120) to GMG, DFG GRK1167 scholarship to RK. Open Access funding enabled and organized by Projekt DEAL.

Author contributions

Katarzyna M Grochowska: Data curation; investigation; visualization; methodology; writing – original draft; writing – review and editing.
Guilherme M Gomes: Investigation; methodology; writing – original draft; writing – review and editing. **Rajeev Raman:** Investigation; methodology; writing – review and editing. **Rahul Kaushik:** Investigation; methodology.
Ljudmila Sosulina: Investigation; methodology; writing – review and editing. **Hiroshi Kaneko:** Investigation; methodology; writing – review and editing. **Anja M Oelschlegel:** Investigation; methodology; writing – review and editing. **PingAn Yuanxiang:** Investigation; methodology; writing – review and editing. **Irene Reyes-Resina:** Investigation; methodology; writing – review and editing. **Gonca Bayraktar:** Investigation; methodology; writing – review and editing. **Sebastian Samer:** Investigation; methodology; writing – review and editing. **Christina Spilker:** Investigation; writing – review and editing. **Marcel S Woo:** Investigation; methodology; writing – review and editing. **Markus Morawski:** Investigation; methodology; writing – review and editing. **Jürgen Goldschmidt:** Investigation; methodology; writing – review and editing. **Manuel A Friese:** Resources; methodology; writing – review and editing. **Steffen Rossner:** Resources; investigation; writing – review and editing. **Gemma Navarro:** Investigation; methodology. **Stefan Remy:** Resources; investigation; methodology; writing – review and editing. **Carsten Reissner:** Investigation; methodology; writing – review and editing. **Anna Karpova:** Data curation; supervision; funding acquisition; investigation; visualization; methodology; writing – original draft; project administration; writing – review and editing.
Michael R Kreutz: Conceptualization; resources; data curation; supervision; funding acquisition; writing – original draft; project administration; writing – review and editing.

Disclosure and competing interests statement

KMG, GMG, AMO, AK, CR, and MRK are named inventors of the patent application No. EP22166017.

References

- Alberini CM, Kandel ER (2014) The regulation of transcription in memory consolidation. *Cold Spring Harb Perspect Biol* 7: a021741
- Alexandru A, Jagla W, Graubner S, Becker A, Bäuscher C, Kohlmann S, Sedlmeier R, Raber KA, Cynis H, Röncke R *et al* (2011) Selective hippocampal neurodegeneration in transgenic mice expressing small amounts of truncated A β is induced by pyroglutamate-A β formation. *J Neurosci* 31: 12790–12801
- Andres-Alonso M, Ammar MR, Butnaru I, Gomes GM, Acuña Sanhuesa G, Raman R, Yuanxiang P, Borgmeyer M, Lopez-Rojas J, Raza SA *et al* (2019) SIPA1L2 controls trafficking and local signaling of TrkB-containing amphisomes at presynaptic terminals. *Nat Commun* 10: 5448
- Bading H (2017) Therapeutic targeting of the pathological triad of extrasynaptic NMDA receptor signaling in neurodegenerations. *J Exp Med* 214: 569–578
- Barco A, Alarcon JM, Kandel ER (2002) Expression of constitutively active CREB protein facilitates the late phase of long-term potentiation by enhancing synaptic capture. *Cell* 108: 689–703
- Bartolotti N, Segura L, Lazarov O (2016) Diminished CRE-induced plasticity is linked to memory deficits in familial Alzheimer's disease mice. *J Alzheimers Dis* 50: 477–489
- Bates D, Mächler M, Bolker B, Walker S (2015) Fitting linear mixed-effects models using lme4. *J Stat Softw* 67: 1–48
- Bayer TA, Wirths O (2014) Focusing the amyloid cascade hypothesis on N-truncated Abeta peptides as drug targets against Alzheimer's disease. *Acta Neuropathol* 127: 787–801
- Bordji K, Becerril-Ortega J, Nicole O, Buisson A (2010) Activation of extrasynaptic, but not synaptic, NMDA receptors modifies amyloid precursor protein expression pattern and increases amyloid- β production. *J Neurosci* 30: 15927–15942
- Braak H, Braak E (1991) Neuropathological staging of Alzheimer-related changes. *Acta Neuropathol* 82: 239–259
- Busche MA, Chen X, Henning HA, Reichwald J, Staufenbiel M, Sakmann B, Konnerth A (2012) Critical role of soluble amyloid- β for early hippocampal hyperactivity in a mouse model of Alzheimer's disease. *Proc Natl Acad Sci USA* 109: 8740–8745
- Caccamo A, Maldonado MA, Bokov AF, Majumder S, Oddo S (2010) CBP gene transfer increases BDNF levels and ameliorates learning and memory deficits in a mouse model of Alzheimer's disease. *Proc Natl Acad Sci USA* 107: 22687–22692
- Carlezon WA Jr, Duman RS, Nestler EJ (2005) The many faces of CREB. *Trends Neurosci* 28: 436–445
- Carriba P, Navarro G, Ciruela F, Ferre S, Casado V, Agnati L, Cortes A, Mallol J, Fuxe K, Canela EI *et al* (2008) Detection of heteromerization of more than two proteins by sequential BRET-FRET. *Nat Methods* 5: 727–733
- Chen J, Rosen BP (2016) Organoarsenical biotransformations by *Shewanella putrefaciens*. *Environ Sci Technol* 50: 7956–7963
- Creighton SD, Mendell AL, Palmer D, Kalisch BE, MacLusky NJ, Prado VF, Prado MAM, Winters BD (2019) Dissociable cognitive impairments in two strains of transgenic Alzheimer's disease mice revealed by a battery of object-based tests. *Sci Rep* 9: 57
- de Almeida LY, Pereira-Martins DA, Weinhäuser I, Ortiz C, Cândido LA, Lange AP, De Abreu NF, Mendonza SES, de Deus Wagatsuma VM, Do Nascimento MC *et al* (2021) The combination of Gefitinib with ATRA and ATO induces myeloid differentiation in acute promyelocytic leukemia resistant cells. *Front Oncol* 11: 686445
- Deane JE, Ryan DP, Sunde M, Maher MJ, Guss JM, Visvader JE, Matthews JM (2004) Tandem LIM domains provide synergistic binding in the LMO4: Ldb1 complex. *EMBO J* 23: 3589–3598
- Didic M, Felician O, Barbeau EJ, Mancini J, Latger-Florence C, Tramon E, Ceccaldi M (2013) Impaired visual recognition memory predicts Alzheimer's disease in amnesic mild cognitive impairment. *Dement Geriatr Cogn Disord* 35: 291–299
- Dieterich DC, Karpova A, Mikhaylova M, Zdobnova I, Konig I, Landwehr M, Kreutz M, Smalla KH, Richter K, Landgraf P *et al* (2008) Caldendrin-Jacob: a protein liaison that couples NMDA receptor signalling to the nucleus. *PLoS Biol* 6: e34
- Eberhardt J, Santos-Martins D, Tillack AF, Forli S (2021) AutoDock Vina 1.2.0: new docking methods, expanded force field, and python bindings. *J Chem Inf Model* 61: 3891–3898
- Espana J, Valero J, Minano-Molina AJ, Masgrau R, Martin E, Guardia-Laguarta C, Lleó A, Gimenez-Llort L, Rodriguez-Alvarez J, Saura CA (2010) Beta-amyloid disrupts activity-dependent gene transcription required for memory through the CREB coactivator CRTCL1. *J Neurosci* 30: 9402–9410
- Fasano CA, Dimos JT, Ivanova NB, Lowry N, Lemischka IR, Temple S (2007) shRNA knockdown of Bmi-1 reveals a critical role for p21-Rb pathway in NSC self-renewal during development. *Cell Stem Cell* 1: 87–99
- Forner S, Baglietto-Vargas D, Martini AC, Trujillo-Estrada L, LaFerla FM (2017) Synaptic impairment in Alzheimer's disease: a dysregulated symphony. *Trends Neurosci* 40: 347–357

- Fowler BA, Chou CHS, Jones RL, Costa M, Chen C-J (2022) Chapter 3 - Arsenic. In *Handbook on the Toxicology of Metals*, Nordberg GF, Costa M (eds), 5th edn, pp 41–89. Amsterdam: Academic Press
- Gomes GM, Dalmolin GD, Bär J, Karpova A, Mello CF, Kreutz MR, Rubin MA (2014) Inhibition of the polyamine system counteracts beta-amyloid peptide-induced memory impairment in mice: involvement of extrasynaptic NMDA receptors. *PLoS One* 9: e99184
- Grochowska KM, Yuanxiang P, Bär J, Raman R, Brugal G, Sahu G, Schweizer M, Bikbaev A, Schilling S, Demuth HU et al (2017) Posttranslational modification impact on the mechanism by which amyloid-beta induces synaptic dysfunction. *EMBO Rep* 18: 962–981
- Grochowska KM, Bär J, Gomes GM, Kreutz MR, Karpova A (2021) Jacob, a synapto-nuclear protein messenger linking N-methyl-D-aspartate receptor activation to nuclear gene expression. *Front Synaptic Neurosci* 13: 787494
- Guex N, Peitsch MC (1997) SWISS-MODEL and the Swiss-PdbViewer: an environment for comparative protein modeling. *Electrophoresis* 18: 2714–2723
- Haass C, Selkoe D (2022) If amyloid drives Alzheimer disease, why have anti-amyloid therapies not yet slowed cognitive decline? *PLoS Biol* 20: e3001694
- Hanwell MD, Curtis DE, Lonie DC, Vandermeersch T, Zurek E, Hutchison GR (2012) Avogadro: an advanced semantic chemical editor, visualization, and analysis platform. *J Chem* 4: 17
- Hardingham GE, Bading H (2010) Synaptic versus extrasynaptic NMDA receptor signalling: implications for neurodegenerative disorders. *Nat Rev Neurosci* 11: 682–696
- Hardingham GE, Fukunaga Y, Bading H (2002) Extrasynaptic NMDARs oppose synaptic NMDARs by triggering CREB shut-off and cell death pathways. *Nat Neurosci* 5: 405–414
- Helmstaedt M, Sakmann B, Feldmeyer D (2009) The relation between dendritic geometry, electrical excitability, and axonal projections of L2/3 interneurons in rat barrel cortex. *Cereb Cortex* 19: 938–950
- Helmuth M, Altmann W, Böckers TM, Gundelfinger ED, Kreutz MR (2001) An electrotransfection protocol for yeast two-hybrid library screening. *Anal Biochem* 293: 149–152.
- Iland HJ, Seymour JF (2013) Role of arsenic trioxide in acute promyelocytic leukemia. *Curr Treat Options Oncol* 14: 170–184
- Jarosz-Griffiths HH, Noble E, Rushworth JV, Hooper NM (2016) Amyloid- β receptors: the good, the bad, and the prion protein. *J Biol Chem* 291: 3174–3183
- Jin M, Shepardson N, Yang T, Chen G, Walsh D, Selkoe DJ (2011) Soluble amyloid β -protein dimers isolated from Alzheimer cortex directly induce tau hyperphosphorylation and neuritic degeneration. *Proc Natl Acad Sci USA* 108: 5819–5824
- Johansson MU, Zoete V, Michielin O, Guex N (2012) Defining and searching for structural motifs using DeepView/Swiss-PdbViewer. *BMC Bioinformatics* 13: 173
- Joseph S, Kwan AH, Stokes PH, Mackay JP, Cubeddu L, Matthews JM (2014) The structure of an LIM-only protein 4 (LMO4) and deformed epidermal autoregulatory factor-1 (DEAF1) complex reveals a common mode of binding to LMO4. *PLoS One* 9: e109108
- Justus D, Dalügge D, Bothe S, Fuhrmann F, Hannes C, Kaneko H, Friedrichs D, Sosulina L, Schwarz I, Elliott DA et al (2017) Glutamatergic synaptic integration of locomotion speed via septoentorhinal projections. *Nat Neurosci* 20: 16–19
- Källberg M, Wang H, Wang S, Peng J, Wang Z, Lu H, Xu J (2012) Template-based protein structure modeling using the RaptorX web server. *Nat Protoc* 7: 1511–1522
- Karpova A, Mikhaylova M, Bera S, Bär J, Reddy PP, Behnisch T, Rankovic V, Spilker C, Bethge P, Sahin J et al (2013) Encoding and transducing the synaptic or extrasynaptic origin of NMDA receptor signals to the nucleus. *Cell* 152: 1119–1133
- Kashani AH, Qiu Z, Jurata L, Lee SK, Pfaff S, Goebbels S, Nave KA, Ghosh A (2006) Calcium activation of the LMO4 transcription complex and its role in the patterning of thalamocortical connections. *J Neurosci* 26: 8398–8408
- Kerchner GA, Deutsch GK, Zeineh M, Dougherty RF, Saranathan M, Rutt BK (2012) Hippocampal CA1 apical neuropil atrophy and memory performance in Alzheimer's disease. *Neuroimage* 63: 194–202
- Kim JH, Anwyl R, Suh YH, Djamgoz MB, Rowan MJ (2001) Use-dependent effects of amyloidogenic fragments of (beta)-amyloid precursor protein on synaptic plasticity in rat hippocampus *in vivo*. *J Neurosci* 21: 1327–1333
- Koes DR, Camacho CJ (2012) ZINCPharmer: pharmacophore search of the ZINC database. *Nucleic Acids Res* 40: W409–W414
- Kolodziej A, Lippert M, Angenstein F, Neubert J, Pethe A, Gresser OS, Amthauer H, Schroeder UH, Reymann KG, Scheich H et al (2014) SPECT-imaging of activity-dependent changes in regional cerebral blood flow induced by electrical and optogenetic self-stimulation in mice. *Neuroimage* 103: 171–180
- Kummer MP, Heneka MT (2014) Truncated and modified amyloid-beta species. *Alzheimers Res Ther* 6: 28
- Lam AD, Deck G, Goldman A, Eskandar EN, Noebels J, Cole AJ (2017) Silent hippocampal seizures and spikes identified by foramen ovale electrodes in Alzheimer's disease. *Nat Med* 23: 678–680
- Lee J-H, Yang D-S, Goulbourne CN, Im E, Stavrides P, Pensalfini A, Chan H, Bouchet-Marquis C, Bleiwas C, Berg MJ et al (2022) Faulty autolysosome acidification in Alzheimer's disease mouse models induces autophagic build-up of A β in neurons, yielding senile plaques. *Nat Neurosci* 25: 688–701
- Lenth R, Buerkner P, Herve M, Love J, Riebl H, Singmann H (2020) Emmeans: estimated marginal means, aka least-squares means, version 1.8.0
- Emmeans
- Li S, Selkoe DJ (2020) A mechanistic hypothesis for the impairment of synaptic plasticity by soluble A β oligomers from Alzheimer's brain. *J Neurochem* 154: 583–597
- Liu D, Vleugel M, Backer CB, Hori T, Fukagawa T, Cheeseman IM, Lampson MA (2010) Regulated targeting of protein phosphatase 1 to the outer kinetochore by KNL1 opposes Aurora B kinase. *J Cell Biol* 188: 809–820
- Lo-Coco F, Avvisati G, Vignetti M, Thiede C, Orlando SM, Iacobelli S, Ferrara F, Fazi P, Cicconi L, Di Bona E et al (2013) Retinoic acid and arsenic trioxide for acute promyelocytic leukemia. *N Engl J Med* 369: 111–121
- Lopez de Armentia M, Jancic D, Olivares R, Alarcon JM, Kandel ER, Barco A (2007) cAMP response element-binding protein-mediated gene expression increases the intrinsic excitability of CA1 pyramidal neurons. *J Neurosci* 27: 13909–13918
- Maimaitiyiming Y, Zhu HH, Yang C, Naranmandura H (2020) Biotransformation of arsenic trioxide by AS3MT favors eradication of acute promyelocytic leukemia: revealing the hidden facts. *Drug Metab Rev* 52: 425–437
- Malinow R (2012) New developments on the role of NMDA receptors in Alzheimer's disease. *Curr Opin Neurobiol* 22: 559–563
- Marcello E, Di Luca M, Gardoni F (2018) Synapse-to-nucleus communication: from developmental disorders to Alzheimer's disease. *Curr Opin Neurobiol* 48: 160–166
- McGuffin LJ, Bryson K, Jones DT (2000) The PSIPRED protein structure prediction server. *Bioinformatics* 16: 404–405

- Mikhaylova M, Karpova A, Bär J, Bethge P, YuanXiang P, Chen Y, Zuschratter W, Behnisch T, Kreutz MR (2014) Cellular distribution of the NMDA-receptor activated synapto-nuclear messenger Jacob in the rat brain. *Brain Struct Funct* 219: 843–860
- Mirra SS, Heyman A, McKeel D, Sumi SM, Crain BJ, Brownlee LM, Vogel FS, Hughes JP, van Belle G, Berg L (1991) The consortium to establish a registry for Alzheimer's disease (CERAD). Part II. Standardization of the neuropathologic assessment of Alzheimer's disease. *Neurology* 41: 479–486
- Nachman KE, Love DC, Baron PA, Nigra AE, Murko M, Raber G, Francesconi KA, Navas-Acien A (2017) Nitarosone, inorganic arsenic, and other arsenic species in Turkey meat: exposure and risk assessment based on a 2014 U.S. market basket sample. *Environ Health Perspect* 125: 363–369
- Oakley H, Cole SL, Logan S, Maus E, Shao P, Craft J, Guillozet-Bongaarts A, Ohno M, Disterhoft J, Van Eldik L et al (2006) Intraneuronal beta-amyloid aggregates, neurodegeneration, and neuron loss in transgenic mice with five familial Alzheimer's disease mutations: potential factors in amyloid plaque formation. *J Neurosci* 26: 10129–10140
- Oelschlegel AM, Goldschmidt J (2020) Functional neuroimaging in rodents using cerebral blood flow SPECT. *Front Phys* 8: 152
- Padurariu M, Ciobica A, Mavroudis I, Fotiou D, Baloyannis S (2012) Hippocampal neuronal loss in the CA1 and CA3 areas of Alzheimer's disease patients. *Psychiatr Danub* 24: 152–158
- Panayotis N, Karpova A, Kreutz MR, Fainzilber M (2015) Macromolecular transport in synapse to nucleus communication. *Trends Neurosci* 38: 108–116
- Parsons MP, Raymond LA (2014) Extrasynaptic NMDA receptor involvement in central nervous system disorders. *Neuron* 82: 279–293
- Peng L, Bestard-Lorigados I, Song W (2022) The synapse as a treatment avenue for Alzheimer's disease. *Mol Psychiatry* 27: 2940–2949
- Price JL, Ko AI, Wade MJ, Tsou SK, McKeel DW, Morris JC (2001) Neuron number in the entorhinal cortex and CA1 in preclinical Alzheimer disease. *Arch Neurol* 58: 1395–1402
- Rönicke R, Mikhaylova M, Rönicke S, Meinhardt J, Schroder UH, Fandrich M, Reiser G, Kreutz MR, Reymann KG (2011) Early neuronal dysfunction by amyloid beta oligomers depends on activation of NR2B-containing NMDA receptors. *Neurobiol Aging* 32: 2219–2228
- Rosset A, Spadola L, Ratib O (2004) OsiriX: an open-source software for navigating in multidimensional DICOM images. *J Digit Imaging* 17: 205–216
- Saura CA, Cardinaux JR (2017) Emerging roles of CREB-regulated transcription coactivators in brain physiology and pathology. *Trends Neurosci* 40: 720–733
- Saura CA, Valero J (2011) The role of CREB signaling in Alzheimer's disease and other cognitive disorders. *Rev Neurosci* 22: 153–169
- Schindelin J, Arganda-Carreras I, Frise E, Kaynig V, Longair M, Pietzsch T, Preibisch S, Rueden C, Saalfeld S, Schmid B et al (2012) Fiji: an open-source platform for biological-image analysis. *Nat Methods* 9: 676–682
- Schymkowitz J, Borg J, Stricher F, Nys R, Rousseau F, Serrano L (2005) The FoldX web server: an online force field. *Nucleic Acids Res* 33: W382–W388
- Selkoe DJ (2002) Alzheimer's disease is a synaptic failure. *Science* 298: 789–791
- Selkoe DJ, Hardy J (2016) The amyloid hypothesis of Alzheimer's disease at 25 years. *EMBO Mol Med* 8: 595–608
- Spilker C, Nullmeier S, Grochowska KM, Schumacher A, Butnaru I, Macharadze T, Gomes GM, Yuanxiang P, Bayraktar G, Rodenstein C et al (2016) A Jacob/Nsmf gene knockout results in hippocampal dysplasia and impaired BDNF signaling in dendritogenesis. *PLoS Genet* 12: e1005907
- Stokes PH, Liew CW, Kwan AH, Foo P, Barker HE, Djamirze A, O'Reilly V, Visvader JE, Mackay JP, Matthews JM (2013) Structural basis of the interaction of the breast cancer oncogene LMO4 with the tumour suppressor CtIP/RBBP8. *J Mol Biol* 425: 1101–1110
- Su L, Hayes L, Soteriades S, Williams G, Brain SAE, Firbank MJ, Longoni G, Arnold RJ, Rowe JB, O'Brien JT (2018) Hippocampal stratum radiatum, lacunosum, and molecular sparing in mild cognitive impairment. *J Alzheimers Dis* 61: 415–424
- Teich AF, Nicholls RE, Puzzo D, Fiorito J, Purgatorio R, Fa M, Arancio O (2015) Synaptic therapy in Alzheimer's disease: a CREB-centric approach. *Neurotherapeutics* 12: 29–41
- The National Institute on Aging (1997) The national Institute on aging, and reagan institute working group on diagnostic criteria for the neuropathological assessment of Alzheimer's disease. *Neurobiol Aging* 18 (Suppl 4): S1–S2
- Trinkle-Mulcahy L, Sleeman JE, Lamond AI (2001) Dynamic targeting of protein phosphatase 1 within the nuclei of living mammalian cells. *J Cell Sci* 114: 4219–4228
- Tsuriei S, Geva R, Zamorano P, Dresbach T, Boeckers T, Gundelfinger ED, Garner CC, Ziv NE (2006) Local sharing as a predominant determinant of synaptic matrix molecular dynamics. *PLoS Biol* 4: e271
- Wang A, Bibb JA (2011) Is CREB the angry bird that releases memory in Alzheimer's? *Neuropsychopharmacology* 36: 2153–2154
- Wirh's O, Zampar S (2020) Neuron loss in Alzheimer's disease: translation in transgenic mouse models. *Int J Mol Sci* 21: 8144
- Wishart DS, Knox C, Guo AC, Shrivastava S, Hassanali M, Stothard P, Chang Z, Woolsey J (2006) DrugBank: a comprehensive resource for *in silico* drug discovery and exploration. *Nucleic Acids Res* 34: D668–D672
- Yiu AP, Rashid AJ, Josselyn SA (2011) Increasing CREB function in the CA1 region of dorsal hippocampus rescues the spatial memory deficits in a mouse model of Alzheimer's disease. *Neuropsychopharmacology* 36: 2169–2186
- Yu XW, Curlik DM, Oh MM, Yin JC, Disterhoft JF (2017) CREB overexpression in dorsal CA1 ameliorates long-term memory deficits in aged rats. *Elife* 6: e19358
- Zhou Y, Won J, Karlsson MG, Zhou M, Rogerson T, Balaji J, Neve R, Poirazi P, Silva AJ (2009) CREB regulates excitability and the allocation of memory to subsets of neurons in the amygdala. *Nat Neurosci* 12: 1438–1443
- Zott B, Simon MM, Hong W, Unger F, Chen-Engerer HJ, Froesch MP, Sakmann B, Walsh DM, Konnerth A (2019) A vicious cycle of β amyloid-dependent neuronal hyperactivation. *Science* 365: 559–565



License: This is an open access article under the terms of the [Creative Commons Attribution-NonCommercial-NoDerivs](https://creativecommons.org/licenses/by-nc-nd/4.0/) License, which permits use and distribution in any medium, provided the original work is properly cited, the use is non-commercial and no modifications or adaptations are made.

Expanded View Figures

Figure EV1. The role of Jacob in cAMP-responsive element-binding protein (CREB) shutoff.

- A Validation of Jacob and pJacob antibodies for detection of the human protein. Human Jacob fused to a Spot tag was expressed in HEK293T cells for antibody detection. The rat amino acid sequence of Jacob used for generation of pan-Jacob antibodies is highly conserved in human and mouse and the antibody effectively detects human Jacob.
- B, C Total Jacob protein levels are not significantly reduced in brain samples from Alzheimer's disease (AD) patients as compared to the control group. (C) Bar plots representing the quantification of Jacob immunoreactivity normalized to H3. $N = 11-12$ protein extracts from different subjects in each group.
- D, E Total NeuN protein levels are significantly reduced in brain samples from AD patients as compared to the control group. (C) Bar plots representing the quantification of NeuN immunoreactivity normalized to H3. $N = 11-12$ protein extracts from different subjects in each group.
- F Scatter plots representing gating strategy used in FACS experiments for neuronal pCREB and CREB immunoreactivity quantification.
- G, H Acute (1 h) $A\beta_{1-42}$ treatment does not induce changes in pan CREB levels in organotypic hippocampal slices from Jacob ($-/-$) mice. (G) Representative confocal images of slices immunolabeled against pCREB, co-labeled with NeuN and DAPI. Scale bar: 100 μm . (H) Bar plot of CREB immunoreactivity averaged per slice, $N = 14-16$ slices.
- I pJacob level and pJacob/panJacob ratio are decreased in TBA2.1 mouse line compared to WT animals. Representative images of the immunoblot probed with antibodies against pJacob, pan-Jacob, and re-probed with Histone3 (H3).
- J-L Bar plots representing the quantification of (J) Jacob, (K) pJacob levels and the (L) pJacob/Jacob ratio normalized to H3. $N = 5-7$ hippocampal protein extracts.
- M Significant changes in cerebral blood flow between TBA2.1 and WT, TBA2.1, $-/-$ and WT, and TBA2.1 and TBA2.1, $-/-$ as determined by $^{99\text{mTc}}$ -HMPAO SPECT measurements. Difference images overlay over a reference MR for comparison with TBA2.1 mice as described on panel labeling. Bregma -2.5 . Statistically significant differences between TBA2.1 and double transgenic animals were detected in dorsal CA1 (regions indicated by arrowheads). $N = 10$ animals ($P < 0.05$) by two-tailed Student's t -test.
- N Significant changes in cerebral blood flow between TBA2.1 and WT, TBA2.1, $-/-$ and WT as determined by SPECT measurements. Statistically significant differences between TBA2.1 or double transgenic animal and WT were detected in lateral septal nucleus and the diagonal band nucleus (regions indicated by arrowheads) ($P < 0.01$) by two-tailed Student's t -test.
- O-Q The quantification of glial cells revealed no major differences between TBA2.1 and double transgenic animals (TBA2.1, $-/-$). (O) Representative confocal images of distal CA1 sections from 13 weeks old mice stained for GFAP, DAPI and Iba-1. Scale bar: 100 μm . (P) Bar plot representing the number of GFAP-positive cells per rectangular region of interest. $N = 17-24$ cryosections from 5 to 7 animals per genotype. (Q) Bar plot representing the number of Iba-1-positive cells per rectangular region of interest. $N = 17-26$ cryosections from 5 to 7 animals per genotype.
- R, S The quantification of $A\beta$ plaques revealed no major differences between TBA2.1 and double transgenic animals (TBA2.1, $-/-$). (R) Confocal images averaged from two sections of the molecular layer of 13-week-old mice distal CA1 labeled for amyloid- β (4G8 antibody) and co-stained with DAPI. Scale bar: 100 μm . (S) Bar plot representing the number of amyloid- β -positive puncta per 100 μm . $N = 8$, number of cryosections from two animals per genotype.

Data information: ns, non-significant difference, $*P < 0.05$, $**P < 0.01$, $***P < 0.001$ by (C, J-L) two-tailed Student's t -test or (H) two-way ANOVA followed by Bonferroni's multiple comparisons test or (P, Q, S) linear mixed-effects model followed by Tukey's multiple comparisons test. All data are represented as mean \pm SEM. Source data are available online for this figure.

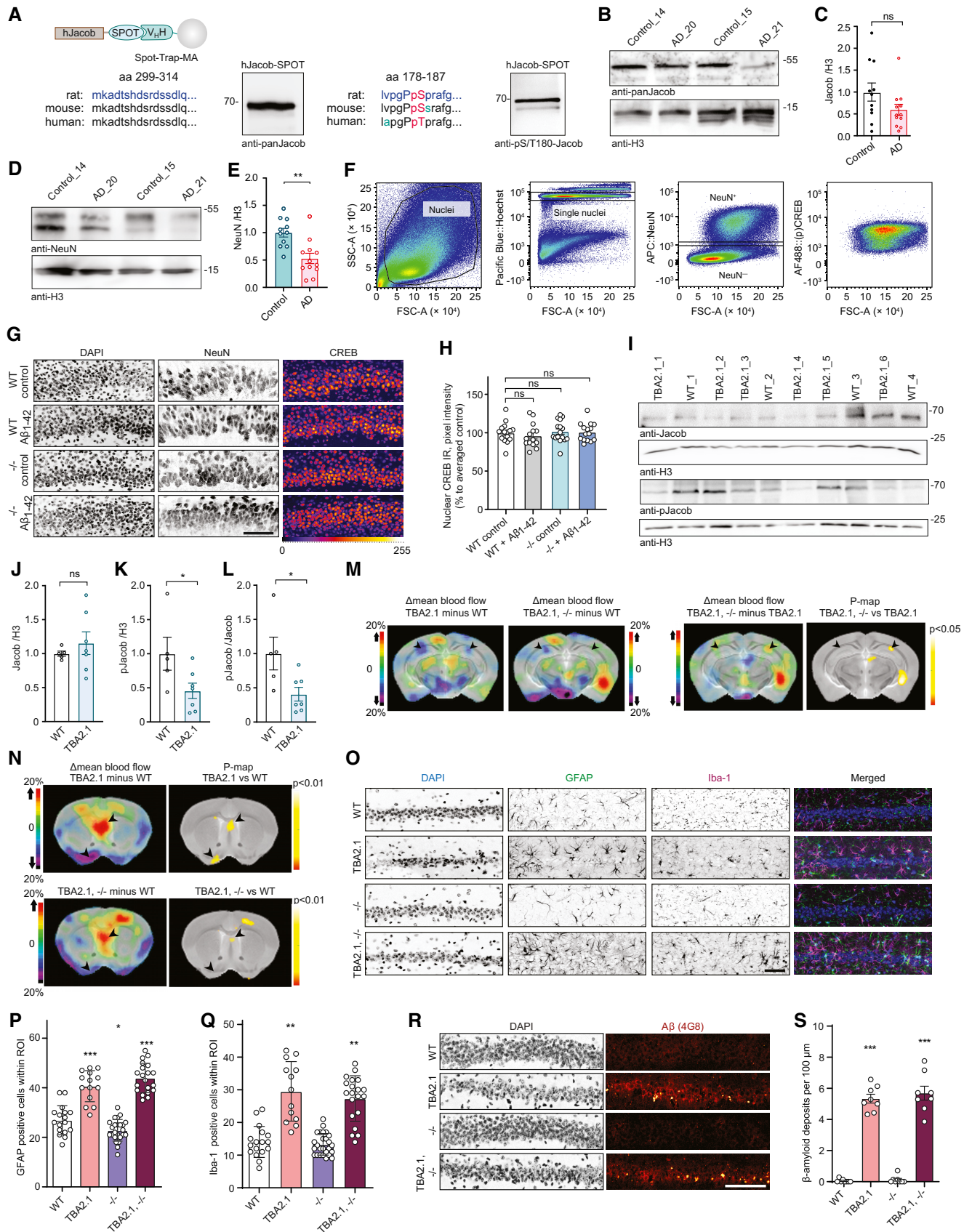


Figure EV1.

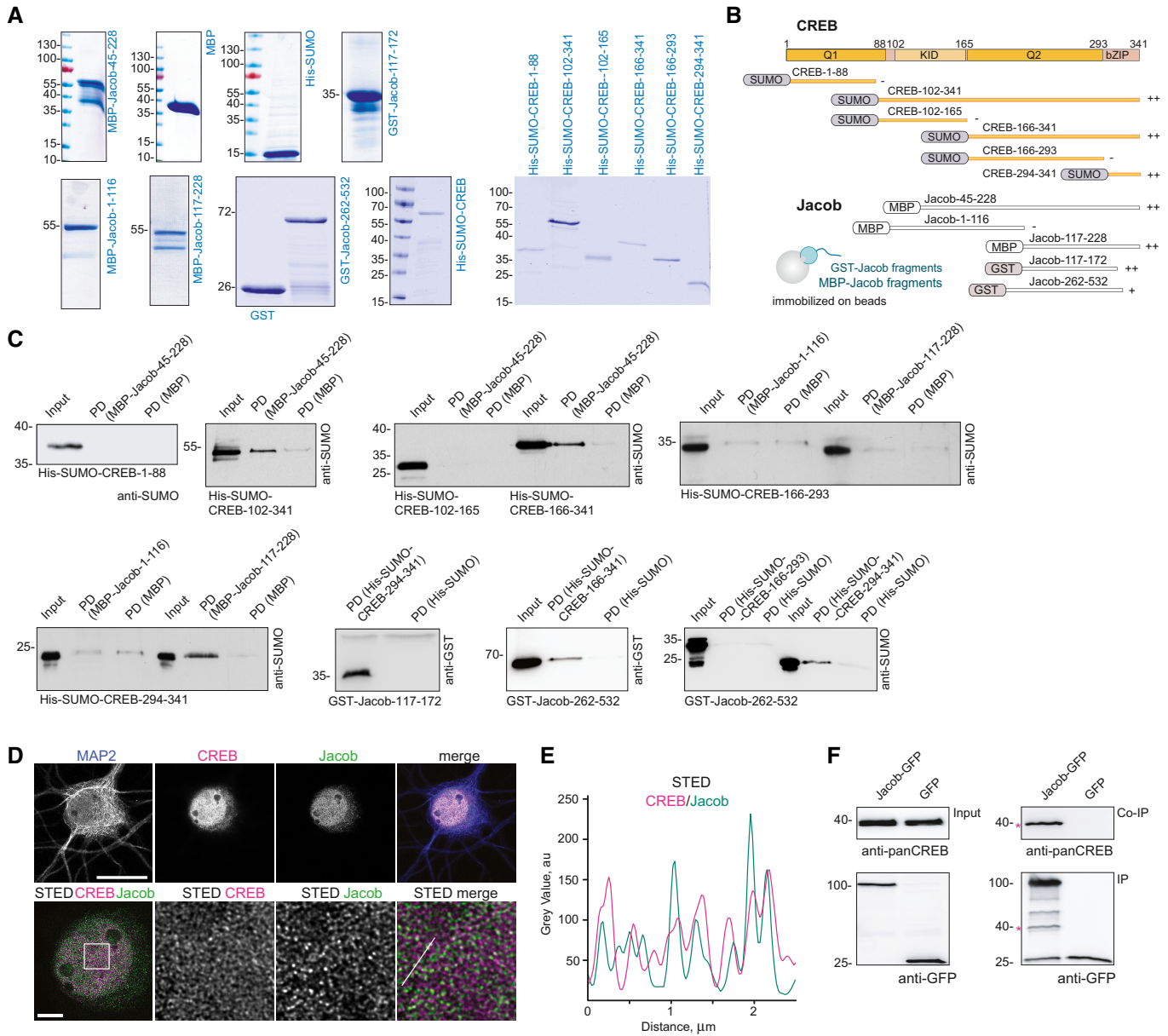


Figure EV2. Mapping of the binding interfaces between Jacob and cAMP-responsive element-binding protein (CREB).

- A** Coomassie blue staining depicting the purity of bacterially produced proteins used for pull-down assays between CREB and Jacob.
- B** Scheme representing the constructs used for mapping of the interaction sites in Fig 1D and Appendix Fig S1B.
- C** The N-terminus of Jacob (117–172 aa in red) interacts with the bZIP domain of CREB, but not with the Q1 (1–88 aa), KID (102–165 aa), or Q2 (166–293 aa) domain. The C-terminus of Jacob (262–532 aa) shows weaker binding to the bZIP domain of CREB. Images of immunoblots representing pull-down assays performed with Jacob and CREB protein fragments depicted in the panel (B).
- D, E** Confocal and STED images show an association of CREB with Jacob in the nucleus of DIV16 hippocampal primary neurons. (D) The upper panel represents deconvolved confocal images. Lower panels depict deconvolved STED images. Scale bars: 20 and 5 μm , respectively. Inserts are denoted by a white square. (E) Line profiles indicate the overlap of relative intensities for CREB and Jacob along a 2.5 μm line.
- F** Endogenous CREB co-immunoprecipitate with overexpressed Jacob-GFP, but not GFP from HEK293T cell extracts. The asterisk denotes the CREB band from a membrane subsequently re-probed with an anti-GFP antibody.

Source data are available online for this figure.

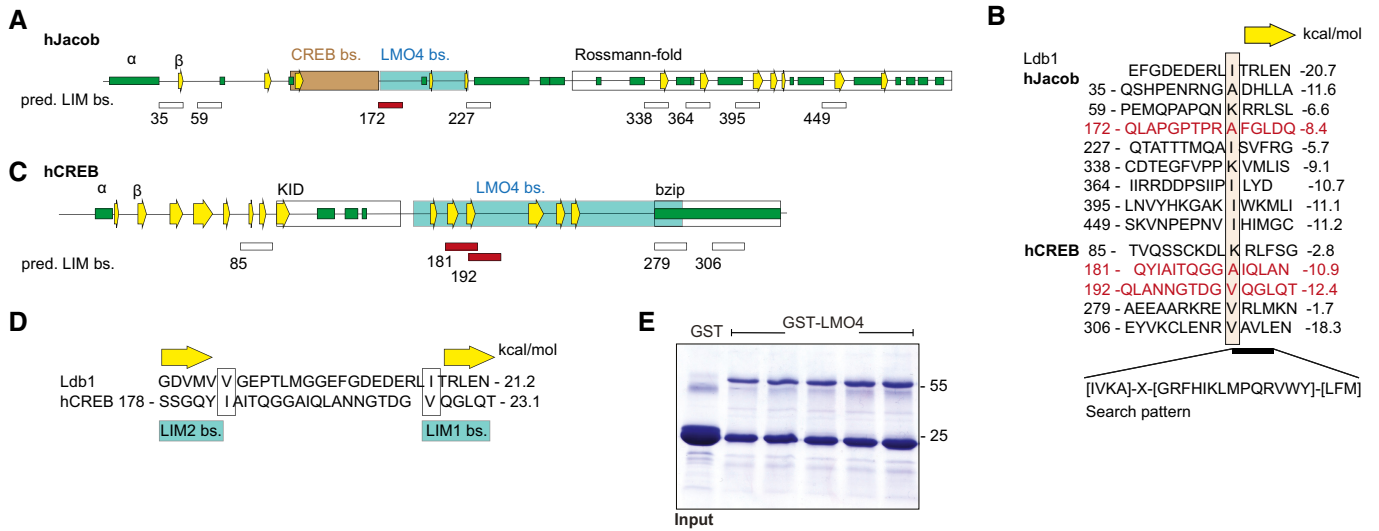


Figure EV3. Nitarsone disrupts the Jacob-LMO4 interaction.

A–D Predicted binding sites for LMO4 LIM domains in Jacob and cAMP-responsive element-binding protein (CREB). (A) Schematic structure of human Jacob showing predicted secondary structures (helices, green; β -strands, yellow arrows) and experimentally determined binding regions for CREB (orange) and LMO4 (gray). The C-terminus of Jacob is predicted to have a Rossmann-fold similar to caspases. (B) The LIM1 binding peptide of Ldb1 is aligned to 8 sequences of Jacob that match the search pattern for the conserved hydrophobic residues and the adjacent β -strand. Structures of LIM1:peptides were modeled and free energy $\Delta\Delta G$ were calculated. Only the peptide starting at 172 (red) lies within the LMO4 binding region. In human, CREB 5 matching peptides were identified. (C) Schematic structure of human CREB with labeled LMO4-binding region and known KID and bZIP domains. (D) The two peptides starting at 181 and 192 are within the LMO4-binding region and align to Ldb1 peptide where 181 binds to LIM2 and 192 to LIM1. **E** Image of gels stained with coomassie blue showing the purity of bacterially produced GST-LMO4 used for pull-down assay.

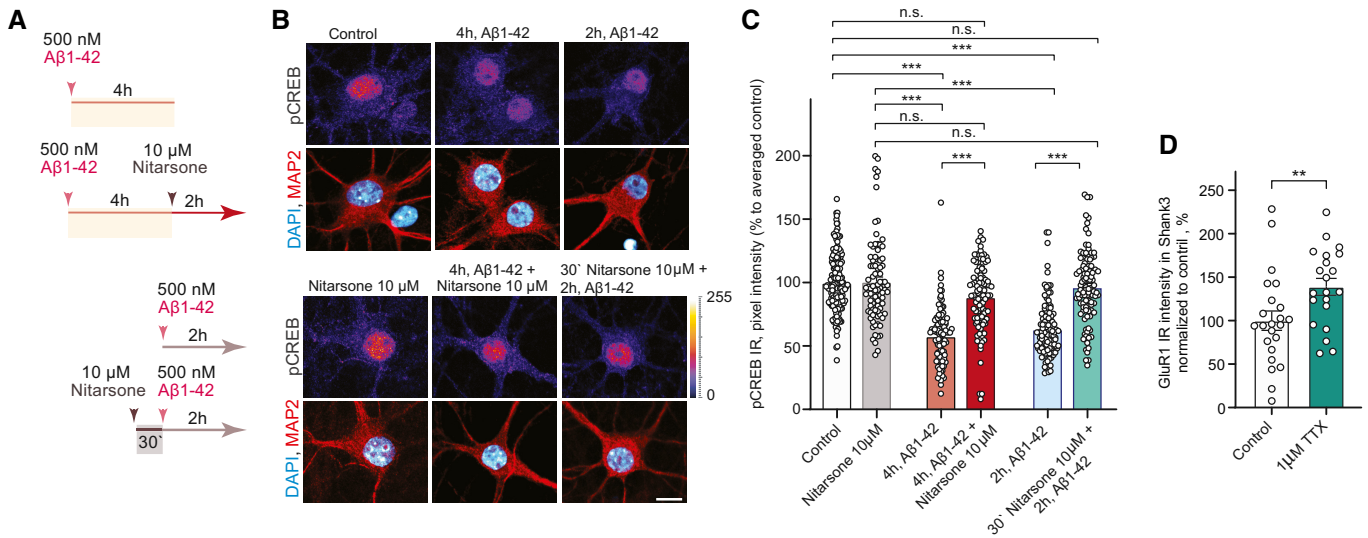


Figure EV4.

Figure EV4. Nitarsonone prevents Aβ-induced cAMP-responsive element-binding protein (CREB) shutoff *in vitro*.

A–C Acute treatment with 10 μM Nitarsonone rescues Aβ_{1–42}-induced CREB shutoff. (A) Scheme of the experimental design. The dissociated, hippocampal cell cultures at DIV16 were either pre-treated for 30 min with 10 μM Nitarsonone and subsequently 2 h with 500 nM Aβ_{1–42} or the drug was added 2 h after the 500 nM Aβ_{1–42} treatment. The pCREB immunoreactivity was measured in comparison to vehicle control. (B) Representative confocal images of hippocampal neurons. Lookup table indicates the pixel intensities from 0 to 255. Scale bar: 10 μm. (C) Bar plot representing nuclear pCREB immunostaining intensity normalized to vehicle control. *N* = 88–101 from 5 to 7 independent cell cultures. ****P* < 0.001 by two-way ANOVA with Sidak's *post hoc* test.

D Treatment with 1 μM TTX induced upregulation of GluR1 surface expression. *N* = 21–23 dendritic segments from three independent cell cultures. ***P* < 0.01 by two-tailed Student's *t*-test.

Data information: All data are represented as mean ± SEM.
Source data are available online for this figure.

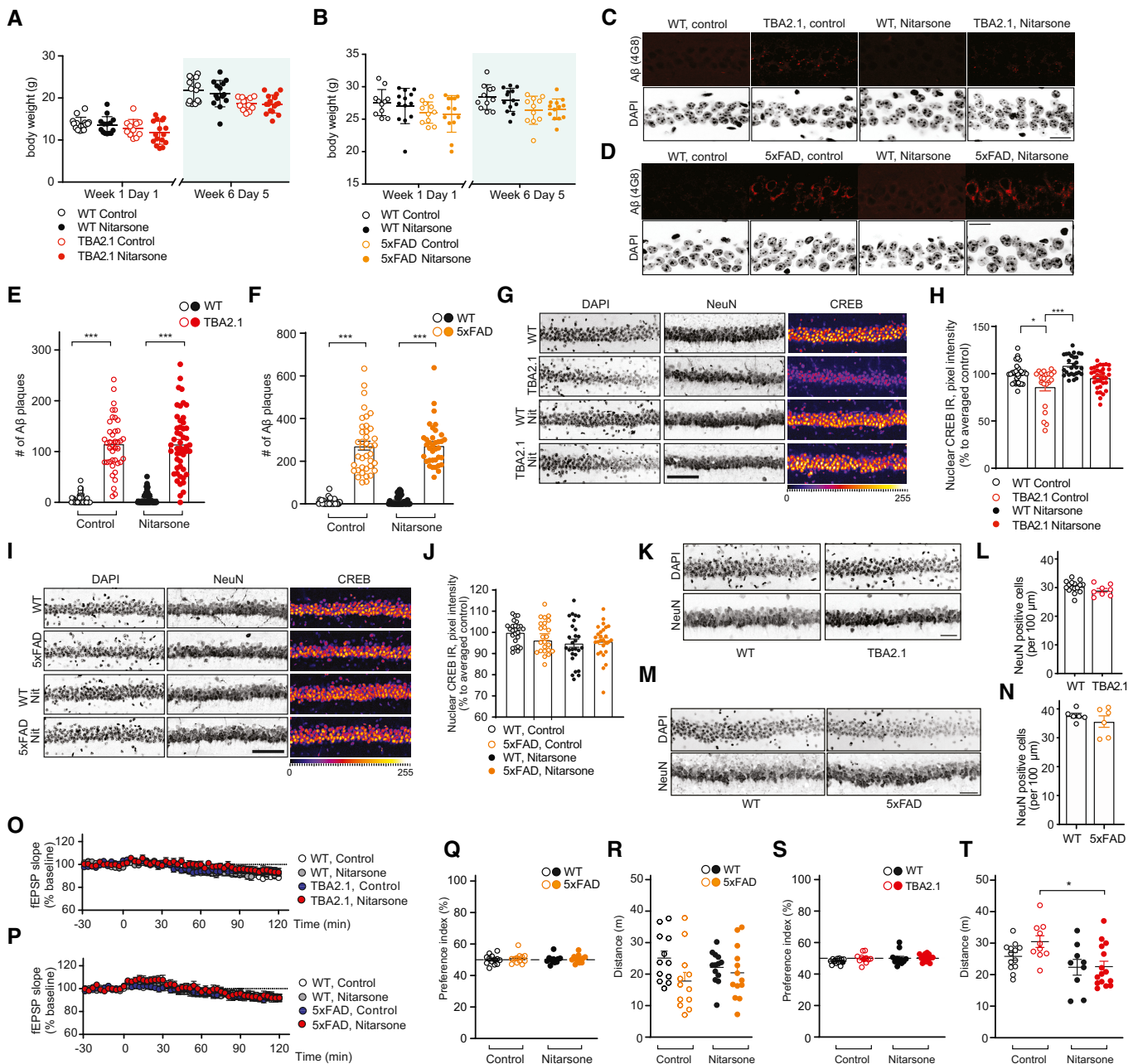
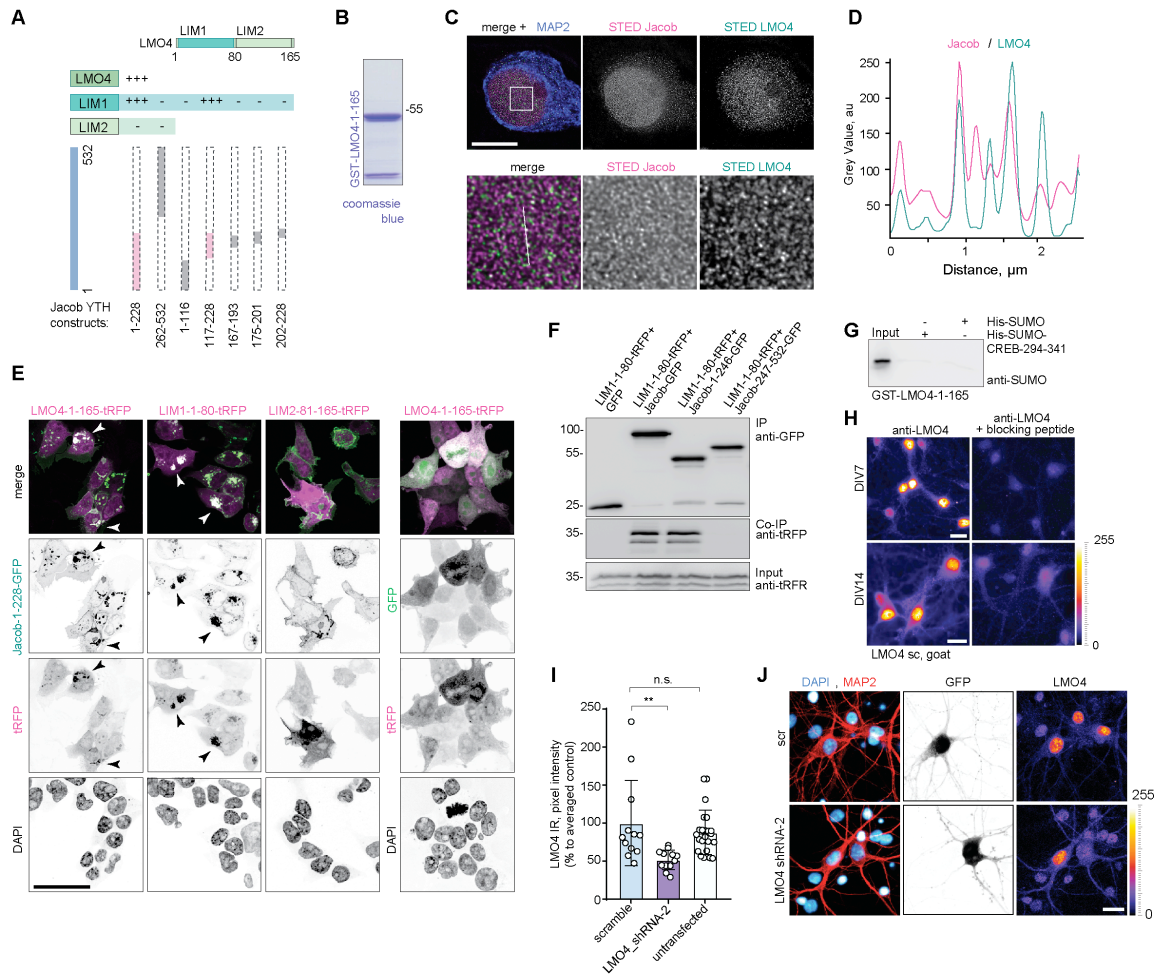


Figure EV5.

Table of Contents

Appendix Figure S1.....	2
Appendix Figure S2.....	4



Appendix Figure S1. Confirmation of the LMO4-Jacob interaction, LMO4 antibody specificity and quantification of LMO4 knockdown efficiency, confirmation of Jacob-PP1 interaction, protein purity and loading controls for pull down experiments and studies on the interaction and network activity depending upon Jacob S180 phosphorylation.

(A) Jacob-117-228 interacts with the LIM1 domain of LMO4 in Y2H. (+++) indicates a strong interaction while (-) indicates no interaction. Evaluation was based on the number of colonies growing in triple drop-out media.

(B) Coomassie blue stained gel showing purity of GST-LMO4 used in the pull-down experiments.

(C, D) Super-resolution STED imaging revealed association of Jacob with LMO4 in the nucleus **(C)**. DIV16 primary hippocampal neurons stained with antibodies against MAP2, LMO4, pan-Jacob. Upper panel - scale bar:10 μm , lower panel (inserts 5 μm x5 μm – denoted by the white square). **(D)** Line profiles indicate relative intensities for deconvolved STED channels along a 2.5 μm line.

(E) Jacob-1-228-GFP co-recruits the LIM1 (1-80), but not LIM2 (81-165) domain of LMO4. Confocal images of HEK293T cells co-transfected either with Jacob-1-228-GFP or GFP together with LMO4 constructs. Arrows indicate co-recruitment. Scale bar: 40 μm .

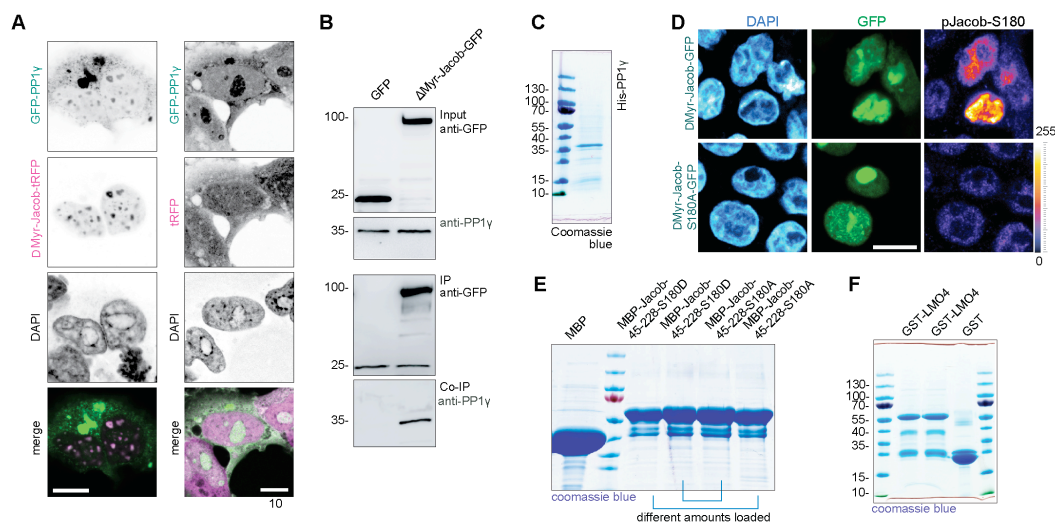
(F) LIM1-1-80-tRFP co-immunoprecipitate with Jacob-1-246-GFP, but not Jacob-247-532-GFP from HEK293T cell extracts.

(G) Pull-down experiments revealed no interaction between His-SUMO-CREB-294-341 with GST-LMO4.

(H) A goat LMO4 antibody was used to stain LMO4 in hippocampal neurons (DIV 7 and DIV 14) in the presence or absence of the blocking peptide. Scale bar: 15 μm .

(I) Nuclear LMO4 staining intensity was downregulated in neurons expressing shRNA targeting LMO4 mRNA compared to scrambled-transfected (scr shRNA) or non-transfected cells. Data represented as mean \pm SEM. n=12-23 nuclei. ** $p < 0,021$ by Kruskal-Wallis test followed by Dunn's multiple comparison test.

(J) Representative, confocal images of hippocampal neurons transfected with shRNA targeting LMO4 or scrambled control. Reduction of nuclear LMO4 level was confirmed in immunocytochemistry with the goat anti-LMO4 antibody. Scale bar:10 μm .



Appendix Figure S2. Jacob interacts with PP1γ.

(A) Confocal images of HEK293T cells overexpressing GFP-PP1γ together with either ΔMyr-Jacob-tagRFP or tRFP control revealed nuclear co-clustering of both proteins. Scale bar: 20 μm.

(B) ΔMyr-Jacob-GFP but not GFP co-immunoprecipitate with endogenous PP1γ from HEK293T cells extracts.

(C) Coomassie blue stained gel showing purity of commercially available His-PP1γ.

(D) Nuclear Jacob (ΔMyr-Jacob-GFP), but not nuclear phosphodeficient mutant (ΔMyr-Jacob-S180A-GFP) expressed in HEK293T cells is phosphorylated. Confocal images of HEK293T cells overexpressing Jacob and immunostained with anti-pS180Jacob antibodies. Scale bar: 10 μm.

(E) Image of gels stained with coomassie blue showing the purity of bacterially produced Jacob mutants used for pull-down assays.

(F) Images of gels stained with coomassie blue showing inputs for bacterially produced GST-LMO4 coupled to beads used for pull-down assay with Jacob and PP1γ.

Figure EV5. Treatment with Nitarsons rescues Alzheimer's disease (AD)-related phenotypes *in vivo*.

- A, B Nitarsons treatment did not affect body weight of (A) TBA2.1 ($N = 22\text{--}24$ animals per group) or (B) 5xFAD mice ($N = 11\text{--}13$ animals per group).
- C–F Nitarsons treatment does not change amyloid load in (C, E) TBA2.1 and (D, F) 5xFAD mice. (C, D) Confocal images averaged from two sections of the molecular layer of CA1 labeled for amyloid- β (4G8 antibody) and co-stained with DAPI. Scale bar: 100 μm . (E, F) Bar plots representing the number of amyloid- β -positive puncta. (E) TBA2.1 $N = 40\text{--}50$ CA1 regions 6–9 animals per genotype and (F) 5xFAD $N = 33\text{--}40$ CA1 regions 6–7 animals per genotype.
- G, H Nitarsons rescues the reduction of CREB immunoreactivity in NeuN positive cells in CA1 of TBA2.1 mice. (G) Representative confocal images of CA1 cryosections from 11-week-old mice stained for NeuN, DAPI, and CREB. Scale bar: 10 μm . (H) Bar plot of CREB nuclear staining intensity. $N = 21\text{--}34$ hippocampal sections from 6 to 9 animals.
- I, J Nitarsons does not affect CREB immunoreactivity in NeuN-positive cells in CA1 of TBA2.1 mice. (I) Representative confocal images of CA1 cryosections from 18-week-old mice stained for NeuN, DAPI, and CREB. Scale bar: 10 μm . (J) Bar plot of CREB nuclear staining intensity. $N = 28\text{--}34$ hippocampal sections from 6 to 7 animals.
- K, L TBA2.1 mice do not display neuronal loss at the beginning of the Nitarsons treatment. (K) Representative confocal images of distal CA1 cryosections from 4 weeks old mice stained for NeuN, DAPI, and CREB. Scale bar: 10 μm . (L) Bar graph representing the average number of NeuN-positive cells normalized to WT treated with vehicle. $N = 8\text{--}16$ hippocampal sections from 2 to 3 animals.
- M, N 5xFAD mice do not display neuronal loss at the end of the Nitarsons treatment. (M) Representative confocal images of distal CA1 cryosections from 19-week-old mice stained for NeuN, DAPI, and CREB. Scale bar: 10 μm . (N) Bar graph representing the average number of NeuN-positive cells normalized to WT treated with vehicle. $N = 6$ hippocampal sections from two animals.
- O, P Basal synaptic transmission is not affected by bath application of Nitarsons in (O) TBA2.1 and (P) 5xFAD mice. TBA2.1: $N = 14\text{--}18$ slices from 5 to 6 mice and 5xFAD: $N = 17\text{--}18$ slices from six mice.
- Q, R (Q) Nitarsons treatment does not influence preference index and (R) distance traveled during open-field arena exploration of TBA2.1 mice. $N = 12\text{--}13$ mice per group.
- S, T (S) Nitarsons treatment does not influence preference index and (T) slightly normalizes increased distance traveled during open-field arena exploration of 5xFAD mice. $N = 12$ mice per group.

Data information: * $P < 0.05$, *** $P < 0.001$ by linear mixed-effects model followed by Tukey's multiple comparisons test. All data are represented as mean \pm SEM. Source data are available online for this figure.